Aalborg University

Design of Mechanical Systems - Master's thesis

Alexander K. Johansen & Oliver Kragh

Simulation-driven design of loudspeaker cabinet using optimization algorithms for finite element models

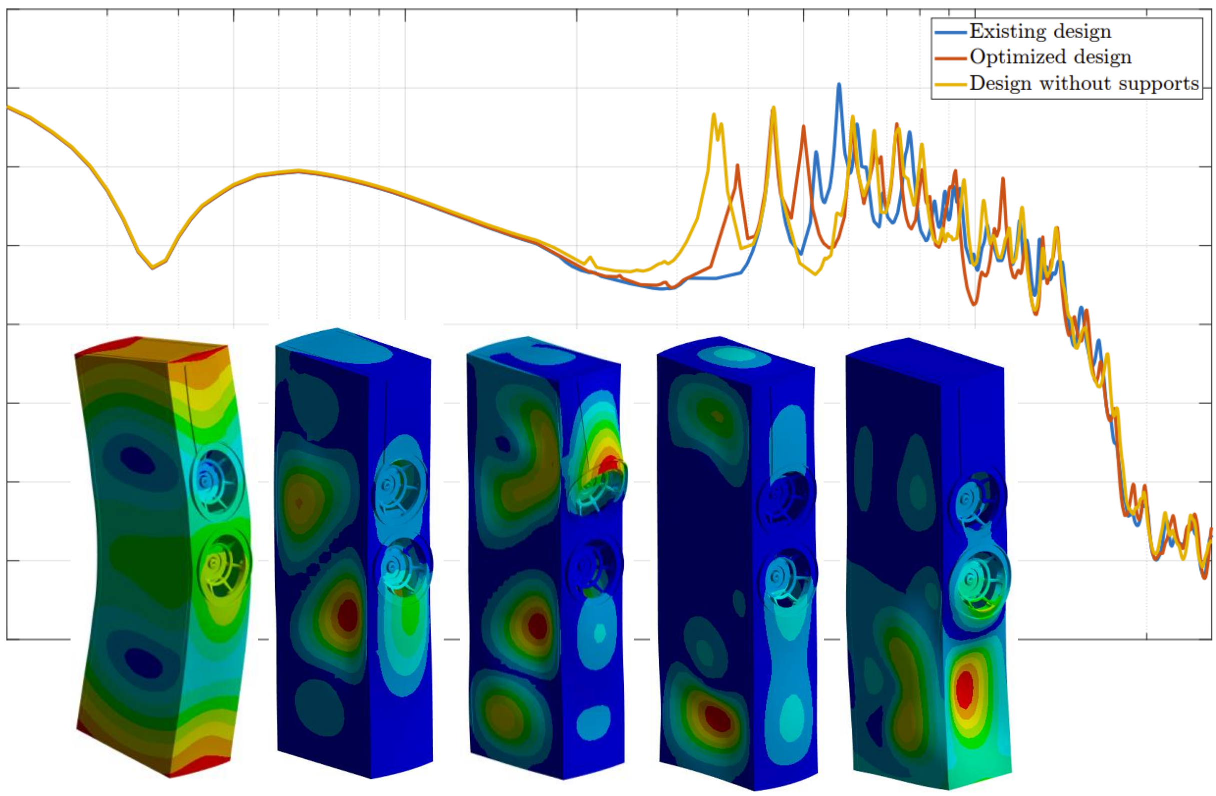

1st of June 2023

Faculty of Engineering and Science
Materials and Production
Fibigerstræde 16
9220 Aalborg Øst
Denmark

Title:

Simulation-driven design of loudspeaker cabinet using optimization algorithms for finite element models

Project:

Design of Mechanical Systems - Master's thesis
Mechanical Engineering & Manufacturing

Project period:

1st February 2023 - 1st June 2023

Project group:

Group 9

Participant(s):

Alexander Kruse Johansen
Oliver Kragh Hindborg Olsen

Supervisor(s):

Sergey V. Sorokin

Total number of pages: 69

Synopsis:

The loudspeaker manufacturer, DALI, currently uses FEA and BEM in the development of the drivers and the bass reflex ports in their loudspeakers, and has a wish of expanding their simulation-driven methodology to also include the design of the cabinets.
In this project, it is demonstrated how the simulation-driven design approach can be expanded to also include the design of the cabinet. The project takes point of departure in the Rubicon 6 loudspeaker, but the presented procedure can also be applied to other loudspeaker cabinets.
A benchmark harmonic analysis, that prioritizes accuracy over computational efficiency, is developed and validated against an experiment measuring the accelerations of the cabinet using accelerometers. The benchmark model is then simplified to a computationally faster design model, giving similar results to the benchmark model. The positions of the internal support structures are parameterized and optimized using a genetic algorithm with the objective function of minimizing the maximum equivalent radiated power level of all exterior MDF surfaces of the cabinet. The result is a cabinet that has a reduced level of equivalent radiated power compared to the existing design, by only moving the already existing supports to another position.
Additionally, a general bracing structure is proposed and optimized which demonstrates that no knowledge about the response of the cabinet is required to produce a design which is better than the existing design.

Preface

This project is written during the spring semester of 2023 and finished on June 1st 2023 at Aalborg University in collaboration with DALI A/S. Citations are indicated by a bracketed number, [#], and are sorted in order of appearance. All citations appear at the end of the report in order of first appearance. Appendix A shows the displacement at all the points measured in the experiment and Appendix B shows the calibration data of the accelerometer used in the experiment. Both appendices are located at the end of the report.

Special thanks to Claus Futtrup, Head of Acoustic Engineering at DALI A/S, for his supervision during the project.

Oliver Kragh

Oliver Kragh

Alexander Kruse Johansen

Alexander Kruse Johansen

Contents

Preface **iv**

1 Introduction **1**

2 Theory **3**
2.1 Theory of sound . . . 3
2.2 Theory of modal analysis . . . 8
2.3 Theory of harmonic analysis . . . 10
2.4 Theory of damping . . . 13
2.5 Theory of optimization . . . 17

3 Problem statement **22**
3.1 Task definition . . . 22
3.2 Delimitations . . . 23

4 Development of benchmark model **24**
4.1 Preliminary benchmark model . . . 24
4.2 Design of experiment . . . 30
4.3 Finalized benchmark model . . . 36
4.4 Conclusion of sub task 1 . . . 42

5 Development of design model **43**
5.1 Methods for reducing solution time . . . 43
5.2 Simplifications and results . . . 44
5.3 Conclusion of sub task 2 . . . 48

6 Repositioning of internal supports using optimization **49**
6.1 Parameterization . . . 49
6.2 Objective function . . . 50
6.3 Optimization and results . . . 51
6.4 Comparison of designs . . . 54
6.5 Conclusion of sub-task 3 . . . 56

7 Redesign of internal supports using optimization **57**
7.1 Initial design concept . . . 57
7.2 Sensitivity analysis . . . 58
7.3 Optimization and results . . . 59
7.4 Conclusion of sub-task 4 . . . 61

8 Discussion **62**

9 Conclusion **64**

10 Further Work **65**
10.1 Effects of manufacturing tolerances . . . 65
10.2 Changing the cavity divider . . . 65
10.3 Development of a general initial design . . . 65

Bibliography **66**

A Validation of benchmark model **68**

B Accelerometer calibration **69**

1 Introduction

Danish Audiophile Loudspeaker Industries, often abbreviated as DALI, designs, manufactures and sells loudspeakers for home audio. DALI A/S currently uses FEA and BEM in the development of the drivers and the bass reflex ports but has a wish of expanding their simulation-driven methodology to also include the design of the cabinets. A simulation-driven approach for the cabinet is quite novel in the loudspeaker industry, as this is an industry primarily populated by audio engineers that have little experience in the design of structural components such as the cabinet. This is also reflected in literature, as plenty of books and articles exist on the topic of the design of the drivers, e.g. the classic and absolutely fundamental [1], but the selection is very scarce when it comes to cabinet design. Books such as [2] seem promising at first, however, for mechanical engineers the book leaves a lot to be desired. There is a large focus on the influence of various cabinet geometries on the fluid-structure interaction between the air and cabinet but with little to no regard for the response of the actual cabinet. This trend continues in [3], which admittedly is more catered towards hobbyists rather than engineers, here it is likewise common practice to assume that all cabinet parts are infinitely rigid, thereby not considering the cabinet as a waveguide. This is of course a very naive assumption as the diaphragm of the driver and the side wall of the cabinet in principle both displace in a direction that is perpendicular to their surface, which is the only cause of sound radiation to an adjacent medium that cannot support shear stresses. [4, p. 35]

However, DALI A/S recognizes that the cabinet is in fact elastic and should be treated as a waveguide accordingly. The aim of this project is thus to develop and demonstrate how FE-simulation can be used to design a cabinet. As DALI A/S already is an established manufacturer of loudspeakers the design of the cabinet is fairly restricted, as the creative design team dictates the outer surfaces of the cabinet. Then the audio engineers choose a combination of drivers that are fitting for the price point of the speaker, which in turn also determines the internal volume each cabinet must provide for the drivers, along with the location of the bass reflex ports. This project is therefore only focused on the design of the internal support structure of the cabinet, as fairly large changes can be made with minimal consequences for the rest of the loudspeaker.

The properties that constitute a good cabinet, in addition to serving as a mounting point for the various components and providing the required internal volume, is its ability to not radiate sound. This means that a good speaker cabinet radiates as little sound as possible from its ports, the only exception being at the port frequency, and panels, as this interferes with the sound radiated by the drivers. [5] As the placement of the ports is determined by the audio engineers at DALI A/S, the main focus of the project is to reduce the latter, i.e. the sound radiated by the panels of the cabinet.

In order to develop a fairly universal procedure for cabinet design using FE-simulation the pre-existing Rubicon 6 loudspeaker made by DALI A/S is chosen. It is assumed that the procedure developed is also applicable to other loudspeakers. Figure 1.1 shows an overview of the Rubicon 6 loudspeaker and its components and serves to establish the nomenclature used throughout the project.

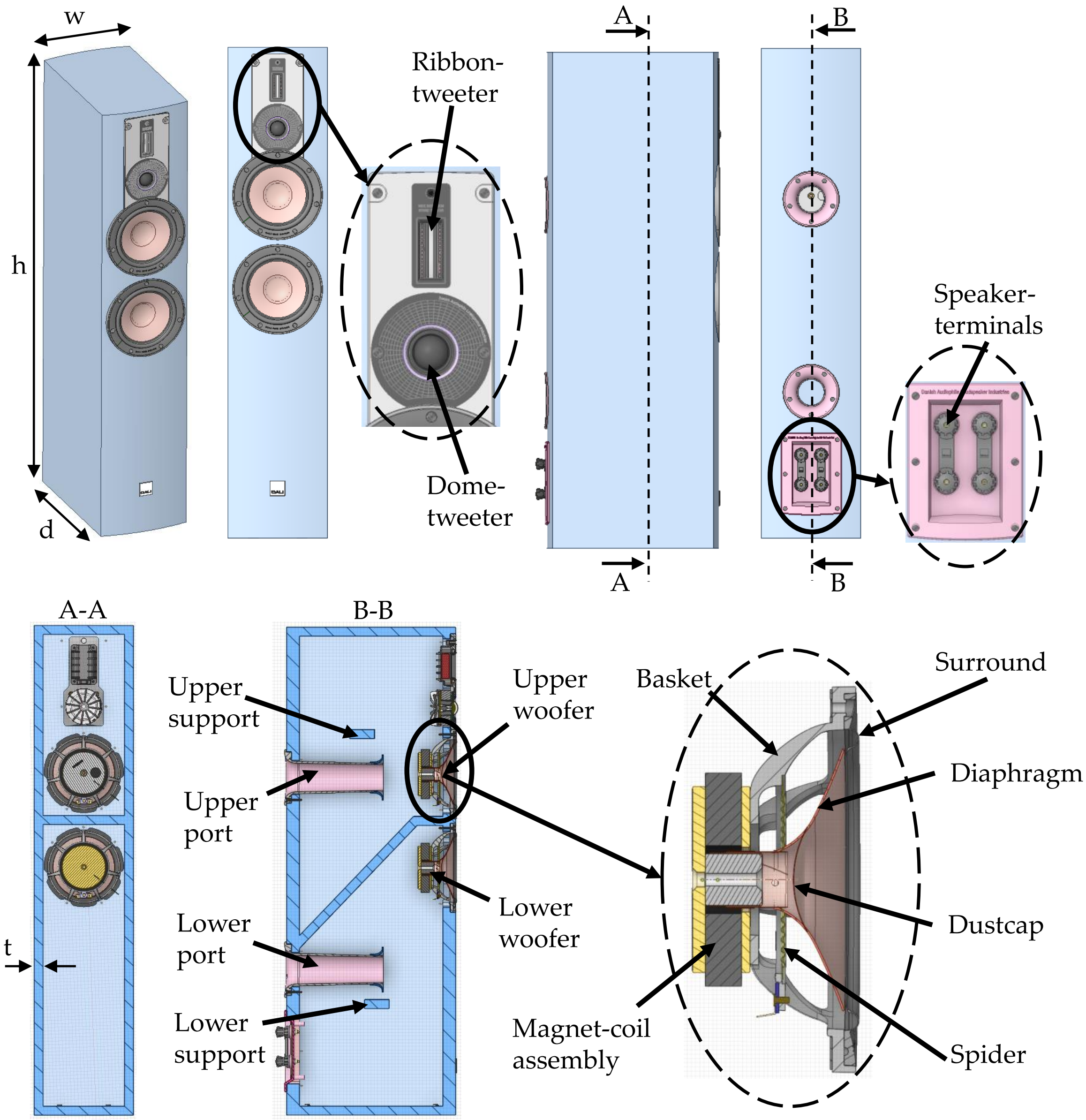

Figure 1.1: Overview of the Rubicon 6 loudspeaker and its components.

The loudspeaker has a height, h = 990mm, width, w = 200 mm and depth, d = 320mm. It consists of a cabinet divided into two cavities, each with a single internal support. The front face of the cabinet houses two woofers and a tweeter assembly, consisting of an aluminium plate, a dome tweeter, and a ribbon tweeter. Located on the back face of the cabinet are two bass reflex ports and speaker terminals. Not visualized in the figure is the crossover, located on the backside of the speaker terminals. The thickness of the cabinet sides is t = 18 mm. Looking at the woofer, it consists of a magnet-coil assembly that creates the motion which is transferred to the diaphragm and dust cap, which remains centred by the spider. All of these elements are assembled into the steel basket.

The driver in a loudspeaker transforms electric energy into mechanical energy. In a dynamic driver, such as the woofers in the Rubicon 6, this works by creating a magnetic field in a coil from the electrical signal, which then either is repelled or attracted by a passive magnet. This creates a linear movement of the coil. The coil is then connected to the diaphragm, which pushes air and creates a pressure difference that propagates through space that can be heard as sound. There are many other intricacies of how a loudspeaker works, however, this project will not focus on the electrical part of the loudspeaker design.

Theory 2

In this chapter, the theory relevant to the project is presented. Firstly, the theory of sound is presented, taking point of departure in 2D plane waves, to introduce the concepts such as the decibel scale and the equivalent radiated power level. Secondly, the theory of FEM modal and harmonic analysis is presented, as these two analyses constitute the benchmark and design model, developed in Chapters 4 and 5, respectively. Thirdly, damping is presented, as it will be introduced in both harmonic analyses. Lastly, optimization theory is presented.

2.1 Theory of sound

The concept of sound is introduced to describe how mechanical waves interact with the human ear. Sound is in its essence vibrations due to pressure fluctuations propagating as mechanical waves through a medium. Usually, the medium is a gas, e.g. air but can also be a liquid or a solid, as in the case of sound in water or structure-borne sound in solids. The sound spectrum is defined with respect to the audible frequency range of human hearing, which ranges from 20 Hz to 20 kHz. All frequencies below the lower limit are termed infrasound, while all frequencies above are termed ultrasound.

2.1.1 The wave equation for plane waves

In this section, the wave equation for plane waves propagating in a medium, such as air, is derived and explained. The derivations are based on [1, p. 9-13]. What we hear as sound is a propagating wave of fluctuating pressure in the air. As pressure is linearly proportional to the density, the fluctuation of pressure results in a fluctuation of density ρ. In (2.1) ρ_0 is the density in the undisturbed state, and ρ is the density at any point during the wave-propagation.

$$\begin{aligned} \frac{\rho - \rho_0}{\rho_0} &= \frac{\delta\rho}{\rho_0} = s \\ \rho &= \rho_0(1+s) \end{aligned} \tag{2.1}$$

s is now defined as the change in density, normalized with the density in the undisturbed state. This is termed condensation. This change in density gives rise to a change in volume, and a similar equation can be expressed in (2.2).

$$\begin{aligned} \frac{V - V_0}{V_0} &= \frac{\delta V}{V_0} = \Delta \\ V &= V_0(1+\Delta) \end{aligned} \tag{2.2}$$

Where V_0 is the volume in the undisturbed state, V is the volume at any point during the propagating wave, and Δ is the change in volume, normalized with the volume in the undisturbed state and is termed dilation. Boyle's gas law says that for any gas, the product between the pressure and volume in a gas is constant, which gives (2.3).

$$\begin{aligned} \rho V = V_0(1+\Delta)\rho_0(1+s) &= \rho_0 V_0 \\ (1+\Delta)(1+s) &= 1 \end{aligned} \tag{2.3}$$

It is assumed that the change in volume and density is much smaller than the volume and density in the undisturbed state, $s << 1$ and $\Delta << 1$. This can be used to linearize (2.3), such that $s = -\Delta$. This means that the characteristics of small changes in pressure and volume is linear. This is also established for the stress-strain relationship. Here the volumetric modulus of elasticity is denoted κ, and the volumetric strain is denoted $-\frac{\delta V}{V_0}$, and the stress in Pa is the change in pressure δp. This gives (2.4).

$$\begin{aligned} \delta p &= -\kappa \frac{\delta V}{V_0} \\ \kappa &= -\frac{V_0}{\delta V}\delta p = \frac{\delta p}{s} \end{aligned} \tag{2.4}$$

It is known that the total pressure p is the change in pressure, δp added to undisturbed pressure, p_0. This gives the following expression for the total pressure when inserting (2.4) and (2.1).

$$p = p_0 + \delta p = p_0 + \kappa s = p_0 + \kappa \frac{\delta \rho}{\rho_0} = p_0 + \kappa \left(\frac{\rho}{\rho_0} - 1 \right) \tag{2.5}$$

In the equations (2.4) and (2.5), κ is assumed constant when the variation in density is small enough that the pressure-density and pressure-volume characteristics can be considered linear. Now the concept of plane waves is introduced. Plane waves can be interpreted as waves, where the displacement u is constant at any point on each plane that extends infinitely in the two directions perpendicular to the direction of propagation. In Figure 2.1, an illustration of plane waves is made.

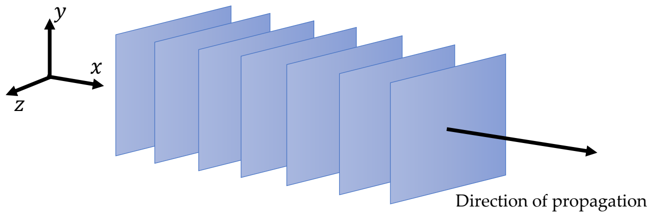

Figure 2.1: Illustration of plane waves. u displacement is along the x-axis.

Now, two planes in the propagating wave are visualized in Figure 2.2. In the figure, the two planes are δx apart and are denoted as AA and BB. The position of AA and BB are the locations of the planes in the undisturbed state. As the wave propagates the planes move such that they are now placed at $A'A'$ and $B'B'$. The displacement of the AA plane from the undisturbed to the disturbed state is denoted u.

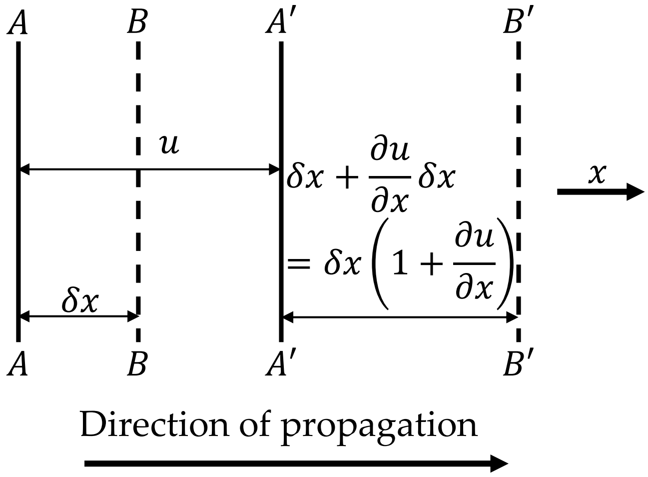

Figure 2.2: Two plane waves in an undisturbed and disturbed state.

In Figure 2.2, the distance between the two planes in the undisturbed state is δx. After the planes have moved the new distance is $\delta x \left(1 + \frac{\partial u}{\partial x}\right)$ when assuming that the distance δx is infinitesimal, such that $\frac{\partial u}{\partial x}$ is assumed constant. The distance between the two planes is therefore not the same in the undisturbed state and after the planes have been moved, however, the mass of the fluid between the planes remains the same. This means that a change in density occurs. The new distance is proportional with the factor $1 + \frac{\partial u}{\partial x}$, and the new volume between the planes is inversely proportional with the same factor. As the volume and density are proportional, the density can now be described in (2.6).

$$\begin{aligned}\rho &= \frac{\rho_0}{1+\frac{\partial u}{\partial x}}\\ \frac{\rho_0}{\rho} &= \left(1+\frac{\partial u}{\partial x}\right)\end{aligned} \tag{2.6}$$

.

Partial differentiation of (2.6) with respect to x gives (2.7).

$$\frac{\partial \rho}{\partial x} = -\rho_0 \frac{\frac{\partial^2 u}{\partial x^2}}{\left(1+\frac{\partial u}{\partial x}\right)^2} \tag{2.7}$$

Inserting (2.6) into (2.7) gives (2.8).

$$\begin{aligned}\frac{\partial \rho}{\partial x} &= -\rho_0 \frac{\frac{\partial^2 u}{\partial x^2}}{\left(\frac{\rho_0}{\rho}\right)^2}\\ -\frac{1}{\rho_0}\frac{\partial \rho}{\partial x} &= \left(\frac{\rho}{\rho_0}\right)^2 \frac{\partial^2 u}{\partial x^2}\end{aligned} \tag{2.8}$$

Multiplying with $\frac{\partial p}{\partial \rho}$ gives (2.9).

$$-\frac{1}{\rho_0}\frac{\partial p}{\partial x} = \left(\frac{\rho}{\rho_0}\right)^2 \frac{\partial p}{\partial \rho}\frac{\partial^2 u}{\partial x^2} \tag{2.9}$$

Now the restoring forces acting on a unit area of the plane, i.e. the pressure, can be found by using Newton's second law of motion $F = ma$. Here it is assumed that the change is infinitesimal, such that $\frac{\delta p}{\delta x} = \frac{\partial p}{\partial x}$.

$$\begin{aligned}\delta p &= -\rho_0 \delta x \frac{\partial^2 u}{\partial t^2}\\ -\frac{1}{\rho_0}\frac{\partial p}{\partial x} &= \frac{\partial^2 u}{\partial t^2}\end{aligned} \tag{2.10}$$

Equating (2.10) to (2.9) gives (2.11).

$$\frac{\partial^2 u}{\partial t^2} = \left(\frac{\rho}{\rho_0}\right)^2 \frac{\partial p}{\partial \rho}\frac{\partial^2 u}{\partial x^2} \tag{2.11}$$

Now partial differentiation of the pressure in (2.5) with respect to the density gives (2.12).

$$\frac{\partial p}{\partial \rho} = \frac{\kappa}{\rho_0} \tag{2.12}$$

Further assuming that $\delta\rho << \rho$ such that $\rho_0 \approx \rho$ and inserting (2.12) in (2.11), the wave equation in (2.13) is obtained.

$$\frac{\partial^2 u}{\partial t^2} = \frac{\kappa}{\rho}\frac{\partial^2 u}{\partial x^2} \tag{2.13}$$

Where $\frac{\kappa}{\rho} = c^2$ and c is the speed of wave propagation in the analyzed medium.

2.1.2 The decibel scale

Dealing with sound in the audible range, as opposed to e.g. ultrasound, the loudness of the sound as perceived by the human ear is often of interest to the engineer. This is especially the case in this project, as improving the perceived sound quality of the loudspeaker is the ultimate goal of a loudspeaker manufacturer. Sound quality is an abstract concept that is difficult to quantify, the same goes for perceived loudness, albeit a little less abstract. Human hearing perceives loudness as somewhat logarithmically. This is a very crude assumption that in no way is true throughout the entire audible frequency spectrum, however, it does exemplify the practicality of a logarithmic scale when dealing with sound. The decibel scale was invented to make it more convenient to relate the difference in power and pressure between two sources to each other in relation to the human ear. In (2.14) the definition of the decibel in terms of the power ratio between a reference power, P_0, and power, P, is defined as the base-10 logarithm of the ratio. [1, p. 7]

$$10\log_{10}\left(\frac{P}{P_0}\right)\,\mathrm{dB} \tag{2.14}$$

This definition means that doubling the power results in an $\approx 3\,\mathrm{dB}$ increase, as $10\log_{10}(2) = 3.01\,\mathrm{dB}$. Doubling the power once again corresponds to an $\approx 6\,\mathrm{dB}$ increase and so forth. Specifying the power in dB is defined as the sound power level. Setting the reference power as the lowest audible power a human can hear, $1 \times 10^{-12}\,\mathrm{W}$, makes for a convenient scale, where the lowest audible sound corresponds to a sound power level of $0\,\mathrm{dB}$, while e.g. a fighter jet during take-off corresponds to $150\,\mathrm{dB}$, having a sound power of $10 \times 10^3\,\mathrm{W}$. [6]

The sound pressure can likewise be specified as a sound pressure level in dB, where the definition in (2.15) is used. The factor of 2 is introduced such that an increase of $3\,\mathrm{dB}$ in the sound power level also corresponds to a $3\,\mathrm{dB}$ increase in the sound pressure level, as the power is proportional to the pressure squared and $\log_{10}(x^2) = 2\log_{10}(x)$.

$$10\log_{10}\left(\frac{p^2}{p_0^2}\right)\,\mathrm{dB} = 20\log_{10}\left(\frac{p}{p_0}\right)\,\mathrm{dB} = 10\log_{10}\left(\frac{P}{P_0}\right)\,\mathrm{dB} \tag{2.15}$$

2.1.3 Equivalent radiated power

The equivalent radiated power (ERP) is a simplified method for the calculation of the radiated acoustic power that is transmitted from a vibrating surface. This method is advantageous to use for optimization problems that require many iterations of evaluations for objective functions. The alternative to the ERP calculation is a coupled multi-physics simulation. Such a simulation could be an acoustic-structure interaction, often performed for simple geometries in the simulation program COMSOL in industry. This is however often very computationally costly due to the additional DoF required to discretize the air surrounding the structural components and the coupling of the structure and the air. The ERP is therefore used in this project. The theory presented in this section is based on [7] and the theory presented in Section 2.1.1.

To understand the equivalent radiated power the concept of acoustic intensity I must be understood. The intensity has the unit $\frac{W}{m^2}$, such that it is the power carried by the pressure waves per unit area. The intensity is found by the pressure p and the velocity v in (2.16).

$$\{I\} = p\{v\} \tag{2.16}$$

The power W that is carried over a surface S is then found by integrating the intensity over the surface.

$$W = \Re\left(\int_S \{I\} dS\right) \tag{2.17}$$

This calculation however requires knowledge of the pressure p for each node in the simulation. However, the assumption of plane waves and the introduction of the acoustic impedance allows for the calculation of the radiated power without knowing the pressure. Plane waves are characterized by the displacement only being a function of one dimension, as the displacement is assumed constant over any plane perpendicular to the direction of wave propagation. The acoustic impedance Z, can be understood as a measure of the opposition of wave-propagation in the medium in which the wave propagates. It is defined in (2.18), for plane waves where $p(x,t)$ is the change in pressure and $v(x,t)$ is the particle velocity.

$$Z = \frac{p(x,t)}{v(x,t)} \tag{2.18}$$

Assuming harmonic sinusoidal displacements $u(x,t)$, with amplitude A, angular frequency ω and wavenumber k gives the expression for the particle velocity in (2.20).

$$u(x,t) = Asin(kx - \omega t) \tag{2.19}$$
$$v(x,t) = -\omega Acos(kx - \omega t) \tag{2.20}$$

The wavenumber, k, is the spatial frequency and is defined as $k = \frac{2\pi}{\lambda}$ and is the number of radians per unit distance. Inserting (2.19) into the wave equation in (2.13), and partial differentiation with respect to time t and position x twice, gives (2.21). It is now immediately obvious that the wave-propagation speed can be described by the wavenumber and angular frequency.

$$\begin{aligned} -A\omega^2 sin(kx - \omega t) &= -c^2 Ak^2 sin(kx - \omega t) \\ c^2 &= \frac{\omega^2}{k^2} \\ c &= \frac{\omega}{k} \end{aligned} \tag{2.21}$$

Now recalling (2.4 on page 4), and assuming plane waves, the pressure increase can now be described by (2.23).

$$p(x,t) = -\kappa \frac{\partial u(x,t)}{\partial x} \tag{2.22}$$
$$p(x,t) = -k\kappa Acos(kx - \omega t) \tag{2.23}$$

Now substitution of (2.20), (2.21) and (2.23) into (2.18) and recalling that $\frac{\kappa}{\rho} = c^2$ gives (2.24).

$$Z = \frac{p(x,t)}{v(x,t)} = \rho c \tag{2.24}$$

It should be noted that the acoustic impedance is not a function of time or space, as it is described by the constants ρ and c. This also implies that the ratio between the pressure change and the particle velocity remains the same at all points in time and space. In other words, by assuming plane waves, it is also assumed that the pressure increase and particle velocity are in phase. The implication is that the amplitudes of the pressure increase and the particle velocity, $\hat{p}$ and $\hat{v}$, respectively, can be substituted into (2.24), and further rewriting gives an expression for the pressure amplitude.

$$\hat{p} = \rho c \hat{v} \tag{2.25}$$

The amplitude of change in pressure, $\hat{p}$, can now, by assuming plane waves, be described by the density of the medium, ρ, the speed of wave propagation, c, and the amplitude of the particle velocity, $\hat{v}$. This reduces the task of calculating the power output to only being able to find the particle velocity at the surface of interest. This simplified method for calculating the acoustic power is seen in (2.26).

$$W = \rho c \int_S \hat{v}^2 dS \tag{2.26}$$

The last assumption made before being able to calculate the ERP, is the assumption that the particle velocity of the medium at the boundary of a vibrating structure is equal to the normal velocity of the surface of the structure. In other words, it is assumed that the fluid cannot support shear stresses. This gives that $\hat{v} = \hat{v}_n$, at the surface of a structure, where $\hat{v}_n$ is the amplitude of the velocity of the structure, normal to the surface. This gives the expression for the ERP in (2.27).

$$ERP = \rho c \int_S \hat{v}_n^2 dS \tag{2.27}$$

Now it can be advantageous to convert into a decibel scale such that the Equivalent Radiated Power Level (ERPL) is obtained by (2.28).

$$ERPL = 10log_{10}\left(\frac{ERP}{P_0}\right) dB \tag{2.28}$$

As was mentioned, it can be advantageous to use the ERP as a metric in numerical models that require several evaluations, such as the case of optimization problems using FEA, as only the velocity of the structure is needed, rather than the velocity and pressure fields in the surrounding fluid. This is done by being able to substitute the pressure in the surrounding fluid by (2.25), and then assuming that the velocity of the fluid at the boundary is equal to that of the normal velocities of the structure. However, this metric is based on the plane wave assumption, which results in over-predictions in the radiated power. This over-prediction stems from the fact that the normal surface velocities are squared in (2.27). This means that the phase shift between the velocity and pressure is neglected, effectively resulting in that destructive interference is not captured as the pressure and velocity are assumed to be in phase. This is especially true for mode shapes of higher order, as more interference is typically associated with these.

2.2 Theory of modal analysis

A modal analysis is a linear analysis that determines the eigenfrequencies and mode shapes for free vibrations of a system. The theory described in this chapter on modal analysis is based on [8, p. 581-585]. The dynamic equilibrium equation for a linear elastic system is seen in (2.29). In this equation, $[m]$ is the mass matrix, $[c]$ is the damping matrix, and $[k]$ is the stiffness matrix. $\{u(t)\}$ is displacement, $\{\dot{u}(t)\}$ is velocity and $\{\ddot{u}(t)\}$ is acceleration. Lastly $\{F^{ext}(t)\}$ is the external force acting on the system.

$$[m]\{\ddot{u}(t)\} + [c]\{\dot{u}(t)\} + [k]\{u(t)\} = \{F^{ext}(t)\} \tag{2.29}$$

Here it is assumed that no damping is present, $[c] = 0$, which results in the second term in (2.29) being equal to zero. Additionally, the modal analysis assumes free vibration, which means that there is no external forcing imposed on the system, $\{F^{ext}(t)\} = 0$. This reduces the dynamic equilibrium equation to (2.30).

$$[m]\{\ddot{u}(t)\} + [k]\{u(t)\} = 0 \tag{2.30}$$

Additionally, it is assumed that the response is harmonic which means that the displacements $\{u(t)\}$ vary sinusoidally with time t. From this the two unknowns in (2.30), $\{u(t)\}$ and $\{\ddot{u}(t)\}$, can be expressed as seen in (2.31) and (2.32).

$$\{u\} = \{\Phi_i\}cos(\omega_i t) \tag{2.31}$$
$$\{\ddot{u}\} = -\omega_i^2\{\Phi_i\}cos(\omega_i t) \tag{2.32}$$

Here, $\{\Phi_i\}$ are the nodal amplitudes, which is also called the mode shape vector and ω_i is the angular frequency. Now (2.31) and (2.32) can be inserted into (2.30), giving (2.33).

$$([k] - \omega_i^2[m])\{\Phi_i\} = 0 \tag{2.33}$$

This equation is an eigenvalue problem, where both the eigenvalues, ω_i and eigenvectors $\{\Phi_i\}$, henceforth called the eigenfrequencies, and mode shape vectors, are sought. In order to find non-trivial solutions to this problem the determinant of the matrix is set equal to zero, which yields the characteristic equation, in (2.34).

$$|[k] - \omega_i^2[m]| = 0 \tag{2.34}$$

The eigenfrequencies ω_i can be found by solving for the roots of the characteristic polynomial. The number of eigenfrequencies for a given system equals the DoF for that system. When implemented in FEA, there are 3 DoF for each node in solid elements. This often results in a number of DoF that is impractical to solve. An n-DoF system results in an n-degree polynomial, often resulting in the polynomial becoming ill-conditioned, even for relatively small values of n. In addition to this, not all eigenfrequencies are of equal importance to the engineer performing the modal analysis. As a result, several algorithms for finding good approximations of a predetermined number of eigenfrequencies have been developed.

When then the eigenfrequencies are found, the mode shapes are found by simply substituting the eigenfrequencies into (2.33) and solving for $\{\Phi_i\}$. It should be noted that any arbitrary scalar can be multiplied on the mode shape vector with the equation still being satisfied. This is the reason that they are called mode shapes instead of displacements, as they simply carry information about the shape of the system and how the nodal displacements relate to each other, rather than information on absolute displacements.

As the magnitude of the mode shape is arbitrary, many conventions for normalizing the mode shape vector are used. One such convention is normalizing the mode shape such that the magnitude of the mode shape equals unity. Another convention is the mass-normalised mode shapes. The mass-normalization of the mode shapes has some traits that will be used in the harmonic analysis and the theory based on [8, p. 591-592] is therefore explained in brief here. One property of mode shapes is their orthogonality with respect to the mass- and stiffness-matrix, $[m]$ and $[k]$, see (2.35) and (2.36).

$$\{\Phi_j\}^T[m]\{\Phi_i\} = 0, \qquad i \neq j \tag{2.35}$$
$$\{\Phi_j\}^T[k]\{\Phi_i\} = 0, \qquad i \neq j \tag{2.36}$$

This property is, in general true, however, when twin modes appear, such that $\omega_i = \omega_j$ the associated mode shapes are not orthogonal to each other, but are still orthogonal to all other mode shapes. The property of orthogonality can be used to generate the generalized mass- and stiffness-matrices in (2.37) and (2.38).

$$[\Phi]^T[m][\Phi] = \begin{bmatrix} M_{11} & 0 & \dots & 0 \\ 0 & M_{22} & \dots & 0 \\ \vdots & \vdots & \ddots & \vdots \\ 0 & 0 & \dots & M_{nn} \end{bmatrix} = [\nwarrow M \searrow] \tag{2.37}$$

$$[\Phi]^T[k][\Phi] = \begin{bmatrix} K_{11} & 0 & \dots & 0 \\ 0 & K_{22} & \dots & 0 \\ \vdots & \vdots & \ddots & \vdots \\ 0 & 0 & \dots & K_{nn} \end{bmatrix} = [\nwarrow K \searrow] \tag{2.38}$$

Here $[\Phi]$ is the modal matrix, $[\Phi] = [\{\Phi_1\}\{\Phi_2\}\dots\{\Phi_n\}]$. Now the mode shapes can be normalized such that $[\nwarrow M \searrow] = [I]$. Mode shapes that fulfil this are called mass-normalized modes shapes. From (2.37) it is evident that mass normalized mode shapes, $\{\hat{\Phi}_i\}$ fulfill (2.39).

$$\{\hat{\Phi}_i\}^T[m]\{\hat{\Phi}_i\} = 1 \tag{2.39}$$

It is clear that in order for (2.39) to be fulfilled, a normalization factor, N_i must be found and multiplied to the original mode shape, such that $\{\hat{\Phi}_i\} = N_i\{\Phi_i\}$. Inserting this into (2.39) and solving for the normalization factor gives (2.40).

$$\begin{aligned} N_i\{\Phi_i\}^T[m]N_i\{\Phi_i\} &= N_i^2(\{\Phi_i\}^T[m]\{\Phi_i\}) = 1 \\ N_i &= \frac{1}{\sqrt{\{\Phi_i\}^T[m]\{\Phi_i\}}} = \frac{1}{\sqrt{M_{ii}}} \end{aligned} \tag{2.40}$$

Now the mass normalized mode shape can be found using the normalization factor.

$$\{\hat{\Phi}_i\} = \frac{\{\Phi_i\}}{\sqrt{M_{ii}}} \tag{2.41}$$

Using the mass-normalized mode shapes $\{\hat{\Phi}_i\}$, the general mass matrix is now the identity matrix.

$$[\hat{\Phi}]^T[m][\hat{\Phi}] = \begin{bmatrix} 1 & 0 & \dots & 0 \\ 0 & 1 & \dots & 0 \\ \vdots & \vdots & \ddots & \vdots \\ 0 & 0 & \dots & 1 \end{bmatrix} = [I] \tag{2.42}$$

Additionally, when the mode shapes are mass-normalized, it is obvious from (2.33) that the general stiffness matrix can be reduced to (2.43).

$$[\hat{\Phi}]^T[k][\hat{\Phi}] = \begin{bmatrix} \omega_1^2 & 0 & \dots & 0 \\ 0 & \omega_2^2 & \dots & 0 \\ \vdots & \vdots & \ddots & \vdots \\ 0 & 0 & \dots & \omega_n^2 \end{bmatrix} = [\nwarrow \omega_i^2 \searrow] \tag{2.43}$$

The reduction of the general mass- and stiffness-matrices when using mass-normalized mode shapes will become important in the theory of harmonic analysis in the following section.

2.3 Theory of harmonic analysis

The harmonic analysis aims to compute the steady-state response of the system when imposed with a load that varies harmonically (sinusoidally) with time. This is done in the frequency domain, where a solution is found for each specified frequency of the imposed load. For a harmonic analysis, the mode shapes and eigenfrequencies found in the modal analysis are used in the computation, and having performed a modal analysis of the system is therefore mandatory before the harmonic analysis can be performed. The theory of the harmonic analysis using mode superposition is based on [8, p. 596-613], [9] and [10]. In order to understand the theory behind a harmonic analysis, let us recall the dynamic equilibrium equation for linear elastic systems. The equation is stated in (2.29) and is restated here in (2.44).

$$[m]\{\ddot{u(t)}\} + [c]\{\dot{u(t)}\} + [k]\{u(t)\} = \{F^{ext}(t)\} \tag{2.44}$$

It is assumed that the response of the system varies sinusoidally with time. This gives the expression for the load, displacements, velocity and acceleration in (2.45), (2.46), (2.47) and (2.48), respectively.

$$\{F^{ext}(t)\} = \{F\}e^{i\Omega t} \tag{2.45}$$
$$\{u(t)\} = \{u\}e^{i\Omega t} \tag{2.46}$$
$$\{\dot{u(t)}\} = i\Omega\{u\}e^{i\Omega t} \tag{2.47}$$
$$\{\ddot{u(t)}\} = -\Omega^2\{u\}e^{i\Omega t} \tag{2.48}$$

Ω is the imposed frequency of the load, while $\{u\}$ are the nodal amplitudes. Now, the concept of mode superposition is introduced. The basis of this concept comes from the expansion theorem. This theorem states that any vector in the n-dimensional space can be formed by a linear combination of the n linearly independent vectors. Vectors are called linearly independent when no vector in the set can be obtained by a linear combination of the remaining vectors. In the case of mode shapes, due to their orthogonality, they are linearly independent. Thus, a linear combination of all mode shapes in a system can express any vector in the n-dimensional space. This means that the displacements can be expressed in terms of a linear combination of the mode shapes.

$$\{u(t)\} \approx \sum_{i=1}^{n} \{\hat{\Phi}_i\} q_i(t) \tag{2.49}$$

In the equation $q_i(t)$ is called the modal amplitude and is a scalar for each mode shape in the model. The magnitude of this scalar represents how much a given mode shape "dominates" in the response of the system. If all the mode shapes in the system are used, then the solution would be exact. However, as not all mode shapes are found, the solution is only approximate. Now (2.49) can be expressed in matrix form, and a harmonic time-dependence is assumed. Additionally, the velocity and acceleration can also be expressed.

$$\{u(t)\} = [\hat{\Phi}]\{q\}e^{i\Omega t} \tag{2.50}$$
$$\{u(\dot{t})\} = i\Omega[\hat{\Phi}]\{q\}e^{i\Omega t} \tag{2.51}$$
$$\{u(\ddot{t})\} = -\Omega^2[\hat{\Phi}]\{q\}e^{i\Omega t} \tag{2.52}$$

Inserting (2.45), (2.50), (2.51) and (2.52) into (2.44), and omitting the time dependency, yields (2.53).

$$-\Omega^2[m][\hat{\Phi}]\{q\} + i\Omega[c][\hat{\Phi}]\{q\} + [k][\hat{\Phi}]\{q\} = \{F\} \tag{2.53}$$

Utilizing the properties of the mass-normalized mode shapes, discussed in Section 2.2, pre-multiplying (2.53) with $[\hat{\Phi}]^T$ gives (2.54).

$$\begin{aligned} -\Omega^2[\hat{\Phi}]^T[m][\hat{\Phi}]\{q\} + i\Omega[\hat{\Phi}]^T[c][\hat{\Phi}]\{q\} + [\hat{\Phi}]^T[k][\hat{\Phi}]\{q\} &= [\hat{\Phi}]^T\{F\} \\ -\Omega^2[I]\{q\} + i\Omega[\hat{\Phi}]^T[c][\hat{\Phi}]\{q\} + [\nwarrow \omega_i^2 \searrow]\{q\} &= \{r\} \end{aligned} \tag{2.54}$$

Here, $\{r\} = [\hat{\Phi}]^T\{F\}$ is called the modal load and is essentially a projection of the external load onto each mode shape. If this projection is small, it also yields small modal amplitudes for that given mode and vice versa. Additionally, its seen that (2.54) only has one coupling term. Both the mass- and stiffness terms are diagonal and are therefore uncoupled, but the damping term is still a coupling term. However, it is often assumed that the modal damping matrix is diagonal, such that the problem can be decomposed into a set of uncoupled equations. The theory of damping is explained in further detail in Section 2.4, but in this section, it is explained how Rayleigh damping can be used to decouple the system of equations. A commonly used damping model is Rayleigh damping, which assumes that the damping term is a linear combination of the mass- and stiffness-matrices.

$$[c] = \alpha[m] + \beta[k] \tag{2.55}$$
$$\zeta_i = \frac{\alpha}{2\omega_i} + \frac{\beta\omega_i}{2}, \qquad \alpha = 2\zeta_i\omega_i - \beta\omega_i^2, \qquad \beta = \frac{2\zeta_i}{\omega_i} - \frac{\alpha}{\omega_i^2} \tag{2.56}$$

Inserting (2.56) into (2.55) and further inserting that into the second term in (2.54) on vector form gives the damping term (2.57).

$$i\Omega[\hat{\Phi}]^T[c][\hat{\Phi}]\{q\} = i\Omega\{\hat{\Phi}_i\}^T\left[(2\zeta_i\omega_i - \beta\omega_i^2)[m] + \left(\frac{2\zeta_i}{\omega_i} - \frac{\alpha}{\omega_i^2}\right)[k]\right]\{\hat{\Phi}_i\}q_i \tag{2.57}$$

As was done earlier, the generalized mass- and stiffness-matrices when the mode shapes are mass-normalized from (2.43) and (2.42) are used. Additionally, the definition of α from (2.56) is inserted.

$$i\Omega\left[2\zeta_i\omega_i - \beta\omega_i^2 + \left(\frac{2\zeta_i}{\omega_i} - \frac{\alpha}{\omega_i^2}\right)\omega_i^2\right]q_i = i\Omega 2\zeta_i\omega_i q_i \tag{2.58}$$

This can be inserted into (2.54), which now can be written as a set of uncoupled equations on the form in (2.59).

$$\begin{aligned}(-\Omega^2 + i\Omega 2\zeta_i\omega_i + \omega_i^2)q_i &= r_i \\ q_i &= \frac{r_i}{-\Omega^2 + i\Omega 2\zeta_i\omega_i + \omega_i^2}\end{aligned} \tag{2.59}$$

Finally, the modal amplitudes can be inserted into (2.49), and the approximate steady-state response of the system when imposed with a sinusoidally varying load at the frequency Ω is found. An interesting point to note is that, in the case of an undampened system, $\zeta_i = 0$, and as the excitation frequency, Ω, approaches any eigenfrequency of the system, the modal amplitude associated with the corresponding mode shape approaches infinity. This gives infinite displacements and is non-physical. Therefore some damping should be used, $\zeta_i \neq 0$, when performing the harmonic analysis. It is evident that the modal amplitudes are complex numbers in the complex plane. This can be seen in Figure 2.3.

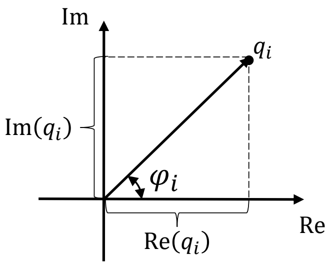

Figure 2.3: Modal amplitude in the complex plane

Looking at the complex plane, the modal amplitude can be expressed as seen in (2.60).

$$q_i = \sqrt{\Re(q_i)^2 + \Im(q_i)^2} \tag{2.60}$$

And the angle, φ, is the phase angle between the external forcing and the response of the system. In Figure 2.4, the modal amplitude, q_i, and phase angle, φ_i, are shown as a function of the unit less $\frac{\Omega}{\omega}$ with $r_i = 1$, with different damping ζ_i.

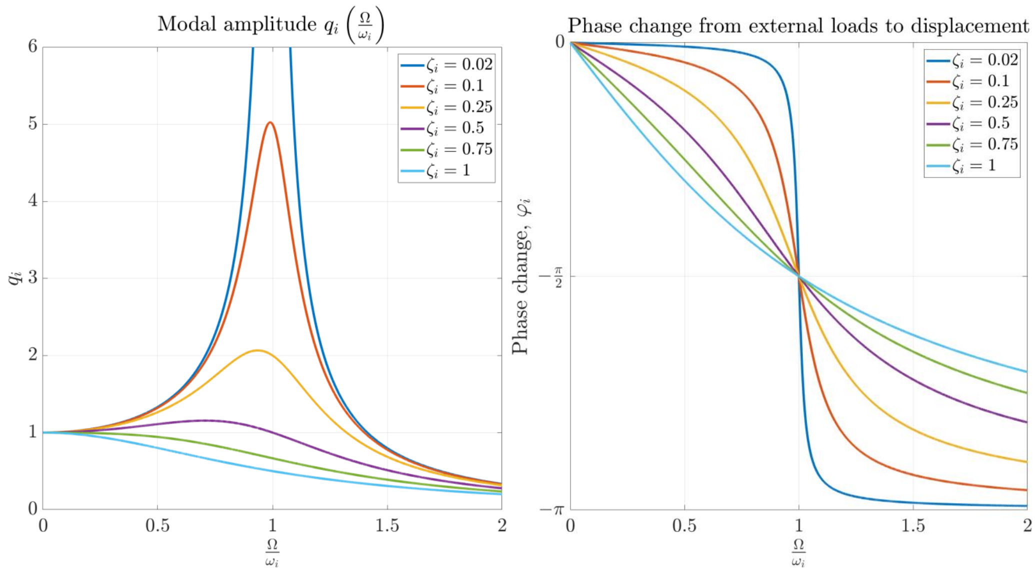

Figure 2.4: Effect of damping on modal amplitudes and phases.

It is also evident from (2.59) that the modal amplitude of any mode is limited to the term $\frac{r_i}{i\Omega 2\zeta_i\omega_i}$. This is visually seen in Figure 2.5, where the modal amplitudes for eight modes are shown with $r_i = 1$, $\zeta_i = 0.01$ along with the term. Here it is evident that the modal amplitudes are lower due to this term when located at increasing frequencies, despite the external forcing and damping remaining the same.

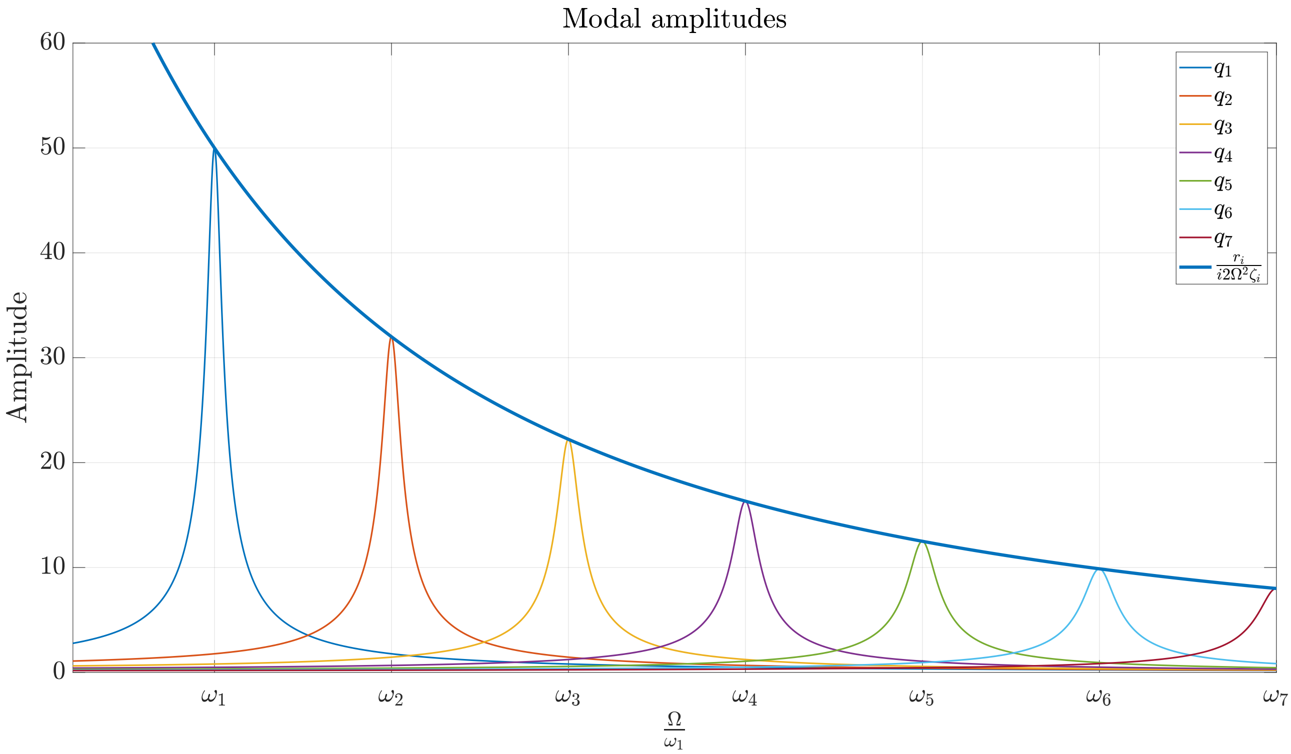

Figure 2.5: Effect of the position of ω_i on modal amplitudes.

2.4 Theory of damping

All practical systems are damped, meaning that energy is dissipated as heat or sound when the system is oscillating, such that the system eventually comes to a halt. The dissipation of energy to heat and sound is difficult to model accurately and thus different approaches depending on the physical system of interest are used. In the context of the speaker cabinet, two overall ways of modelling damping are of interest; viscous and hysteresis damping. Viscous damping is most often used to model the dissipation of energy in systems surrounded by a fluid such as air, water or oil. The damping force for viscous damping is proportional to the velocity of the vibrating body. Hysteresis damping on the other hand is proportional to the amplitude of displacement and is thus independent of the frequency. This is because hysteresis damping is inherent to the material and represents energy dissipation due to small plastic deformation despite only having strains in the elastic range. [11, p. 388].

In most physical systems, both viscous and hysteresis damping are present and contribute to the decrease of the amplitude of oscillations over time. However, as stated in [11, p. 389], most damping in physical systems loaded in the elastic range is sufficiently small to accurately model the response of the system using the formulation for viscous damping only. Viscous damping is advantageous to hysteresis damping as it is easier to introduce in the dynamic equilibrium equation, [8, p. 613], and makes it possible to decouple the equations in a FEM context, as was shown in the previous Section 2.3. For these reasons, viscous damping is used in this project to model the entire damping in the system.

2.4.1 Viscous damping

Viscous damping is easily introduced in the dynamic equilibrium equation for a single DoF system (2.61) for damped free vibrations.

$$m\ddot{u} + c\dot{u} + ku = 0 \tag{2.61}$$

Assuming a time-dependent harmonic solution (2.62), where C and s are undetermined constants.

$$u(t) = Ce^{st} \tag{2.62}$$

Inserting (2.62) in (2.61) and taking the derivative with respect to time twice yields the characteristic equation (2.63).

$$ms^2 + cs + k = 0 \tag{2.63}$$

Solving the polynomial for the two solutions of s, $s_{1,2}$, that satisfies the characteristic equation yields (2.64).

$$s_{1,2} = \frac{-c \pm \sqrt{c^2 - 4mk}}{2m} = -\frac{c}{2m} \pm \sqrt{\left(\frac{c}{2m}\right)^2 - \frac{k}{m}} \tag{2.64}$$

Inserting (2.64) into (2.62) yields the general solution (2.65) to the dynamic equilibrium equation and is a combination of the two solutions $s_{1,2}$. Here C_1 and C_2 are arbitrary constants, which satisfy the initial conditions of initial displacement and initial velocity.

$$u(t) = C_1 e^{s_1 t} + C_2 e^{s_2 t} = C_1 e^{\left(-\frac{c}{2m} + \sqrt{\left(\frac{c}{2m}\right)^2 - \frac{k}{m}}\right)t} + C_2 e^{\left(-\frac{c}{2m} - \sqrt{\left(\frac{c}{2m}\right)^2 - \frac{k}{m}}\right)t} \tag{2.65}$$

Next, the concept of critical damping is introduced as the value of damping c_c at which the system comes to rest as fast as possible without any oscillations. This happens when the square roots in the exponentials in (2.65) are equal to 0. Also, exploiting that the natural frequency is defined as $\omega_n = \sqrt{\frac{k}{m}}$, the critical damping is defined as:

$$\sqrt{\left(\frac{c_c}{2m}\right)^2 - \frac{k}{m}} = 0 \Rightarrow c_c = 2m\sqrt{\frac{k}{m}} = 2m\omega_n \tag{2.66}$$

Introducing the damping ratio, ζ, as the ratio between the amount of damping and the critical damping, $\frac{c}{c_c}$, the following relation between c, ζ and ω_n is stated:

$$\frac{c}{2m} = \zeta\omega_n \tag{2.67}$$

Inserting (2.67) into (2.65) defines the general solution using the damping ratio and the natural frequency:

$$u(t) = C_1 e^{\left(-\zeta+\sqrt{\zeta^2-1}\right)\omega_n t} + C_2 e^{\left(-\zeta-\sqrt{\zeta^2-1}\right)\omega_n t} \tag{2.68}$$

The solution has 4 different forms depending on the value of the damping ratio, where only the case of an undamped and underdamped system is of relevance in this project:

$\zeta = 0$	Undamped
$0 < \zeta < 1$	Underdamped
$\zeta = 1$	Critically damped
$1 < \zeta$	Overdamped

When the system is undamped the solution of course becomes identical to (2.31), albeit in the exponential form and for a single DoF system here, while C simply represents the amplitude. The choice between the two solutions in (2.69) is arbitrary as long as the sign in the special solution, $u(x)$, is then chosen accordingly to the sign choice in the time-dependent solution.

$$u(t) = Ce^{\pm\sqrt{-1}\omega_n t} = Ce^{\pm i\omega_n t} \tag{2.69}$$

In the case of the underdamped system, the term in the square root will always be negative. The solution is rewritten by replacing $\sqrt{\zeta^2 - 1}$ with $i\sqrt{1 - \zeta^2}$ and by separating the real and imaginary exponents:

$$u(t) = e^{-\zeta\omega_n t} Ce^{\pm i\sqrt{1-\zeta^2}\omega_n t} \tag{2.70}$$

From (2.70) it is apparent that the first term represents an exponential decrease, while the second term is a harmonic oscillation. Multiplying the two terms together results in the expected response, i.e. a harmonic oscillation, where the amplitude decreases exponentially each cycle, from this it is also apparent that viscous damping is indeed frequency dependant. The frequency that the system will oscillate with is called the damped natural frequency, ω_d, and will always be lower than the undamped natural frequency, as ω_d is defined from the exponent in the second term (2.71).

$$\omega_d = \sqrt{1 - \zeta^2}\omega_n \tag{2.71}$$

From (2.71), it is immediately obvious that for $\zeta << 1$, as is the case for all materials used in the cabinet in this project, then $\omega_d \approx \omega_n$. This means that the assumption of zero damping when performing the modal analysis, only results in insignificant differences in the location of the eigenfrequencies when compared to the case of damped eigenfrequencies.

2.4.2 Rayleigh and modal damping

The concept of viscous damping, the damping ratio and the damped natural frequency was introduced taking point of departure in a one DoF system. However, introducing damping for each DoF in a system, couples the equations, i.e. damping in one mode shape affects the damping in other mode shapes as well. A smart way of defining viscous damping was shown in Section 2.3, namely Rayleigh damping, which makes it possible to decouple the equations.

Rayleigh damping works by defining the damping matrix as a linear combination of the stiffness and mass matrix by introducing the two constants α and β. Here α and β are defined in such a way that the damping term can be decoupled later. Equations (2.55) and (2.56) are restated below as (2.72) and (2.73).

$$[c] = \alpha[m] + \beta[k] \tag{2.72}$$

$$\zeta_i = \frac{\alpha}{2\omega_i} + \frac{\beta\omega_i}{2}, \qquad \alpha = 2\zeta_i\omega_i - \beta\omega_i^2, \qquad \beta = \frac{2\zeta_i}{\omega_i} - \frac{\alpha}{\omega_i^2} \tag{2.73}$$

Rewriting (2.73) such that an expression for the damping ratio for each term is defined yields (2.74).

$$\zeta_i = \frac{\alpha}{2\omega_i} + \frac{\beta\omega_i}{2}, \qquad \zeta_{\alpha,i} = \frac{\alpha}{2\omega_i}, \qquad \zeta_{\beta,i} = \frac{\beta\omega_i}{2} \tag{2.74}$$

Figure 2.6 plots the damping ratio as a function of the frequency for the mass and stiffness proportional terms and the combination of the two, i.e. the equations in (2.74). The figure also illustrates how the constants α and β are practically defined for a physical system, assuming that a constant damping ratio in the entire frequency range of interest is the goal. The damping ratio at the first frequency of interest, ω_1, and the last, ω_n, is forced to a constant value of $\zeta_{1,n}$ and the equations are solved for α and β. The damping ratio is thus close to linear, but lower, in the frequency range between ω_1 and ω_n.

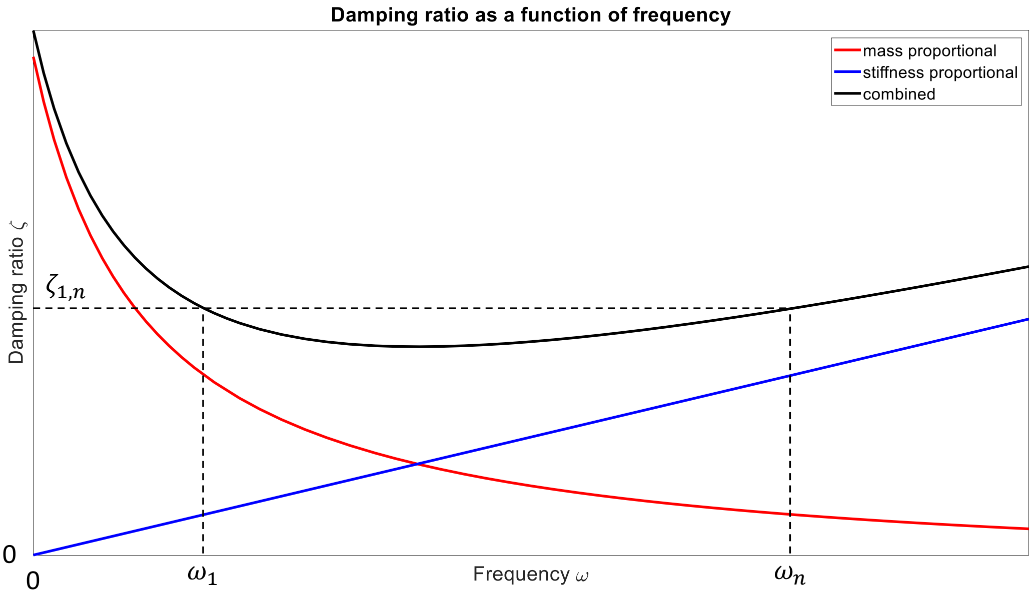

Figure 2.6: Rayleigh damping. Functions for damping ratio with mass, stiffness and combined proportionality. Note, that in this context ω_n denotes the nth eigenfrequency.

It should be stated that the damping characteristic that Rayleigh damping introduces is not physical for most systems, and is thus more commonly exploited as a way of decoupling the equations. Alternatively, modal damping can be used to force a specific damping ratio for each mode shape, if the damping ratio for all modes is equal the system will have a constant damping ratio, while still having the benefits of decoupling the equations. The concept of modal damping can easily be understood using Rayleigh damping, as it simply corresponds to defining an α_i and β_i, for each mode, such that the damping ratio is forced to a specific value.

2.4.3 Reverberation time

The reverberation or also called the decay time is a measure of how long a sound rings. In acoustics, a sound is said to have ended once its vibrational energy is reduced to one-millionth of its initial value, i.e. a 60 dB decay.

[12, p. 321] The time elapsed is the reverberation time, T, and is defined as in (2.75). [4, p. 186]

$$T = \frac{\ln 10^6}{\omega\eta} \tag{2.75}$$

According to DALI A/S, when designing a loudspeaker a lower reverberation time is better. This is because the reverberation time is measured from when the excitation is removed, meaning that the sound heard during the reverberation time is heard simultaneously with the current sound emitted by the loudspeaker.

In (2.75), η, denotes the loss factor which is a dimensionless parameter that represents the ratio of the energy dissipated in a system to the total energy stored in the system per cycle of vibration. [12, p. 229] It is possible to relate the damping ratio and the loss factor to each other through the logarithmic decrement, assuming a harmonic excitation and response. In (2.76) it is apparent that the equivalent damping ratio corresponds to a half loss factor. [8, p. 192-195]

$$\zeta_{eq} = \frac{\eta}{2} \tag{2.76}$$

2.5 Theory of optimization

In this section, the relevant theory for the optimization performed in this project is presented. Firstly the different types of optimization problems are presented. Secondly, the concept of gradient-based methods for solving optimization problems is presented in brief. Thirdly, the concept of zero-order methods is presented. Lastly, the use of surrogate models is explained.

In optimization theory, there are in general four types of optimization problems.

1. Unconstrained, single-objective
2. Unconstrained, multi-objective
3. Constrained, single-objective
4. Constrained, multi-objective

It is evident that there are two main parameters from which the optimization problem is characterized, i.e. whether it is constrained or unconstrained and whether it is a single-objective or multi-objective. An unconstrained optimization problem is a problem where the input parameters to the objective function are allowed to take any value. The solution to the optimization problem is therefore always the global minimum of the objective function. This is a very rare type of optimization problem for engineering problems, as there are typically physical limits to the values of input parameters. Constrained problems are more common. Here the input parameters are limited and are not allowed to take any value. In the case of this project, the location of the internal supports are not allowed to collide with the other components in the cabinet and are confined to the interior of the cabinet. Additionally, the supports are also limited in their total amount of volume, as the speakers still require a certain amount of air volume in the cabinet. The constraints limit the objective function to a feasible domain, and the solution to the optimization problem will be the minimum of the objective function in this domain. A single-objective optimization problem is a problem where only one function is to be minimized. The solution to these problems is one singular point in the feasible domain of the objective function. However, multiple objectives are also a common type of problem. An example of this could be to both try and minimise the ERPL of the cabinet, to reduce the power output, and to move certain eigenfrequencies up in frequency in order to reduce reverberation time. If all objective functions have the optimal point at the same location, then this point is the solution. However, often the objective is optimal at different points, i.e. the objectives are conflicting. Here a compromise solution must be found. A general formulation for an optimization problem is stated:

$$\begin{aligned} \text{minimize: } & f_i(x) \\ & x \in X \end{aligned} \tag{2.77}$$

Where f_i are the objective functions and x is a vector of n input parameters, $x = [x_1, x_2, \dots, x_n]$, and are subject to equality constrains $h(x)$ and inequality constraints, $g(x)$.

$$\begin{aligned} g(x) &\leq 0 \\ h(x) &= 0 \end{aligned} \tag{2.78}$$

From these constraints, the feasible domain, X, is defined as:

$$X = \{x \in \mathbb{R}, g(x) \leq 0, h(x) = 0\} \tag{2.79}$$

This is the standard formulation of optimization problems. It is immediately obvious that if the objective is to maximise a function, then the objective function will just be that function with a change of sign.

Pareto optimality

When dealing with multiple objective functions, it is uncommon that all objective functions obtain their minimum value at the same point in the design space. In the rare cases where this point exists the result of the optimization is this singular point which is called the utopia point. However, for most multi-objective problems the objective functions are conflicting, and the result is a set of Pareto optimal points. A Pareto optimal point is defined as a point where no objective function can be minimized any further without increasing at least one other objective function. Several designs meet this criterion, including designs at the minimum value of each individual objective function. For two objective functions, a line of Pareto optimal points between these individual minimums exists and for three conflicting objectives, a surface exists of Pareto optimal points, etc. This is called the Pareto front, which consists of an infinite amount of designs. The result of a multi-objective optimization should thus be a set of designs that represent this Pareto front. The user must after the optimization algorithm is finished choose a design from the set of Pareto optimal solutions.

2.5.1 Gradient-based methods

Gradient-based methods are often used to solve optimization problems where gradient information is available and for one objective function only. The reason for this is that gradient-based methods converge to one point in the feasible domain rather than a set of Pareto-optimal points such as the MOGA-algorithm, which is explained in Section 2.5.2. Gradient-based methods typically follow the following steps.

1. Estimate a starting design, $x^{(k)}$ for iteration $k = 0$. Select a convergence criterion η.
2. Compute the gradient of the objective function $\nabla f(x^{(k)})$.
3. Calculate $\|\nabla f(x^{(k)})\|$. Stop if $\|\nabla f(x^{(k)})\| < \eta$.
4. Calculate a search direction $d^{(k)}$. This can be done in many ways, including the steepest descent method [13, p. 443], conjugate gradient method [13, p. 446], modified Newton's method [13, p. 473], etc.
5. Calculate a step size, $\alpha^{(k)}$. This can also be done in many different ways such as the golden section search [13, p. 437], polynomial interpolation [13, p. 449], etc.
6. Update the design point $x^{(k+1)} = x^{(k)} + \alpha^{(k)} d^{(k)}$. Go to step 2.

As gradient-based methods rely on being able to compute gradients of the objective function, it is often not used when the gradient cannot be found analytically. In the case of the ERPL found in a harmonic finite element analysis, gradient information has to be approximated by a forward difference or central difference approximation. This means that the objective function has to be evaluated one extra time per design parameter in each iteration for forward difference approximations and two extra times for central difference approximations. For objective functions that are evaluated in a finite element analysis, which is often computationally expensive, gradient-based methods are not the preferred option.

2.5.2 Zero-order methods

Zero-order optimization methods are methods that do not require gradient information about the objective function, i.e. only the function value for the design point in each iteration is needed. The most commonly used types of zero-order methods are genetic algorithms. Genetic algorithms are based on the same principles as the evolution theory by Charles Darwin and can be used for both single-objective problems and for multi-objective problems as proposed in [14]. The fundamental steps in a genetic algorithm are outlined below:

1. Generate an initial population, ψ, of N_p designs within the feasible design space and define a stopping criterion. For single objective problems, the stopping criterion is a number I_g, where if for I_g consecutive generations the same design has been the fittest, then the algorithm is stopped. Alternatively, a stability percentage, S, is set, for which the algorithm is stopped when the stability criterion, explained in step 6, is reached. For multi-objective problems, a number η is set, which defines a maximum percentage of Pareto optimal designs in the population before the algorithm is stopped.
2. Evaluate the objective function and fitness of each design. The fitness function is typically defined as $F(\psi) = max(f(\psi)) - f(\psi)$, where $F(\psi)$ is the fitness for the design points in the population. If dealing with multiple objectives, then the fitness function will be as seen in (2.80).
$$F(\psi) = \sum_{i=1}^{n} w_i F_i(\psi) \tag{2.80}$$
Where $F_i(\psi)$ is the fitness function for the objective function $f_i(\psi)$, n is the number of objective functions, and w_i is a weight for each objective function. In order to allow the algorithm to search in different directions in the feasible space, then the weights are randomly chosen according to (2.81).
$$w_i = \frac{rand_i}{\sum_{j=1}^{n} rand_j} \tag{2.81}$$
Where $rand$ is a vector of n numbers randomly chosen between 0 and 1. This gives a random weight for each objective function which allows for the algorithm to converge on a Pareto front in the design space, rather than a single point.
3. Chose designs from the current design population for progressing to the next step. This selection process is done according to (2.82). $P(x)$ is the probability of the design x, in the population ψ, being selected.
$$P(x) = \frac{max(f(\psi)) - f(x)}{\sum\left(max(f(\psi)) - f(x)\right)} \qquad x \in \psi \tag{2.82}$$
In addition to this, a number of the best-performing design points are chosen as “elite” design points, and will move on directly to step 6.
4. Crossovers are performed. A selected number of design points are paired up and a crossover operation is performed.
5. A selected number of design points undergo a mutation operation, where one or more of the design parameters are changed.
6. Insert the “elite” design points back into the population. If the same design point has been the fittest for the last I_g iterations for single-objective problems, or if the amount of Pareto optimal points accounts for more than η of the total population for multi-objective problems, then the algorithm is converged and stopped. Alternatively for single objective problems with a stability-stopping criterion, the algorithm is stopped if 2.83 is true.
$$\begin{gathered}\frac{|mean_k(f(\psi)) - mean_{k-1}(f(\psi))|}{max(f(\psi)) - min(f(\psi))} \leq S \\ \text{and} \\ \frac{|stdDev_k(f(\psi)) - stdDev_{k-1}(f(\psi))|}{max(f(\psi)) - min(f(\psi))} \leq S\end{gathered} \tag{2.83}$$
Where $mean_k(f(\psi))$ and $mean_{k-1}(f(\psi))$ is the mean value of the evaluations in the current and previous iteration respectively, and $stdDev_k(f(\psi))$ and $stdDev_{k-1}(f(\psi))$ is the standard deviation of the evaluations in the current and previous iteration. Otherwise, return to step 2.

7. If the optimization is a multi-objective problem, the user must choose a design from the set of Pareto optimal designs.

As no gradient information is required for genetic algorithms, these are often used for the optimization of the output from finite element models. However, the algorithms can still require many evaluations depending on user settings such as the population size, and convergence criterion. It should also be noted that genetic algorithms do not require continuity of the objective function.

2.5.3 Surrogate model optimization

Surrogate model optimization has been shown to be an effective approach for the optimization of computationally expensive models [15]. The concept of surrogate model optimization is that an approximation of the objective function is constructed which is computationally light to evaluate, significantly reducing the time to run an optimization algorithm. The main task is now to construct a surrogate model that is representative of the unknown objective function. In order to do this, the objective function is evaluated in certain locations in the design space and is interpolated in order to construct the approximation. The task is now to choose points to evaluate that gives a good approximation of the objective function, using fewer evaluations than what is required if a zero-order optimization had been directly used instead. In [15], several schemes for choosing these points are presented, including the Latin Hypercube Sampling method (LHS), Orthogonal Arrays method (OA), Polynomial Regression method (PRG), etc. However, the method attempted in this project is the sparse grid scheme [16, p. 347-350]. Sparse grids are a method used for dealing with "the curse of dimensionality", a term coined in [17]. The curse of dimensionality refers to the number of points needed, to approximate an arbitrary function at a certain accuracy, growing exponentially with the number of input parameters, i.e. the number of dimensions. The sparse grid was first developed in [18] for numerical integration. In [19] it is shown that sparse grids require fewer points to approximate an n-dimensional function at a given accuracy when compared to traditional full-grid methods. In order to understand the sparse grid scheme, consider the simple example of a function of one input parameter, x. The design space is thus a line spanning from the minimum to maximum allowable value of the parameter, x_{min} to x_{max}. The sparse grid is built up of levels of grids in the parameter space. A level 0 sparse grid, is the midpoint of the parameter. A level 1 sparse grid is the midpoint along with the maximum and minimum values. Level 2 then adds points at the midpoint between the existing points and so forth. The approximation of the function value is thus a piece-wise linear interpolation between all evaluated points. Adding an extra parameter, and thus a new dimension, results in the 2D sparse grid seen in Figure 2.7.

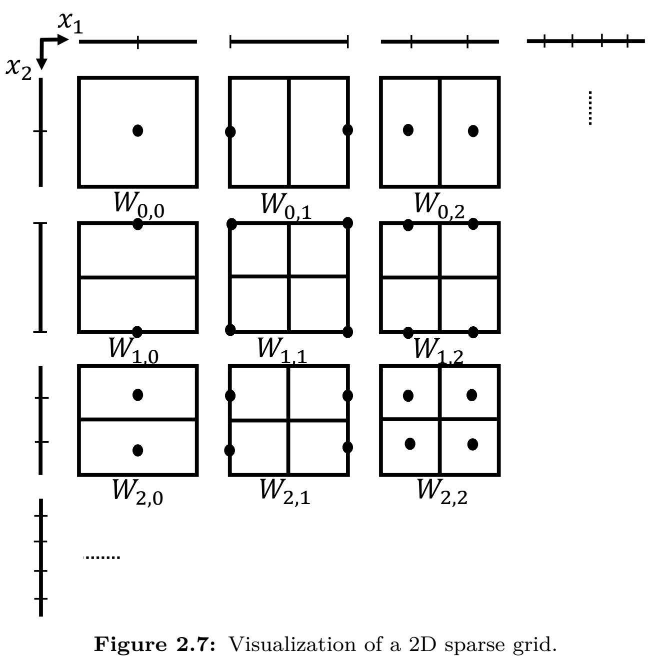

Figure 2.7: Visualization of a 2D sparse grid.

In the figure, the two axes represent the two input parameters, x_1 and x_2. W_l is introduced as the name of the sparse grid, where l is a multi-index with the same dimension as the number of input parameters. For the case of two variables, $l = [i, j]$, where i indicates the level, also sometimes referred to as depth [16], for x_1, and j indicates the level for x_2. All previous levels for a parameter must have been made before the next level is made. The first initialization step is the evaluation of the $W_{0,0}, W_{1,0}$ and $W_{0,1}$ grids. Next, the approximated model is evaluated at the points in the next grid. Lastly, the "real" model is evaluated. The accuracy of the model is defined as the difference between the real and approximated value, normalized with the difference between the maximum and minimum value of the entire approximated objective function. When the relative error for each objective function is less than a user-defined value, the process stops. The optimization can now be performed on the surrogate model, which is computationally light to compute. However, it is worth noticing that the accuracy of the surrogate model is only as good as the user-specified stop criterion allows it to be.

Problem statement 3

In this chapter, the problem that the project aims to solve is stated and clarified. This will be done by first defining the main task. The main task will then be split into four sub-tasks, which will be solved in their respective chapters. Finally, the delimitations of the project are stated.

3.1 Task definition

In Chapter 1 it was stated that DALI A/S wishes to develop a method for designing loudspeaker cabinets using simulation-driven design in order to reduce the sound emitted by their cabinets. The less sound radiated by a loudspeaker cabinet, the better the cabinet is considered. DALI A/S has requested that the procedure for designing a cabinet using simulations is developed by taking point of departure in their Rubicon 6 loudspeaker and only by moving the existing internal supports of the cabinet, thus keeping the remaining cabinet geometry constant. Additionally, DALI A/S has also requested that an alternative internal support structure is developed to exemplify the capabilities of a simulation-driven design procedure when the design is less restricted. In Chapter 2, theory relevant to the project was presented, including the equivalent radiated power level, ERPL, which will be the measure used to quantify the sound radiated from the cabinet.

Main task:

Reduce the maximum equivalent radiated power level of all exterior MDF surfaces of the cabinet by a re-design of the internal support structure.

The main task is split into four sub-tasks:

- **Sub-task 1: Develop a benchmark model**
  Develop a finite element harmonic analysis that calculates the ERPL of all exterior MDF surfaces of the cabinet as a function of the frequency.
- **Sub-task 2: Develop a design model**
  Develop a finite element harmonic analysis with reduced solution time compared to the benchmark model from sub-task 1, while giving results that are comparable to that of the benchmark model.
- **Sub-task 3: Move internal supports using optimization**
  Parameterize the position of the internal supports. Optimize the position of the internal supports with respect to minimizing the maximum ERPL.
- **Sub-task 4: Develop an alternative internal support structure**
  Develop an alternative internal support structure to exemplify the possible reduction in maximum ERPL when the design is less restricted.

3.2 Delimitations

The following delimitations are made in order to simplify the project. The implications of all delimitations are discussed in Chapter 8.

- **No experiment is performed on the final design.**
  The only experiment performed in this project is on the initial design for the validation of the benchmark model.
- **No air is included in any simulations.**
  No air is included in the simulations, and the ERPL is used as a measure of the sound radiated from the cabinet.
- **Only the woofers are considered.**
  The forcing from the dome and ribbon tweeter are ignored.
- **Only the maximum ERPL is considered as the objective.**
  Other metrics such as the reverb time, the location of the eigenfrequencies, etc. are not considered.
- **Only one loudspeaker is analyzed.**
  Only the Rubicon 6 loudspeaker is analyzed.
- **No non-linear vibration analyses are performed**
  Only linear vibration analyses are performed.

Development of benchmark model 4

Sub task 1: Develop a benchmark model

Develop a finite element harmonic analysis that calculates the ERPL of all exterior MDF surfaces of the cabinet as a function of the frequency.

In this chapter, a benchmark model for analysing the frequency response of the cabinet is developed. The benchmark model is developed with a focus on accuracy, meaning that computational efficiency is not emphasized.

A preliminary benchmark model is developed to assist in the design of the experiment which the benchmark model is validated against. The setup of the experiment is described and the results are presented and compared against the preliminary benchmark model. The preliminary benchmark is changed based on the results of the comparison and a final benchmark model is presented and validated by comparison with the experimental results.

The benchmark model is developed in ANSYS Workbench 2023 R1 and consists of a linear modal analysis which passes mode shapes and eigenfrequencies to a mode superposition harmonic analysis. The result of a harmonic analysis is the response, resulting from a harmonically applied load, of the field variable as a function of the frequency of the applied load. Lastly, the ERPL of all exterior MDF surfaces of the cabinet is calculated as a function of the frequency.

4.1 Preliminary benchmark model

In this section, the preliminary benchmark model, used for designing the experiment that is used to develop and validate the final benchmark model, is developed.

4.1.1 Defeaturing

Despite the benchmark model emphasising accuracy, as opposed to computational efficiency, simplifications to the analysed geometry are still necessary. Figures 4.1 and 4.2 show the original and defeatured loudspeaker, respectively. Minimal simplifications are made to the cabinet as this is the least complex component of the loudspeaker. The dome tweeter and ribbon tweeter are replaced with a solid plate of aluminium as both are disregarded, cf. Section 3.2 regarding the delimitations. The aluminium plate ensures that the stiffness in this section of the cabinet is retained. A loss in mass is expected but is assumed to be of less importance, as the cabinet and the woofers account for the majority of the mass of the loudspeaker. The woofers are simplified by eliminating the surround, diaphragm, dust cap, voice coil and spider, as these components are assumed to have an insignificant influence on the mass and stiffness. All remaining components of the woofers are simplified to a single body made of structural steel. The speaker terminals are simplified to a solid ABS plate to retain the stiffness. The bass reflex ports are simplified by removing features such that they have a more uniform thickness to avoid using unnecessary small elements. This is assumed to have no discernible influence on the stiffness and mass.

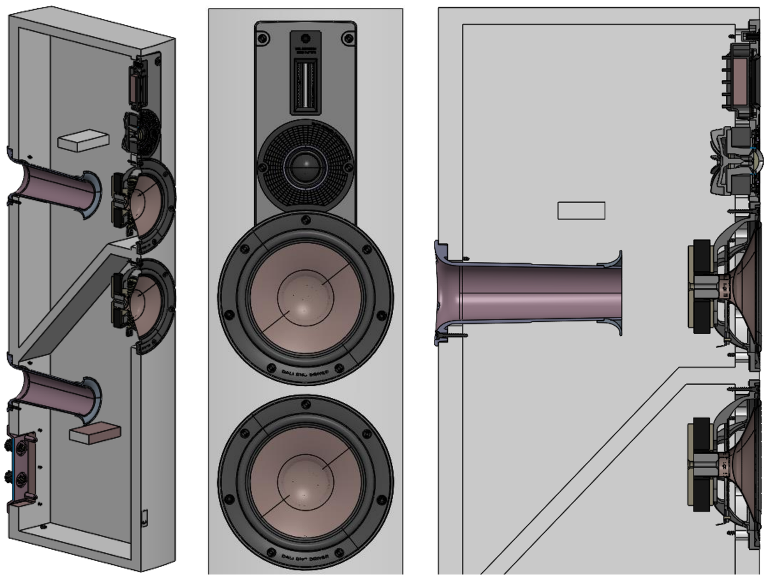

Figure 4.1: Original cabinet before any features are removed.

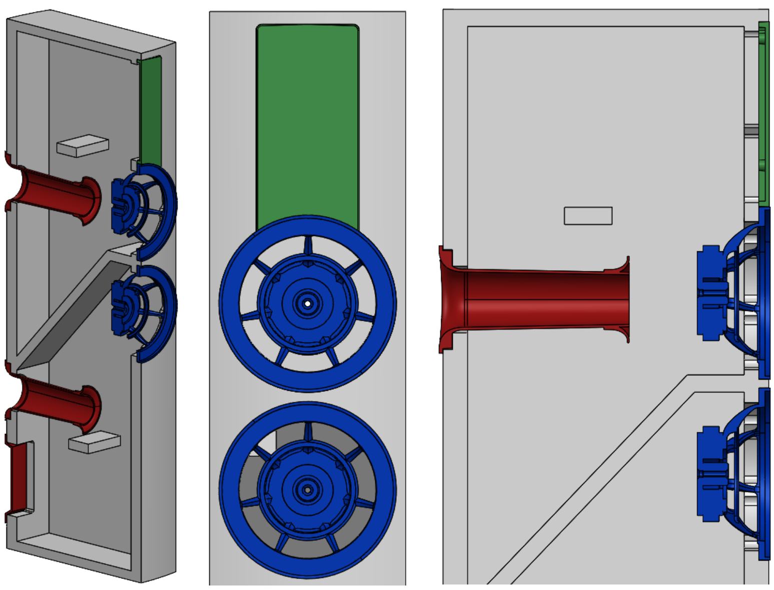

Figure 4.2: Defeatured cabinet to be used in the benchmark model. Colours refer to material assignments cf. Table 4.2.

4.1.2 Meshing and convergence

As the goal of the benchmark analysis is to model the harmonic response of the cabinet, the stiffness of the baskets, tweeters, speaker terminals and bass reflex ports, are of less importance compared to the stiffness of the cabinet. The mesh refinement of these components is therefore minimal as mass convergence is achieved even using a coarse mesh. A mesh convergence study for the modal analysis is conducted, analysing the 30 lowest eigenfrequencies, corresponding to the range from 0 Hz to ≈1000 Hz. The percentage change between each eigenfrequency for each interaction is found and the maximum change for any mode in each iteration is reported. The median change for all modes for each iteration is also reported. Note, that modes pertaining only to the bass reflex ports, tweeters and speaker terminals are excluded in this convergence study, as these are of no interest. All bodies are meshed using SOLID187 quadratic tetrahedral elements with the maximum allowed element size being halved for each iteration. The results are seen in Table 4.1.

Table 4.1: Convergence study of benchmark modal analysis. The change indicates the maximum and median relative deviation from the previous iteration for any mode.

Max element size [mm]	DoF	Max change [%]	Median change [%]
100	228696	N/A	N/A
50	223680	7,8	4,0
25	280860	12,6	7,9
12,5	494265	5,8	2,5
6,25	1157484	4,2	1,3
3,125	3843978	2,3	0,6

A maximum element size of 12.5 mm is chosen for the benchmark model, as all subsequent iterations reported median changes smaller than 2.5%, which is deemed acceptable. Figure 4.3 shows the mesh of the benchmark model.

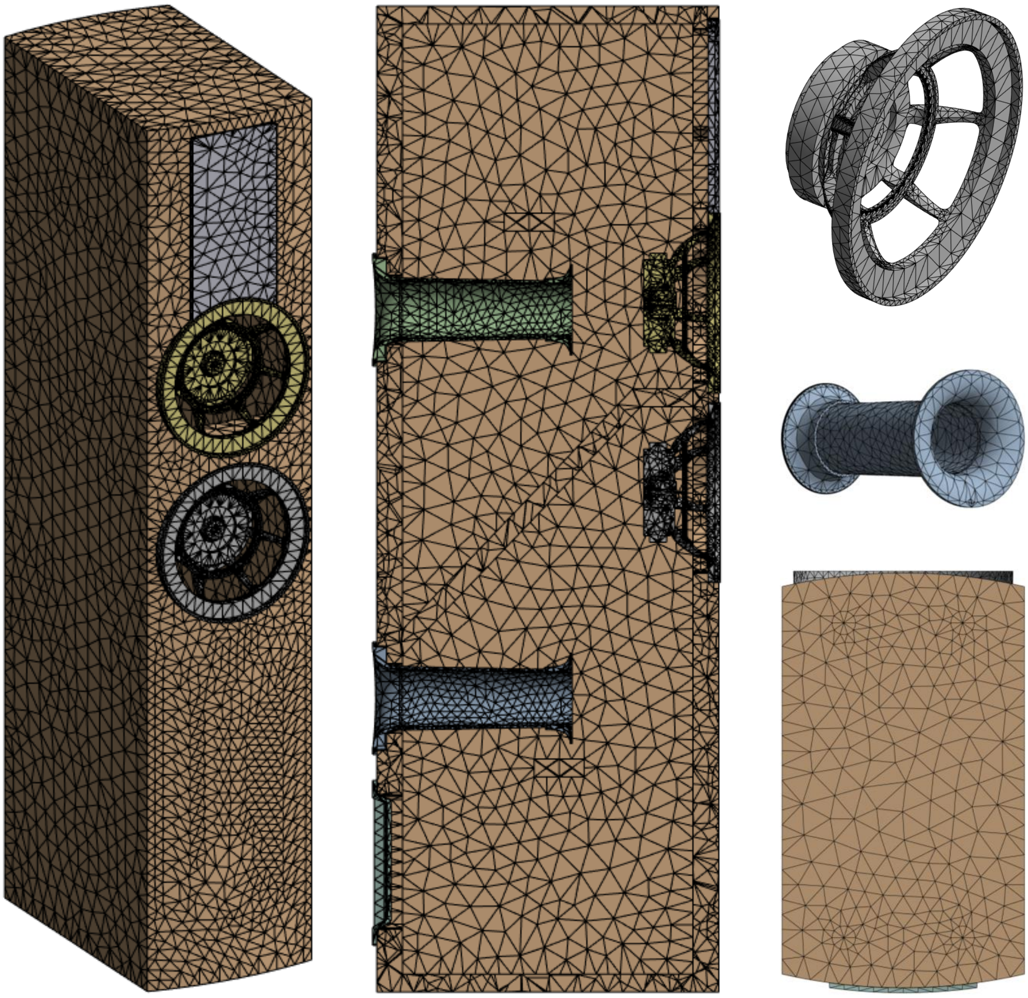

Figure 4.3: Mesh of the benchmark model. Maximum allowed element size: 12.5 mm.

4.1.3 Material definition

Table 4.2 lists the material properties used in the benchmark model. The colours refer to Figure 4.2. The damping ratio is derived from the loss factor, assuming that the damping ratio is equal to half of the loss factor. The relationship between the damping ratio and loss factor is explained in Section 2.4.3. Loss factors are cited from [4, p. 191,196] while the densities, stiffnesses and Poisson ratios are taken from ANSYS's material library.

Table 4.2: Material properties. Damping ratio derived from loss factor [4, p. 191,196]. Colours refer to Figure 4.2.

Material	Colour	ρ [kg/m^3]	E [GPa]	ν	ζ	η
Steel	Blue	7850	200	0,3	2.0×10^{-4}	4.0×10^{-4}
Aluminum	Green	2770	71	0,33	2.5×10^{-5}	5.0×10^{-5}
MDF	Gray	735	3,8	0,25	1.0×10^{-2}	2.0×10^{-2}
ABS	Red	1050	2,5	0,41	1.5×10^{-2}	3.0×10^{-2}

4.1.4 Boundary conditions

The loudspeaker is standing on feet which are mounted using holes on the bottom. A type of feet often used for loudspeakers is called speaker spikes. There are two different types of speaker spikes; one type aims to couple the loudspeaker to the floor and another type aims to decouple the loudspeaker from the floor. The Rubicon 6 loudspeaker uses the first kind which couples the loudspeaker to the floor. Their property of digging themselves into the floor is illustrated in Figure 4.4. This, of course, requires a floor with low hardness e.g. wood, linoleum, carpet, etc. and would not work on say a concrete floor. By digging into the floor the spikes aim to prevent the loudspeaker from losing contact with the floor, as any displacement of the loudspeaker that is not orthogonal to the floor would generate a reaction force between the floor and the spike resulting from friction due to the conical shape of the spike.

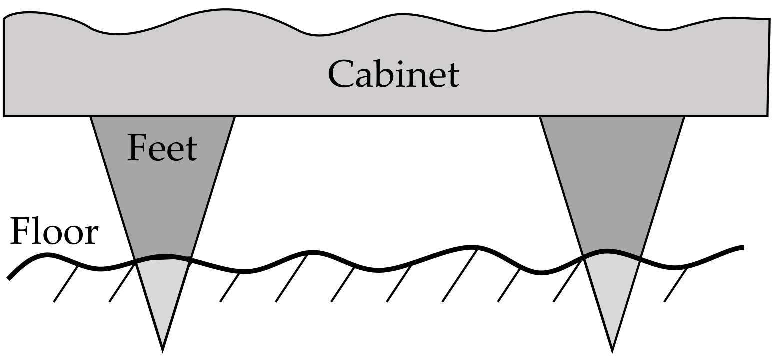

Figure 4.4: Feet of the loudspeaker. Here illustrated their property of digging into the floor.

The boundary conditions applied to the mounting hole of the spikes aim to model their behaviour of digging in. Figure 4.5 shows the boundary conditions applied to the bottom face of the loudspeaker. All DoFs of all nodes are locked, i.e. no displacement or rotation of the elements in the holes is allowed. These boundary conditions are expected to yield results where the connection between the loudspeaker and the floor is too stiff, as the loudspeaker is essentially bolted to the floor in the model. A bolted connection is hypothesized to be an over-prediction of the ability of the spikes to couple the loudspeaker to the floor.

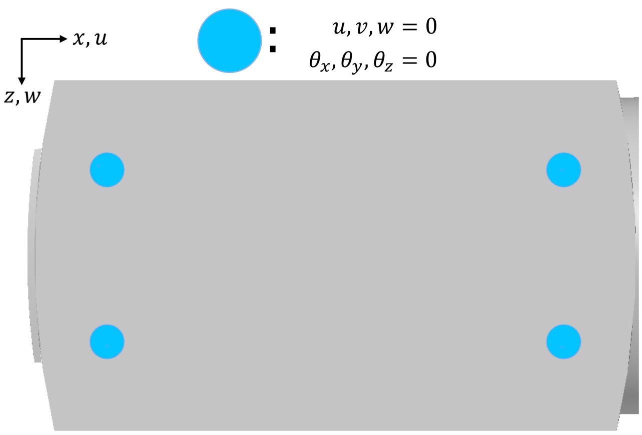

Figure 4.5: Boundary conditions of benchmark model applied to the holes in the bottom face.

4.1.5 Forcing

The loudspeaker has crossovers for the upper and lower woofers set at 800 Hz and 2600 Hz respectively. Two loads F_u and F_l are applied to the outer rim of the upper and lower basket respectively, as all other driver components are excluded from the analysis. The loads are applied normal to the driver, i.e. in the x-direction, with unit magnitude. In order to model the crossovers the loads are applied in two frequency ranges according to Table 4.3, such that the lower basket is not loaded at frequencies above 800 Hz. The applied loads are seen in Figure 4.6.

Table 4.3: Magnitude of forces F_u and F_l in the two frequency ranges defined by the crossovers.

Frequency range [Hz]	0-800	800-2600
F_u [N]	1	1
F_l [N]	1	0

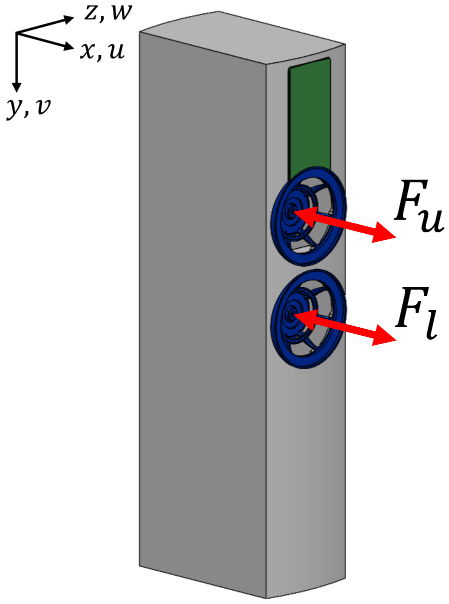

Figure 4.6: Harmonically varying loads F_u and F_l applied to the upper and lower basket.

F_u and F_l are applied as unit loads, as the response of the preliminary benchmark is only used as a tool for designing the experiment that the benchmark is validated against. As such, a response with arbitrary scaling is sufficient to determine which measurement points are interesting to measure in the experiment.

It should be noted that the effect of the internal air is disregarded in this model. However, the effect thereof is investigated after the experiment, as the displacement of the diaphragms as a function of the frequency is then known. In turn, the change in internal volume in the cabinet is also known, which can then be used to estimate the change in internal pressure.

4.1.6 Results of preliminary benchmark

The goal of the benchmark analysis is to model the sound radiated by the cabinet. As described in Section 2.1.3, ERPL is a simplified method for the calculation of the radiated acoustic power from a mode superposition harmonic analysis. The result of interest from the benchmark, in the context of decreasing the sound radiated by the cabinet, is thus the ERPL from all exterior MDF surfaces of the cabinet. The experiment for validating the benchmark should therefore prioritize accuracy at frequencies where the ERPL predicts that the cabinet radiates the most sound. A plot of the ERPL as a function of the frequency for all exterior surfaces of the cabinet is seen in Figure 4.7.

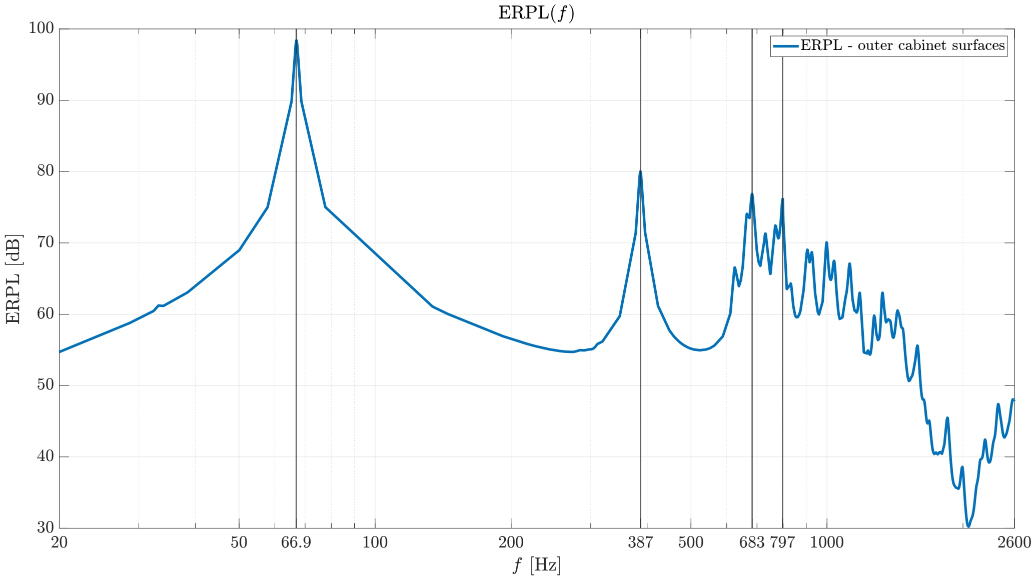

Figure 4.7: ERPL-frequency plot of all exterior MDF surfaces of the cabinet from the preliminary benchmark model.

In Figure 4.7 four points of interest are shown on the graph indicated by a black vertical line. These points are chosen as they are peaks that have the highest value of ERPL. The frequency of these peaks is shown on the frequency axis of the plot. The experiment should be designed such that benchmark can be validated at these four frequencies of interest.

In Figure 4.8 the mode shapes whose associated eigenfrequencies are closest to the frequencies of the four points of interest are shown. Here it is evident that the eigenfrequencies and the frequencies of the points of interest are coincident. It is therefore assumed that the mode shapes shown are dominant in the deformation response at these points of interest.

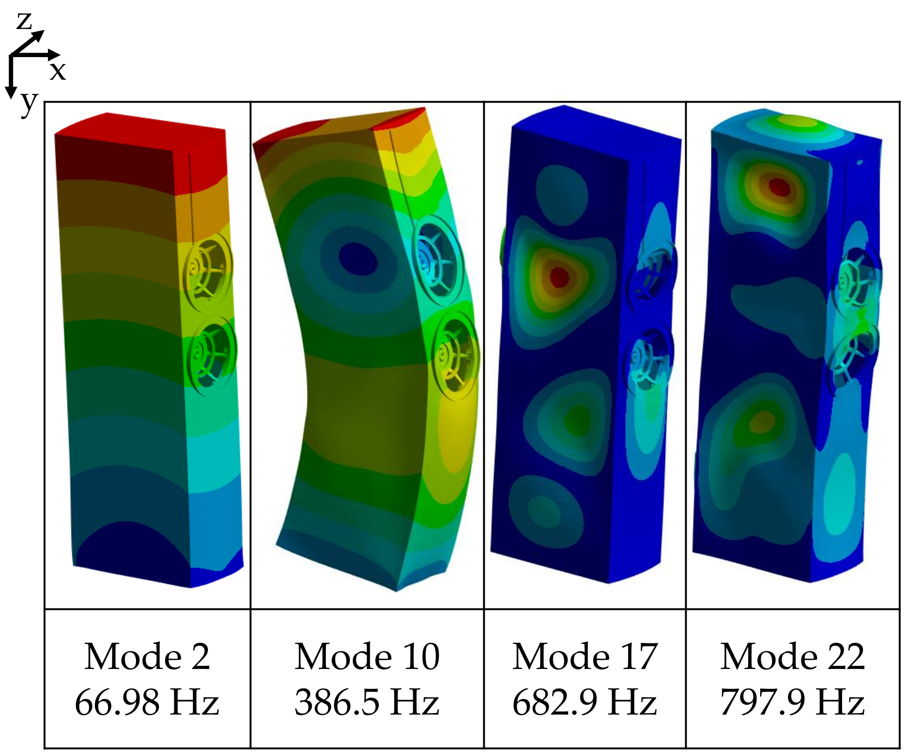

Figure 4.8: Mode shapes and eigenfrequencies closest to the frequencies of large ERPL.

Looking at the modeshapes in Figure 4.8, mode 2 is the first bending mode around the z-axis, mode 10 is the second bending mode around the z-axis, while modes 17 and 22 are both membrane modes of the cabinet walls. Intuitively, it makes sense that these particular modes result in peaks in the ERPL plot, as modes 2 and 10 are both modes with large deformation in the same direction as the force is applied, while mode 17 and mode 22 both have a large area of deformation normal to the surface of the cabinet, which, when exited will result in a large ERPL. In addition to this, it is seen that modes 2 and 10 exhibit large deformations normal to the surface on the back of the cabinet towards the top. Modes 17 and 22, exhibit large deformations normal to the surface on the side of the cabinet towards the top.

4.2 Design of experiment

In this section, the results of the preliminary benchmark model are used to design an experiment used for developing and validating the final benchmark model.

4.2.1 Test setup

Figure 4.9 illustrates the test setup for the experiment. The accelerometer used in this test is a Brül & Kjær Accelerometer Type 4374, which measures acceleration in the normal direction to the surface it is mounted on. The signal from the accelerometer is amplified using the Brül & Kjær Charge Amplifier - Type 2635. The loudspeaker is a DALI Rubicon 6, driven by an Audio Precision APx515 B audio analyzer into a NAD C 275BEE amplifier. The input signal is generated in the software APx500. The latest calibration data for the accelerometer are seen in Appendix B.

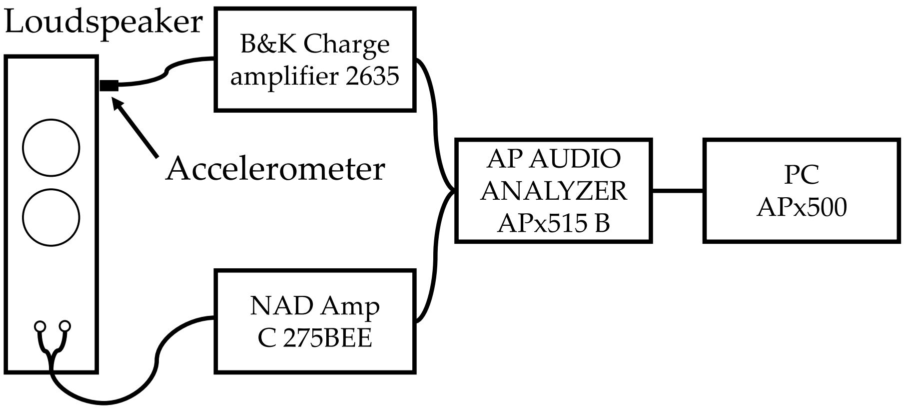

Figure 4.9: Illustration of test setup for accelerometer measurements.

The APx500 software is configured such that a frequency sweep from 20 Hz to 2600 Hz is performed over a span of 5 s with a voltage of 250 mV, amplified to 7.8 V, to power the Rubicon 6 loudspeaker. The signal from the accelerometer is Fourier transformed using the built-in FFT feature in APx500, resulting in measurements of the voltage as a function of the frequency.

The output is root mean squared voltage and is converted to peak voltage by multiplying by $\sqrt{2}$. The voltage is then converted to acceleration using the voltage sensitivity factor of $1.64\,\mathrm{mV/ms^{-2}}$ of the accelerometer as the charge amplifier is set to 10. Finally, assuming a harmonic response, the displacement is found by dividing the acceleration by ω^2, disregarding the change in sign as the time dependency is omitted. This allows for a comparison between amplitudes from the experiment and the results obtained in the harmonic analysis at discrete points.

All the measurements presented throughout the project are the mean of three consecutive measurements.

4.2.2 Placement of measurement points

The ideal placement of the measuring points requires some insight into the deformation of the loudspeaker. Recalling the results of the preliminary benchmark analysis, presented in Section 4.1.6, showed that the modes located at the frequencies of interest all exhibit large displacements in the upper section of the speaker. Additionally, the two bending modes around the z-axis displace in the x-direction, while the two membrane modes displace in the y-direction. A 3x3 grid of measurement points on the back, B_{ij}, and left side, L_{ij}, of the cabinet towards the top, is therefore chosen. In addition, a singular point on the right side, R_{22}, opposite the L_{22} point on the left side, is chosen. This is done in order to assess if any asymmetries are present in the response. The location of the points is seen in Figure 4.10 in red. The coordinates of the points are seen in Table 4.4, w.r.t. the origin at the blue point.

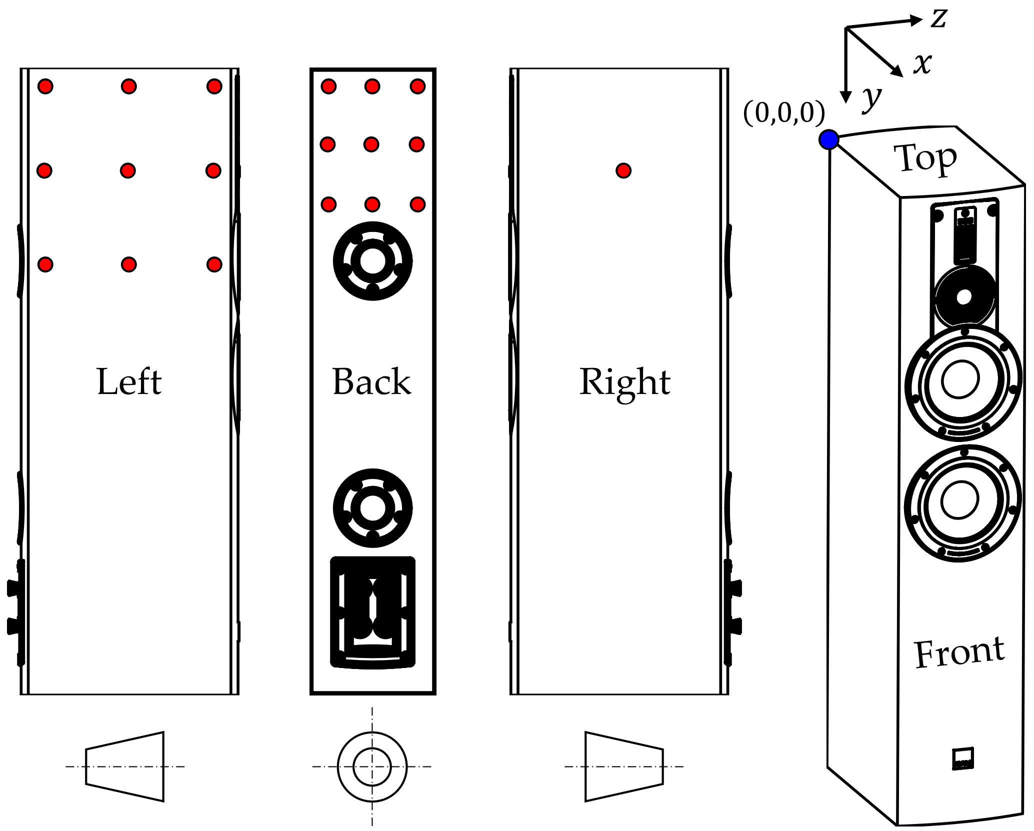

Figure 4.10: Placement of the measurement points. The blue point designates the origin of the coordinate system, while the red points are the positions of the measurement points.

Table 4.4: Coordinates of measurement points. i and j denote rows and columns, respectively, where $i = j = 1$ is at the top left when normal to a specific face, cf. Figure 4.10. All coordinates are in mm.

Left face - L_{ij} - (x y)			Back face - B_{ij} (z y)			Right face - R_{ij} (x y)
(50 50)	(160 50)	(270 50)	(150 50)	(100 50)	(50 50)	
(50 200)	(160 200)	(270 200)	(150 130)	(100 130)	(50 130)	(160 200)
(50 350)	(160 350)	(270 350)	(150 210)	(100 210)	(50 210)	

In addition to the measurement points of the cabinet, the response of the lower and upper woofer is also of interest, as this can be used to determine the force as a function of frequency. In Figure 4.11, the placement of the accelerometer on the woofers is seen.

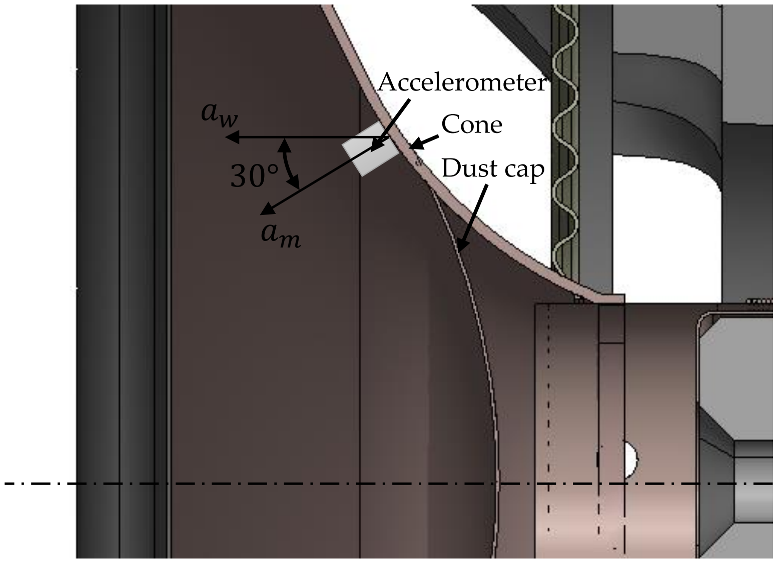

Figure 4.11: Placement of the accelerometer on the woofers, shown on a cross-section of the driver assembly.

In Figure 4.11, it is seen that the accelerometer is placed at an angle on the cone, rather than in the centre of the dust cap. The reason for this is that the eigenfrequencies of the dust cap would influence the measurements, resulting in a response that does not match that of the woofer. The component of acceleration parallel to the direction of the excitation force is found using (4.1). Here a_m is the measured acceleration and a_w is the acceleration in the direction of the woofer.

$$a_w = a_m cos^{-1}(30°) \tag{4.1}$$

4.2.3 Results of experiment

In this section, the results of the experiment are presented. First, the noise of measurements and differences between the right and left sides are presented to evaluate the overall tolerances of the experiment. Second, the responses of the woofers are presented. Third, a comparison between displacements predicted by the preliminary benchmark model and displacements measured at the discrete point B_{22} are presented.

Figure 4.12 plots the w-displacements of the left and right sides as a function of the frequency at the points L_{22} and R_{22} along with the noise floor. The benchmark model is symmetric w.r.t. w-displacements predicted at the points L_{22} and R_{22}. Any difference in the measured w-displacements between the two points can therefore not be explained by the model and must be attributed to various factors such as e.g. the manufacturing tolerance and the discrepancies between the boundary conditions and the contact between the spikes and the floor. The noise floor is found by measuring with the amplifier to the loudspeaker turned off.

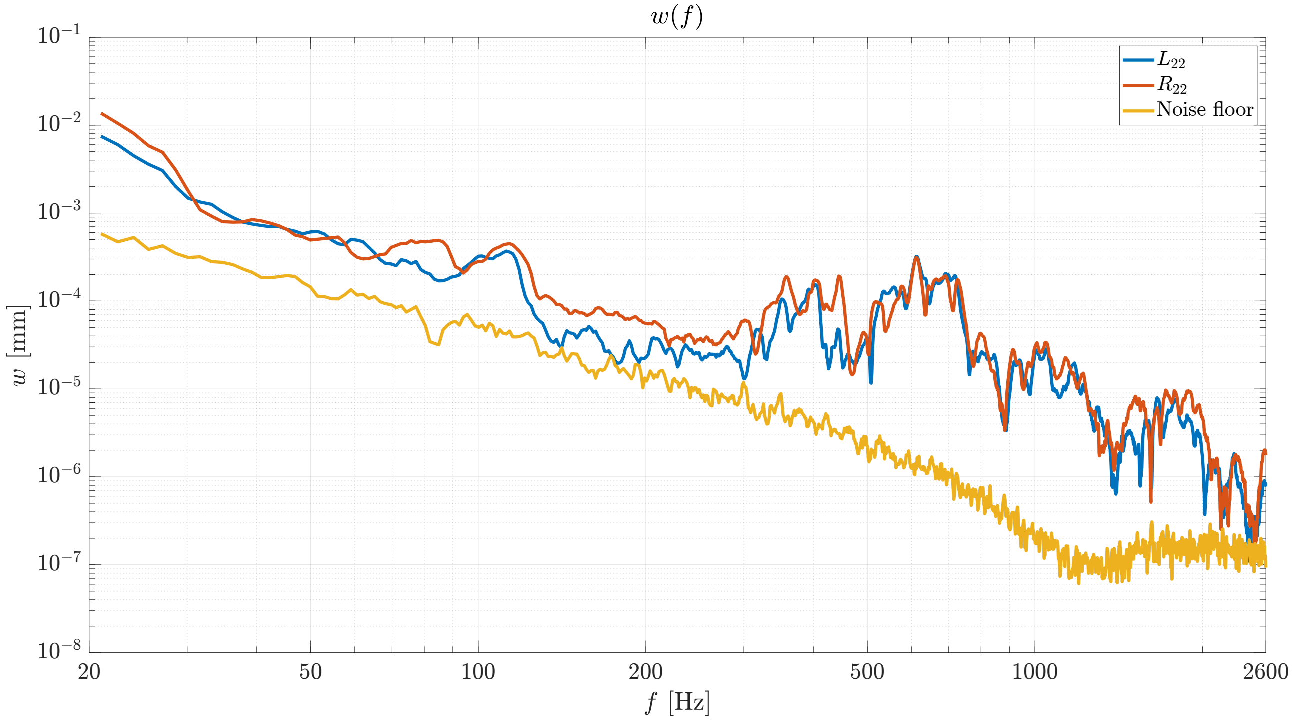

Figure 4.12: $w(f)$ measured at the points L_{22} and R_{22} and the noise floor.

In order to discuss the difference between the measured w-displacements at L_{22} and R_{22} the noise floor must be taken into account. Figure 4.13 plots the absolute difference between the w-displacements at the points L_{22} and R_{22} and the noise floor. It is evident that from ≈ 25 Hz to ≈ 65 Hz the difference between the left and right side is not discernible from the noise, i.e. it is not possible to say that there is in fact a difference in this frequency range, as it simply could be due to the noise. However, from ≈ 65 Hz and up, the difference between the sides must be considered as an actual measurable difference as the noise floor is lower and thus does not explain why there is a difference.

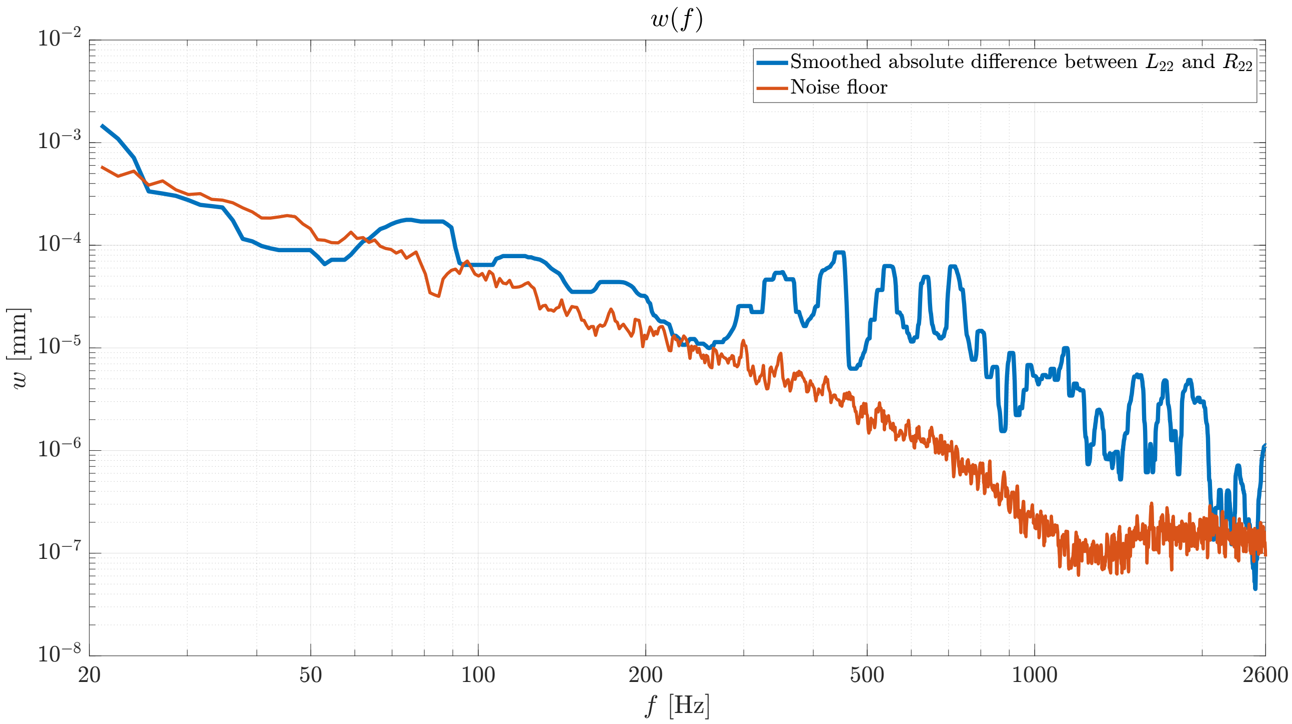

Figure 4.13: Absolute difference between $w(f)$ measured at the points L_{22} and R_{22} and the noise floor.

The total tolerance of the experiment is defined as the sum of the noise floor and the difference between the left and right sides. This total tolerance is used when the finalized benchmark is validated, as any discrepancy between the predicted and measured displacement that is smaller than this total tolerance does not equal a more accurate model. The benchmark model, therefore cannot be improved beyond this tolerance limit, as any prediction by the benchmark closer than this limit, could simply be because of variables in the physical environment that are unaccounted for in the model. Figure 4.14 plots the total tolerance as a function of frequency. The measured difference in w-displacements between points L_{22} and R_{22} are assumed to be representable of the unaccountable differences of all other points in all other displacement directions. The noise floor is of course invariant of the direction.

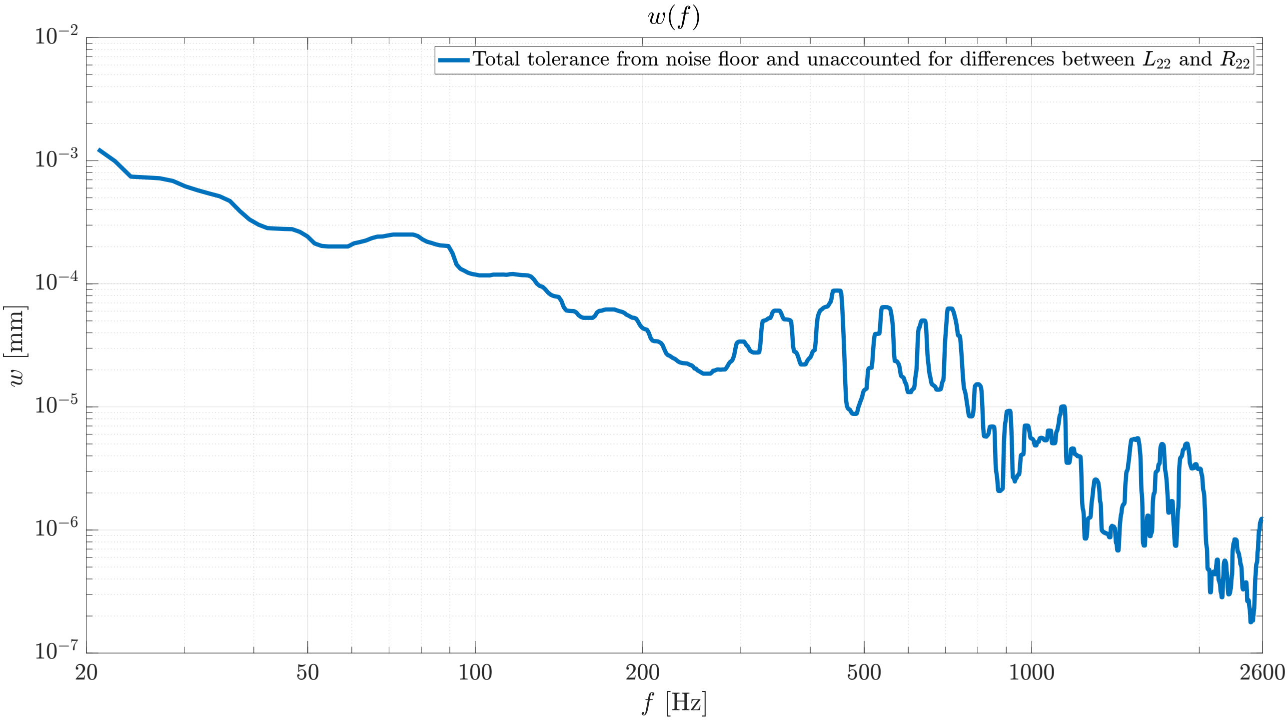

Figure 4.14: The total tolerance of the experiment as a function of the frequency, defined as the sum of the difference between $w(f)$ measured at the points L_{22} and R_{22} and the noise floor.

The forces applied to the upper and lower baskets in the preliminary benchmark are two harmonically varying unit loads constant as a function of the frequency. The crossover filter is accounted for by removing the force on the lower basket from 800 Hz and onwards. However, looking at Figure 4.15, which plots the force of the upper and lower woofer as a function of the frequency, it is immediately obvious that both the forces are not constant w.r.t. the frequency and that the lower woofer still experiences a significant force above 800 Hz. Furthermore, a dip in the forces is seen at 37 Hz corresponding to the port frequency. The port frequency is typically placed just before the lower part of the frequency range of the woofer, such that the overall frequency range of the loudspeaker is extended to a lower frequency. At this frequency, the bass reflex port and the internal air of the cabinet act as a Helmholtz resonator, such that the internal air is moving in anti-phase with the diaphragm. Therefore, measuring the acceleration of the diaphragm shows a dip at this frequency, however, the sound level at this frequency is increased as it radiates from the bass reflex port instead of from the diaphragm.

It should be noted that the forces plotted in the figure are derived using Newton's second law, assuming that each driver has a movable mass of 14.5 g, according to DALI A/S, and disregarding the influence of the air. The influence of the air on the forcing of the woofers is investigated in Section 4.3.3.

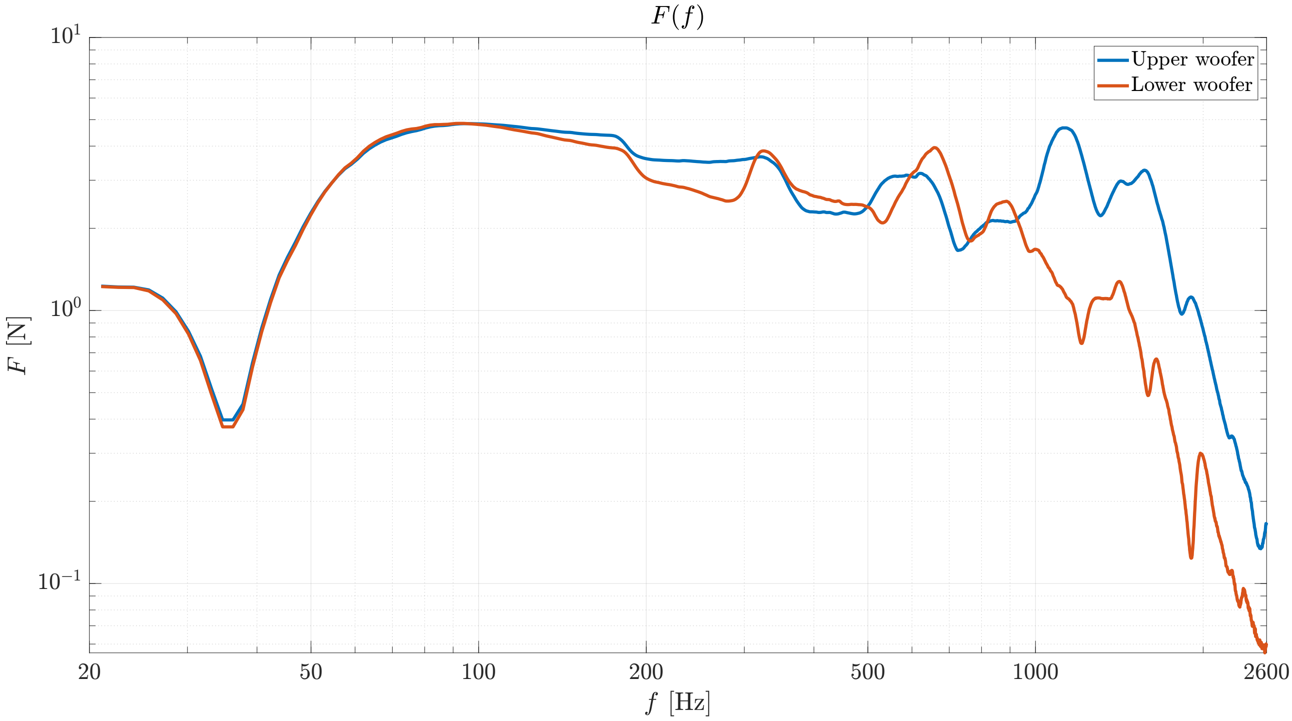

Figure 4.15: $F(f)$ for the upper and lower woofer. Derived using Newton's second law, disregarding the influence of air.

Lastly, the predicted and measured displacements are compared. Figure 4.16 plots the u-displacement at the point B_{22} along with vertical lines indicating the frequencies of interest previously found from the peaks in the ERPL plot in Figure 4.7. Comparing the magnitude between the predicted and measured displacements are of little interest, as the previous Figure 4.15 showed that the actual forcing is poorly modelled using a unit load. The variation of the measurement is captured in an overall sense by the benchmark model, as there are some similarities between the two plotted responses. Looking at the port frequency at 37 Hz the dip is not captured by the benchmark, this is expected as the unit load does not account for this and the air is disregarded. At 66.9 Hz it is seen that the mode predicted by the benchmark model is not present in the measured response. This indicates an error in the boundary conditions, as changing the stiffness of the benchmark model will only shift the response along the frequency axis and not remove a mode. Furthermore, this is not due to a discrepancy in the forcing, as the measured forcing does not spike at this frequency. In addition, generally comparing Figure 4.15 against Figure 4.16, i.e. the forcing against the measured response at B_{22}, it is seen that from 20 Hz to 100 Hz the variation of the displacement w.r.t. the frequency is explained by the variation of the forcing. Looking at the second point of interest at 387 Hz, the predicted peak is at a lower frequency than the measured peak, indicating that the benchmark model is too compliant. However, looking at the third point of interest at 638 Hz, the predicted peak is now at a higher frequency than the measured peak, indicating that the benchmark model is too stiff. The conclusion of the comparison between the preliminary benchmark model and the measured u-displacements at point B_{22}, is that the boundary conditions are erroneous, as the eigenfrequency predicted by the benchmark model at 66.9 Hz does not exist.

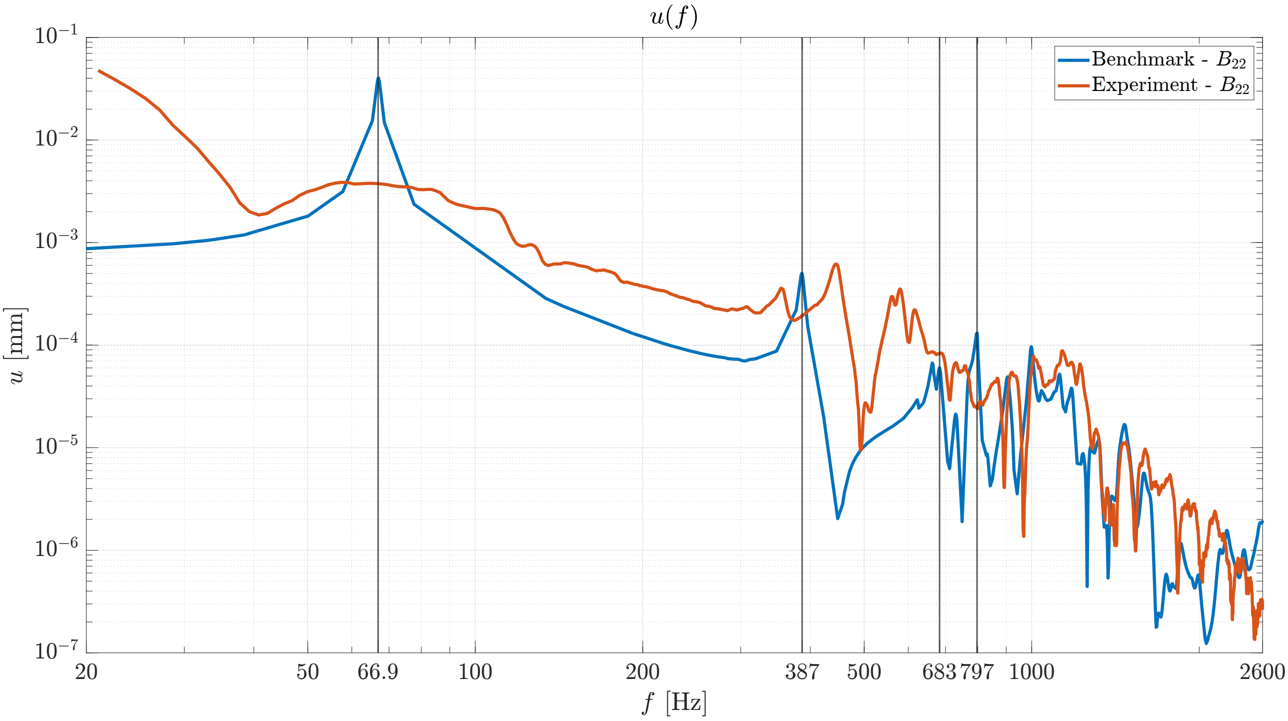

Figure 4.16: u-displacements at point B_{22} from preliminary benchmark and experiment.

4.3 Finalized benchmark model

In this section, the preliminary benchmark model is adjusted taking point of departure in the experimental results and the comparison between the preliminary benchmark and the experiment. Lastly, the response of the final benchmark is validated against the experimental response.

4.3.1 Material definition

The geometry remains unchanged, however, an adjustment is made to the stiffness of the MDF material. The stiffness of the MDF is decreased from 3.8 GPa in the preliminary benchmark to 2.55 GPa in the finalized benchmark.

4.3.2 Boundary conditions

The experiment concluded, based on the comparison between the benchmark model and the measured u-displacements at the B_{22} point, that the predicted eigenfrequency at 66.9 Hz does not exist. Recalling Figure 4.8 shows that the mode of interest is the first bending mode around the z-axis. Looking back at Figure 4.16 it is apparent that there are no modes in the vicinity of 66.9 Hz, meaning that the mode needs to be removed and moving the mode up or down in the frequency range is not a solution.

The mode is removed by imposing the boundary conditions seen in Figure 4.17 on the bottom face of the loudspeaker. The boundary conditions are softened by allowing the bottom face of the cabinet to translate along and rotate around the x and z-axes. The rotation around the y-axis remains locked, while the average translation along the y-axis for all nodes on the bottom face is 0. This allows the loudspeaker to freely rock back and forth and from side to side. This behaviour is in line with the contact facilitated by the speaker spikes, as it is fairly easy to rock the loudspeaker by applying force on the top section. The rocking is allowed as the v-displacement is 0 in an average sense if the bottom face is rotated around the x and z-axes. The loudspeaker is still inhibited from twisting around its longitudinal axis, a behaviour which was observed to be true, as the speaker spikes digging into the floor prevent this rotation.

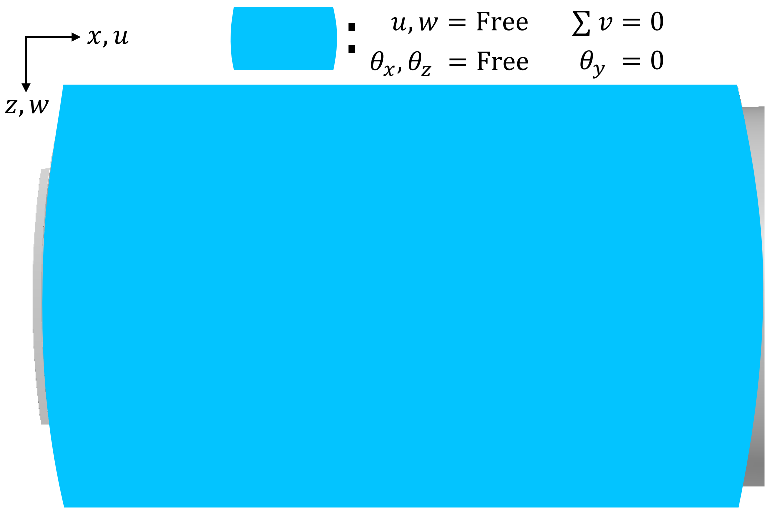

Figure 4.17: Boundary conditions of the final benchmark model applied to the entire bottom face.

4.3.3 Forcing

As stated in Figure 4.15, the forcing on the upper and lower woofer was derived assuming that the only force on the woofers was resulting from the acceleration of the moving mass of each driver. In this section, the effect of including the internal air on the forcing is investigated.

As the actual pressure as a function of the frequency inside the cabinet was not measured in the experiment, the pressure is derived based on the acceleration of the driver diaphragms. Assuming that the cabinet is closed, any change in internal volume due to the displacement of the diaphragms, results in a change in pressure. Ignoring dynamic effects and thus assuming that the problem is quasi-static the change in pressure is readily available from (4.2), where p_1 and V_1 is the initial pressure and volume when the diaphragm is in its neutral position and p_2 and V_2 is the pressure and volume when the diaphragm is fully displaced into the cabinet.

$$p_2 = \frac{p_1 V_1}{V_2} \tag{4.2}$$

The initial pressure is equal to the atmospheric pressure, $p_1 = 1\,\text{Atm}$, and the initial volume is equal to $\approx 22\,\text{l}$ for each cavity. The change in volume is calculated by multiplying the surface area of the diaphragm by the displacement of the diaphragm measured in the experiment and subtracting this from the initial volume. Figures 4.18 and 4.19 plot the change in pressure in the upper and lower cavities as a function of the frequency.

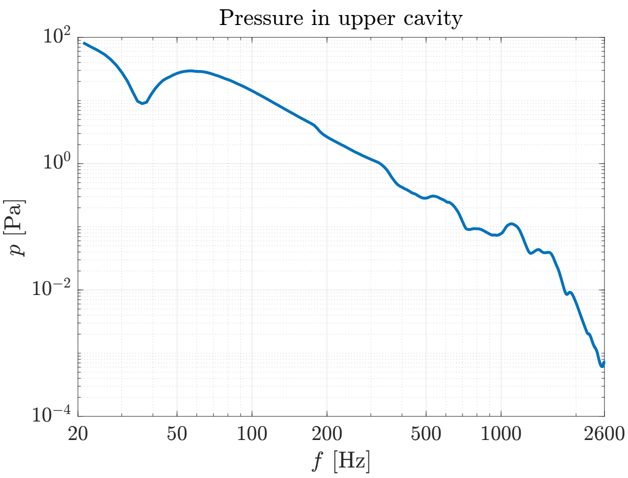

Figure 4.18: Pressure in the upper cavity of the cabinet.

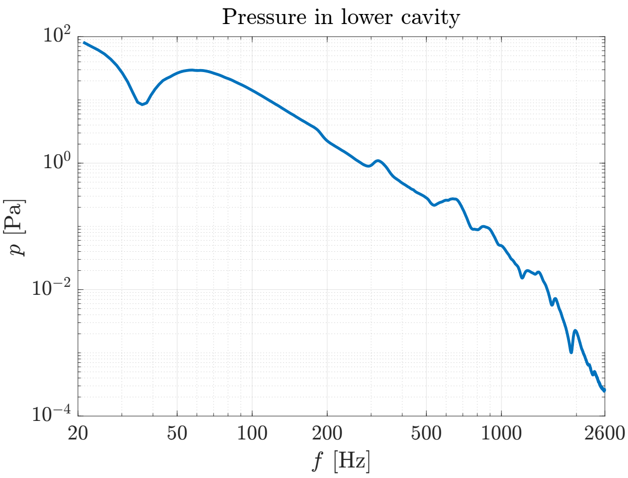

Figure 4.19: Pressure in the lower cavity of the cabinet.

In addition to adding the above pressures to all internal surfaces of the cabinet in the benchmark model, the pressure also acts on the back side of the diaphragm. As the experiment measures the acceleration and thereby also the displacement of the diaphragms while pressure is built inside the cabinet, the forcing on the woofers should account for this as well. The additional force required to build pressure in the cabinet is found by multiplying the pressure with the surface area of the diaphragm. In Figures 4.20 and 4.21, the force required to build the pressure is added to the original force, i.e. the force required to accelerate the moving mass of each driver, and plotted against the original force for both the upper and lower woofer. From the figures, it is apparent that the additional force is only significant up to 200 Hz.

The assumption of a closed cabinet over-predicts both the pressure in the cavities and thus also the additional force required to build this pressure. This is because the cabinet is of course ported, meaning that the air escapes through the bass reflex ports.

Figure 4.20: Total force applied on the basket on the upper woofer.

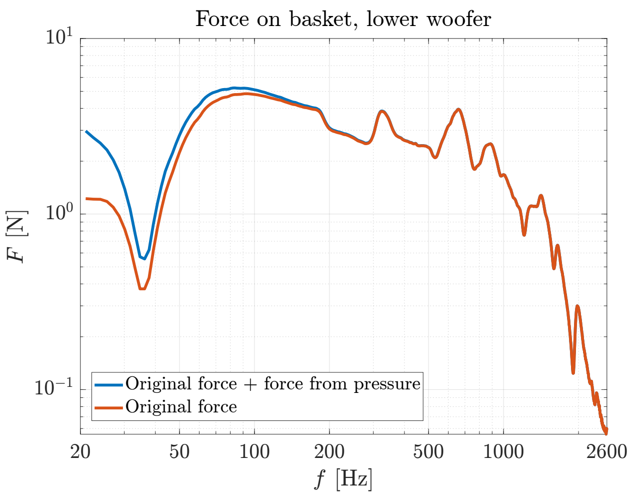

Figure 4.21: Total force applied on the basket on the lower woofer.

As the pressure and the additional force are found using the crude assumption of a closed cabinet, the influence of the pressure and additional force on the ERPL of all exterior surfaces is investigated. Figure 4.22 plots the ERPL with and without the inclusion of the pressure. The same conclusion drawn in the previous figures regarding the forcing is drawn again, as the influence on the ERPL is only significant up to 200 Hz. The influence of the pressures on the ERPL is not necessarily given by the influence of the pressure on the forcing, as the ERPL accounts for the additional excitation normal to all internal surfaces resulting from the pressure. The pressures are added in phase with the forces on the baskets, such that the pressures are maximum when the diaphragms are fully displaced into the cabinet. If the problem had been considered transient the pressure would likely be lagging the forcing as the pressure takes time to build. However, the effect of this on the ERPL is assumed to be insignificant and is thus not investigated further.

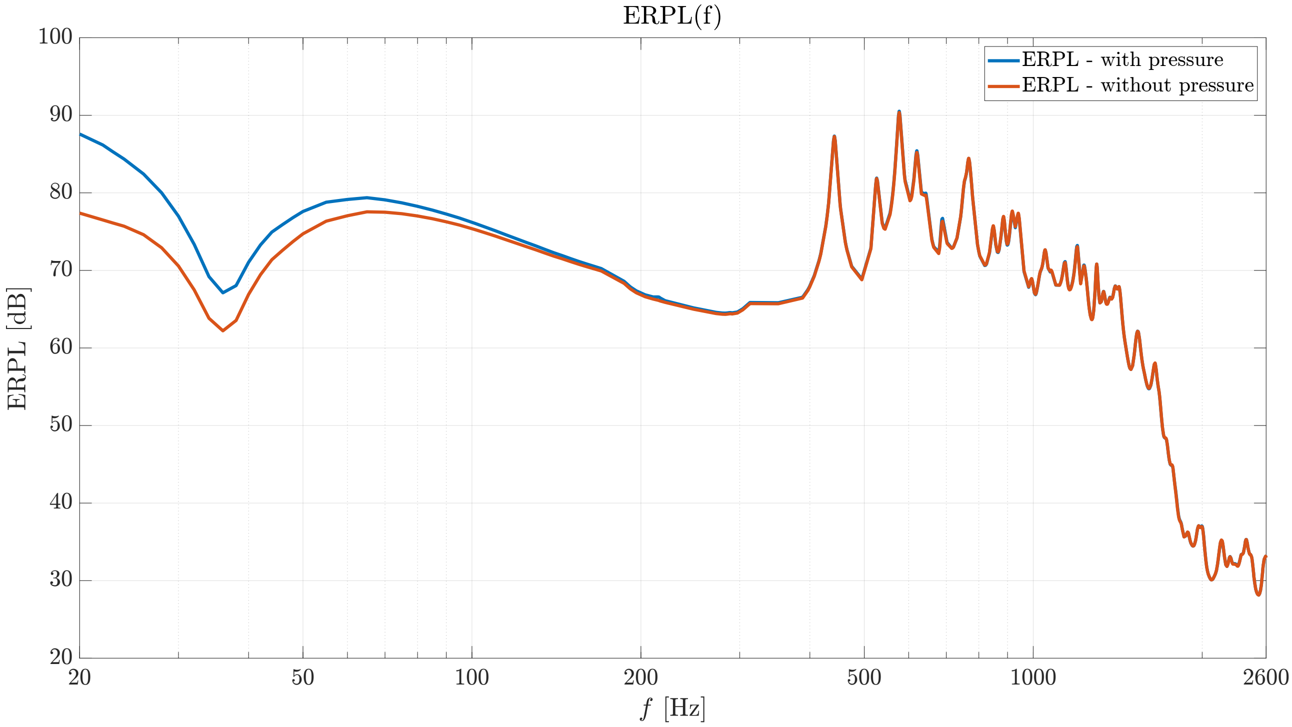

Figure 4.22: ERPL from all exterior MDF surfaces of the cabinet, with and without the inclusion of pressure.

4.3.4 Experimental validation

In this section, the final benchmark analysis is validated against the experimental results and the frequency range of interest is found based on the ERPL predicted by the benchmark.

The benchmark analysis has a total solution time of ≈80 min, distributed over the modal analysis taking ≈5 min and the harmonic analysis taking ≈75 min.

Figure 4.23 again plots the u-displacement as a function of the frequency at the point B_{22} for the benchmark and the experiment. The overall correlation between the benchmark and the experiment at this discrete point is excellent. The benchmark is leading the experiment at the port frequency, however, this is of little interest as the bass reflex ports are to remain unchanged. The benchmark is unable to capture the peak at 367 Hz, but predicts the peaks at 447 Hz, 582 Hz and 618 Hz very well. After 650 Hz the benchmark does not match one-to-one with the experiment, however, the general variation of the response is still modelled fairly well.

The correlation between the displacements predicted by the benchmark and those measured in the experiment at all points, L_{ij} and B_{ij}, are seen in Appendix A. It is evident that a similar degree of correlation, as is seen in Figure 4.23, is also present at the other B_{ij} points. A less satisfactory correlation is seen at the points L_{ij}, however, due to the accelerometer measuring normal to the surface, and the direction of the forcing being parallel to the surface, the amplitudes are smaller in the direction normal to the left side. As the displacements in the normal direction at the left side points are smaller, the correlation between the experiment and the benchmark is of less importance on the left side compared to the back.

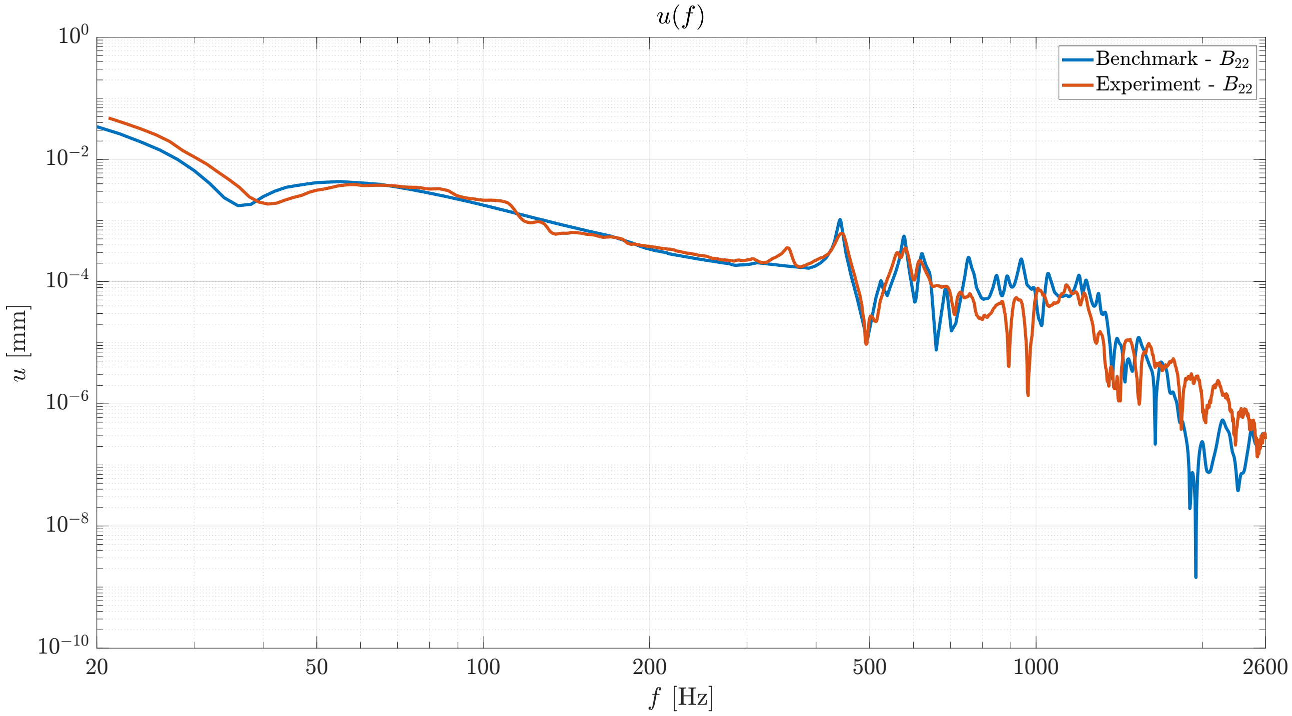

Figure 4.23: u-displacements in point B_{22} from benchmark and experiment.

Figure 4.24 plots the difference between u-displacements in point B_{22} between the benchmark and the experiment against the tolerance of the measurement. Generally over the entire frequency range the tolerance is lower than the difference, i.e. there is a difference between the benchmark and experiment that cannot be explained by the tolerance of the measurements. However, the difference is, at all frequencies except at around 900 Hz, less than a magnitude larger than the tolerance, meaning that the difference is fairly close to being accounted for by the tolerance.

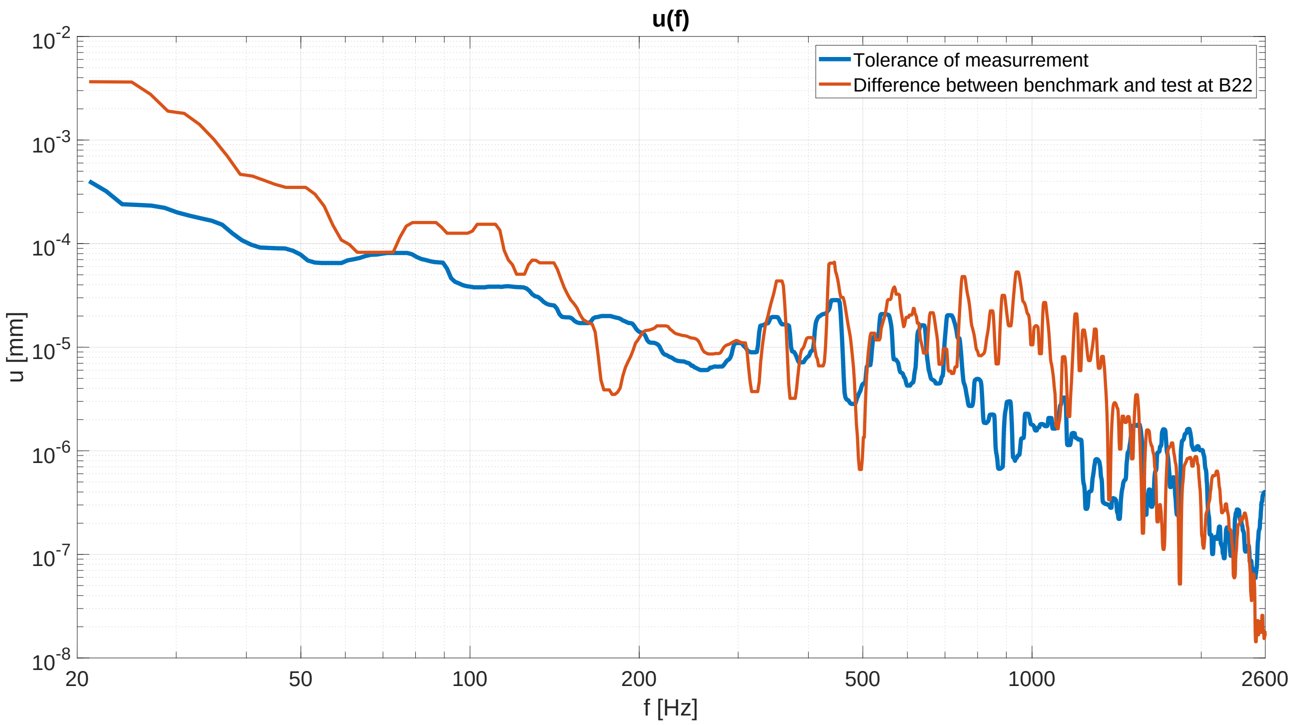

Figure 4.24: Difference between u-displacements in point B_{22} between benchmark and experiment plotted against the tolerance of measurement, defined in Figure 4.14.

Lastly, the ERPL of all exterior MDF surfaces of the cabinet is plotted in Figure 4.25. The frequency range of interest is set from 300 Hz to 1000 Hz. Frequencies from 0 Hz to 20 Hz are not excited by the drivers and are thus not of interest. The frequencies from 20 Hz to 37 Hz, i.e. up to the port frequency, do not contain any eigenfrequencies in the benchmark analysis, meaning that the response is dominated by the forcing and would thus be difficult to change by altering the internal supports in the cabinet. From 37 Hz to 192 Hz no eigenfrequencies are found, as the first non-zero eigenfrequency is at 192 Hz. From 192 Hz to 300 Hz there are eigenfrequencies, however, the magnitude of the ERPL is small in this range, indicating that little sound is radiated from the cabinet. The frequency range of interest is thus set from 300 Hz to 1000 Hz, as all frequencies below either have no eigenfrequencies or the magnitude of the ERPL is small. The magnitude of the ERPL at all frequencies above 1000 Hz is also small and is thus not of interest. The tightest frequency range of interest is from 442 Hz to 765 Hz. However, the range is broadened to 300-1000 Hz to account for the movement of the eigenfrequencies when the geometry of the cabinet is changed. In the figure, the five peaks with the largest ERPL value are indicated along with their associated frequency. In Figure 4.26, the mode shapes associated with each peak are seen.

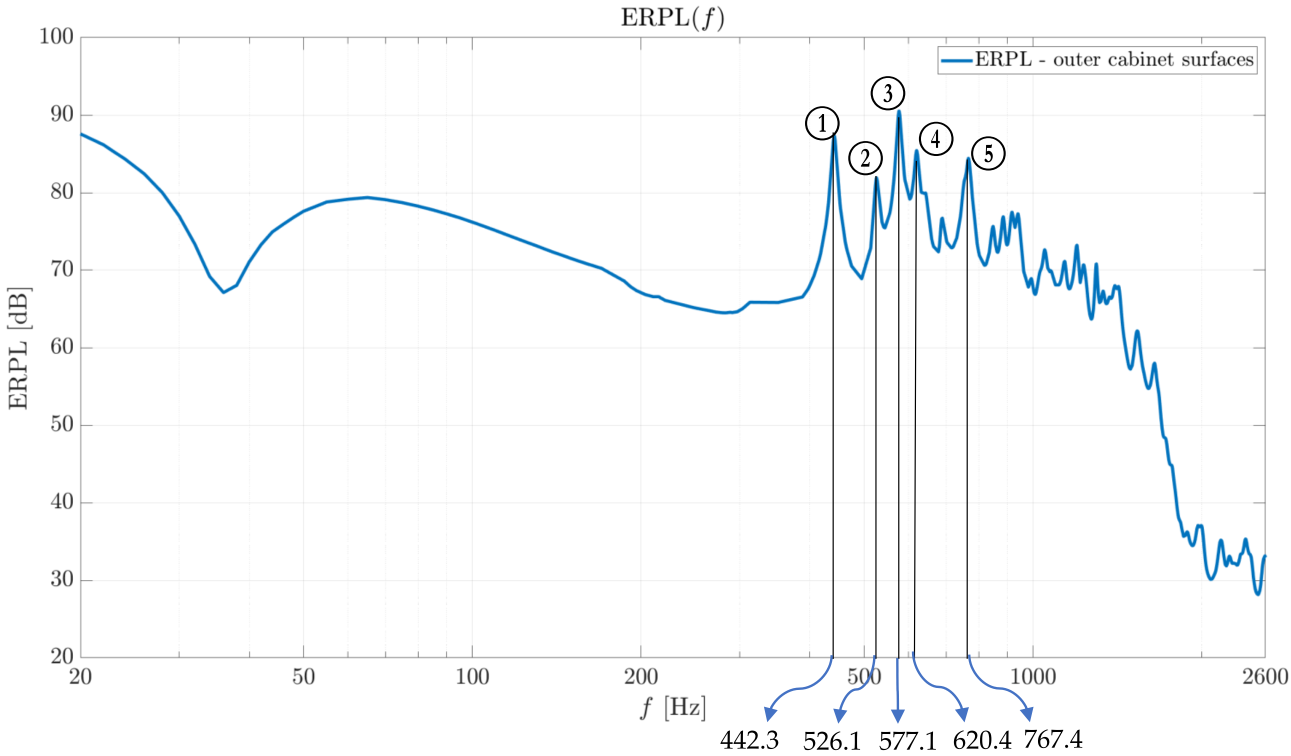

Figure 4.25: ERPL-frequency plot of all exterior MDF surfaces of the cabinet from the final benchmark model.

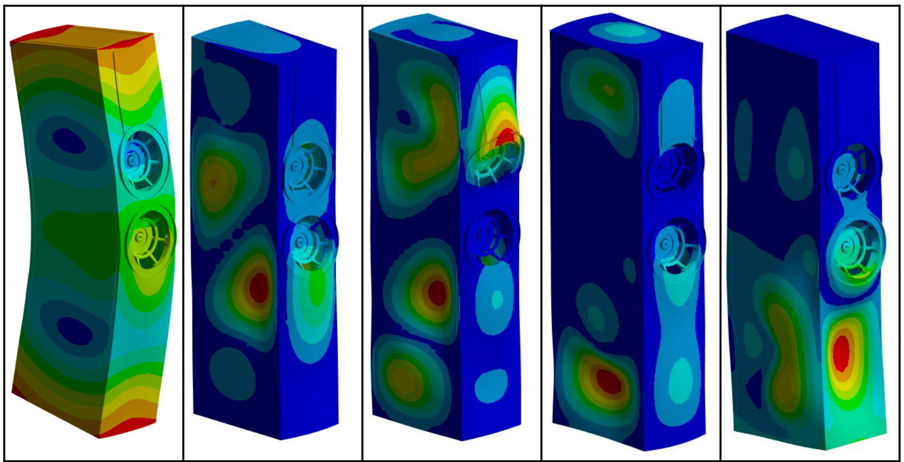

Peak 1	Peak 2	Peak 3	Peak 4	Peak 5
Mode 14	Mode 16	Mode 19	Mode 21	Mode 28
442.3 Hz	526.1 Hz	577.1 Hz	620.4 Hz	767.4 Hz

Figure 4.26: Mode shapes with updated boundary conditions associated with each peak in the ERPL plot.

4.4 Conclusion of sub task 1

A mode superposition harmonic finite element analysis has been developed in ANSYS Workbench called the benchmark model. The benchmark analysis computes the EPRL of all the exterior surfaces of the cabinet as a function of the frequency. A preliminary benchmark analysis using a harmonic unit load was used to design an experiment measuring the acceleration of the cabinet as a function of the frequency using an accelerometer placed at discrete points. The experiment showed that an eigenfrequency predicted by the benchmark at 66.9 Hz, was not present. Based on this, the stiffness of the MDF was decreased and the boundary conditions and forcing were changed. The benchmark analysis was validated against the measured response of the cabinet, where a good correlation was seen between the displacements predicted by the benchmark and the displacements measured in the experiment. Lastly, the frequency range of interest was determined to range from 300 Hz to 1000 Hz based on the ERPL plot from the benchmark model.

Development of design model 5

Sub-task 2: Develop a design model

Develop a finite element harmonic analysis with reduced solution time compared to the benchmark model from sub-task 1, while giving results that are comparable to the benchmark model.

In Chapter 4, a benchmark harmonic analysis was developed and validated by comparison with experimental data. In this chapter, a model that produces comparable results to that of the benchmark model, with significantly reduced solution time is developed. This model is called the design model. Lastly, it is verified that the same geometric change in the design model and the benchmark model results in a comparable change in the response of both models.

5.1 Methods for reducing solution time

There exists a number of different methods to simplify finite element models in order to reduce computation time. However, not all simplifications are relevant or give results comparable to the original model when implemented, as this is highly dependent on the analysis type and the geometry. An example of this is the commonly used symmetry simplification. This simplification is applicable when there exists a symmetry plane in the geometry, the applied boundary conditions and the forcing, such that the results can also be expected to be symmetric. However, in the case of the benchmark analysis, not all mode shapes are symmetric, despite the symmetry plane between the left and right side w.r.t. the geometry, the boundary conditions and the forcing. The symmetry condition is most applicable in linear static structural analyses. This type of simplification is therefore not investigated in this project. The methods for reducing the computation time investigated in this project are listed below.

1. Using fewer elements
2. Changing analysis settings
3. Using a lower element order
4. Using shell elements to replace the cabinet
5. Further simplifications of the geometries
6. Deleting components
7. Using condensed geometries

Of these methods, using fewer elements and changing the analysis settings were implemented. The result of implementing these are described in Section 5.2. This means, however, that the remaining methods were not implemented though they were investigated. The reasons for not implementing these are in short described here.

- **Using a lower element order**
  The element type used in the benchmark model is the SOLID187 3D 10-node element, which exhibits a quadratic displacement behaviour [20, p. 1025]. Instead of using this element, it was investigated whether the SOLID285 linear 4-node element could be used instead. However, it was discovered that faster computation time could be obtained using larger SOLID187 elements rather than using smaller lower-order elements, without significant change in the ERPL plot. The design model therefore still uses elements with a quadratic formulation.
- **Using shell elements to replace the cabinet**
  Shell elements are typically a reasonable simplification for modelling plate-like structures with fewer

degrees of freedom. A shell element is a 2D element that deforms in 3D space. A quadratic shell element has 6 nodes, each with 3 DoF when the topology is triangular. This is significantly less than the 10-node SOLID187 element. Additionally, when using 3D elements, it is typically recommended to use two or more elements through the thickness to capture the bending stiffness. This is not needed for the shell element. However, when considering the front and back walls of the cabinet, it is observed that they are curved on the external face while being flat on the internal face. This means that the thickness of these two walls is not constant and can therefore not be modelled by shell elements. Only the side walls and top and bottom of the cabinet are candidates for being modelled by shell elements. This would however create some practical issues further in the process when generating design concepts, as they must then not invalidate the plate assumptions of the geometries modelled as shells. Using shells would e.g. require that the cabinet sides, top and bottom remain of constant thickness. It was therefore assessed that the decrease in computation time did not outweigh the design limitations.

- **Further simplifications of the geometry**
  It was investigated whether faster computation could be achieved by simplifying the woofer baskets, tweeter plate, ports and terminals further by using very simple geometries, such as completely straight plates and circular disks. This however resulted in a significantly changed ERPL frequency plot. This is likely due to the change in stiffness in these components combined with the fact that they are made from stiffer materials compared to the cabinet. In other words, these components have a large influence on the overall stiffness of the structure.

- **Deleting components**
  Lastly, the influence of deleting the bass reflex ports, the terminal and the tweeter plated was investigated. Again it was evident that the influence of the components on the overall stiffness of the cabinet is large.

- **Using condensed geometries**
  ANSYS has the option of condensing geometries to superelements such that the inertial and flexibility behaviour of the superelement is summarized to a reduced set of DoF. This is achieved by reducing all internal nodes, i.e. nodes that do not contact other geometries, to a single mass- and stiffness matrix of the superelement. The nodes that contact other geometries in the model are called master nodes and are the only nodes from the superelement included in the analysis. [21, p. 1025] The idea is that superelements are not affected by changes to the surrounding geometry, meaning that if all components except the cabinet are condensed to superelements the mass- and stiffness matrix of these are only calculated once despite the geometry of the cabinet being changed. Condensing all components except the cabinet to superelements means that in the optimization only the mass- and stiffness matrix of the cabinet is calculated for each interaction, while the superelements remain unchanged. However, when implemented in the design model, it was discovered that the computation time associated with the bookkeeping of the superelements outweighed the time saved by using fewer DoF.

5.2 Simplifications and results

In this section, the simplifications used for creating the design model are explained. Firstly using fewer elements and the resulting ERPL-frequency plot is presented. Next, a change of the analysis settings is presented. Lastly, it is validated that a change in the geometry in the benchmark still gives similar results to that of the design model with the same geometry changes. In other words, it is validated, that the two models have similar sensitivities to geometry changes.

5.2.1 Using fewer elements

In Section 4.1.2, it was shown that the benchmark had obtained convergence in the eigenfrequencies of interest when meshed with SOLID187 elements with a maximum size of 12.5 mm. It is hypothesized that convergence was achieved in the benchmark at a maximum element size of 12.5 mm as this results in at least two elements through the thickness of the cabinet walls. It was mentioned earlier that two elements in the thickness are recommended for capturing the bending stiffness of structures.

In order to obtain better control over the mesh the cabinet is split into multiple simpler geometries. The sides, top and bottom faces and the internal supports are meshed using SOLID286 elements with a maximum size of 40 mm, while still having two elements through the thickness. The front and back faces, the middle plate separating the upper and lower cavities, the tweeter plate and the terminal are all still meshed using SOLID187 elements but with a maximum element size of 40 mm. Lastly, the woofers are meshed with SOLID187 elements with a maximum size of 25 mm. Figure 5.1 shows the mesh used in the design model.

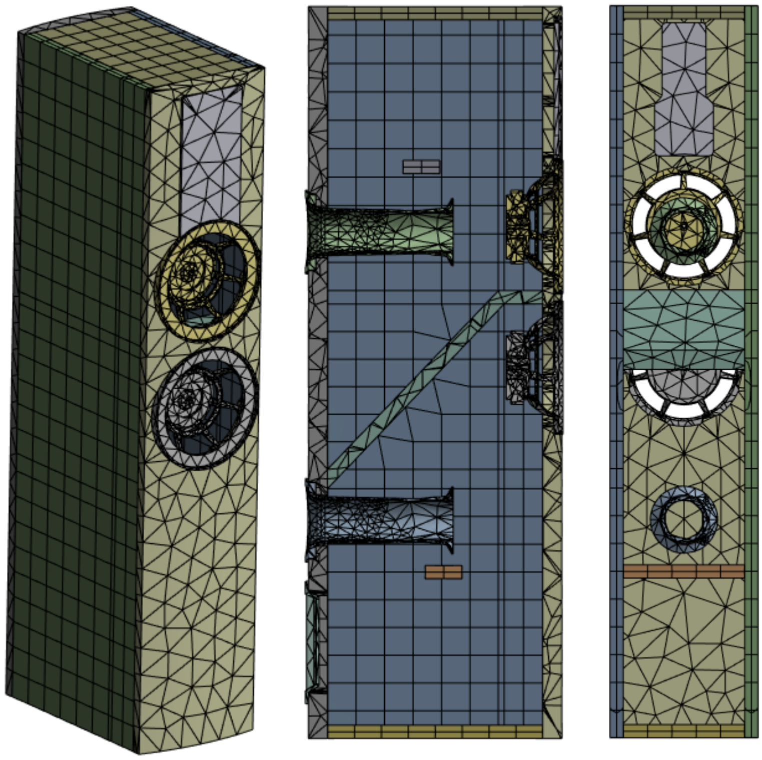

Figure 5.1: Mesh of the design model.

Comparing the solution time between the benchmark analysis and the design model, show that the solution time is reduced from 80 min to 8 min. The solution times are distributed such that the modal is reduced from 5 min to 52 s and the harmonic from 75 min to 7 min.

In Figure 5.2, the ERPL plot obtained from the benchmark model is overlayed with the ERPL plot obtained from the design model. It is seen that the two look almost identical from 20 Hz up to ≈ 850 Hz.

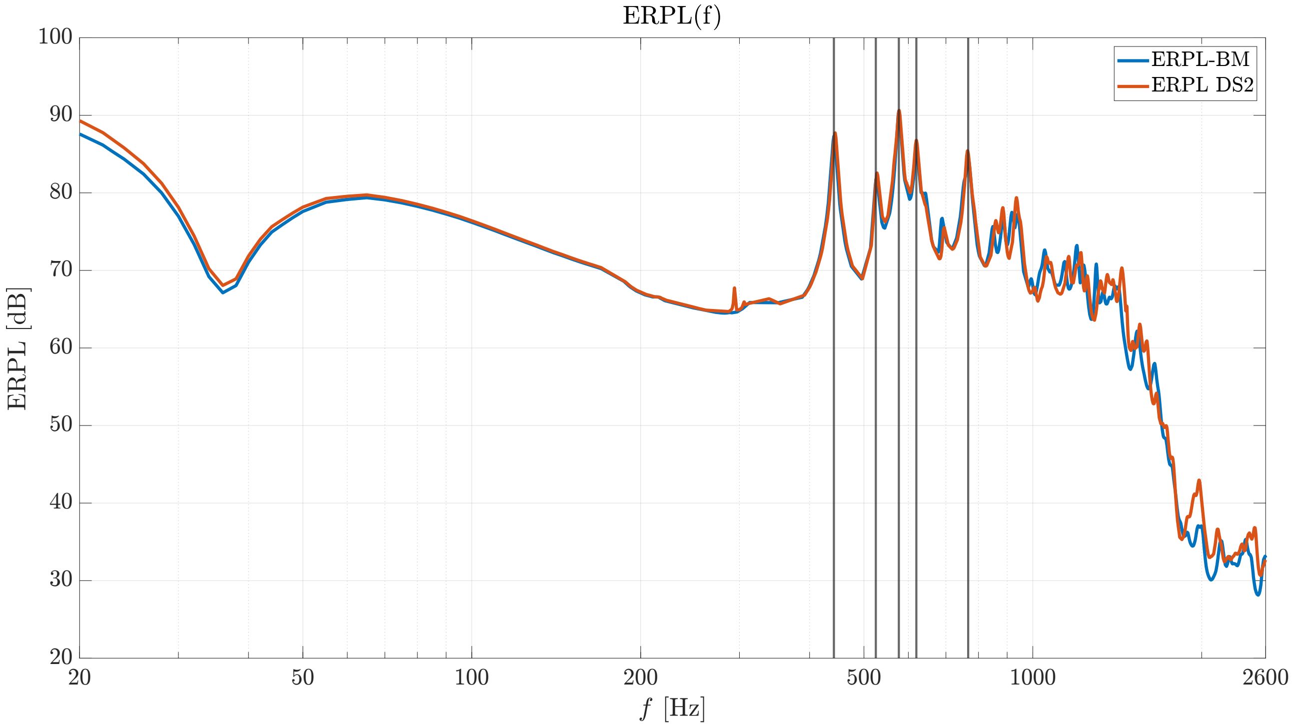

Figure 5.2: ERPL-frequency plot from the benchmark and the design model after reducing the number of elements in the design model.

Further looking at the five peaks indicated by a vertical line in the plot, it can be seen in Table 5.1 that neither the location of the peak nor the ERPL-value differs more than 1.55%. This deviation from the benchmark model to the design model is deemed to be acceptable for further use.

Table 5.1: Comparison of the five peaks indicated in the ERPL plot.

	Peak 1	Peak 2	Peak 3	Peak 4	Peak 5
Benchmark [Hz]	442.3	526.1	577.1	620.4	767.4
Design model [Hz]	444.2	527.6	577.8	619.7	764.9
Deviation [%]	0.43	0.29	0.12	0.11	0.33
Benchmark [dB]	87.32	81.91	90.52	85.43	84.43
Design model [dB]	87.73	82.63	90.62	86.75	85.42
Deviation [%]	0.47	0.88	0.11	1.55	1.17

5.2.2 Changing the analysis settings

It was stated in the conclusion of the benchmark analysis, Section 4.4, that the frequency range of interest looking at the ERPL plot ranges from 300 Hz to 1000 Hz, including a margin at the top and bottom to account for shifting the eigenfrequencies as a result of changing the geometry. The analysis range of the design model is therefore limited to this frequency range of interest, as the objective function of the optimization will only be defined in this range. The modal analysis in the benchmark analysis calculates all eigenfrequencies from 0 Hz to 3900 Hz, while this range is reduced to 0 Hz to 1500 Hz in the design model, such that the mode superposition harmonic analysis still accounts for the frequencies up to 1.5 times the maximum frequency.

The benchmark analysis clusters the ERPL results around the eigenfrequencies calculated in the modal analysis such that the ERPL is calculated 1 time at the eigenfrequency and 12 times close to, in addition to frequencies spaced in a linear interval. These numbers are reduced to 1 and 4 in the design model. The total solution time is reduced from 490 s to 36 s, distributed such that the modal is reduced from 52 s to 22 s and the harmonic from 438 s to 14 s.

Figure 5.3 shows the ERPL as a function of the frequency calculated by the design model from 300 Hz to 1000 Hz overlayed the benchmark analysis from 20 Hz to 2600 Hz. Comparing Figure 5.3 to Figure 5.2, it is evident that changing the analysis settings has no noticeable impact on the resulting ERPL plot. Furthermore, the values previously presented in Table 5.1 are of similar magnitude after the analysis settings are changed.

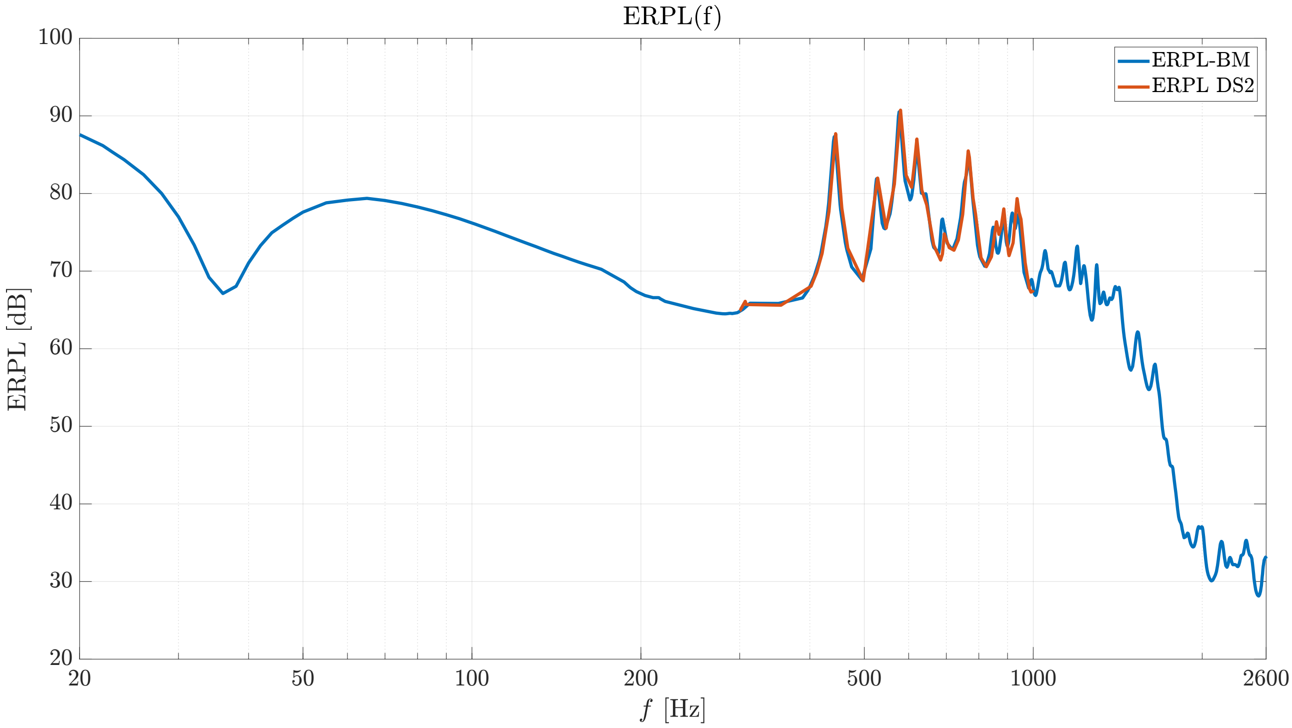

Figure 5.3: ERPL-frequency plot of the benchmark and the design model after reducing the number of elements and the analysis range in the design model.

5.2.3 Validation of sensitivity

As the purpose of the design model is to give a fast, relative to the benchmark, prediction of the ERPL of the cabinet when the geometry of the cabinet is changed, the same change in the design model and benchmark should result in a similar change in the resulting ERPL from both. The sensitivity of each model is therefore investigated by removing the internal supports from both the benchmark and the design model and comparing the resulting ERPL. Figure 5.4 plots the ERPL found using the benchmark and design model without the supports. It is seen that both models predict the same change in the ERPL as a function of the frequency. There are two additional mode shapes in the design model at around 300 Hz, however, after investigating these it is apparent that they are bass reflex port modes and are thus of little interest.

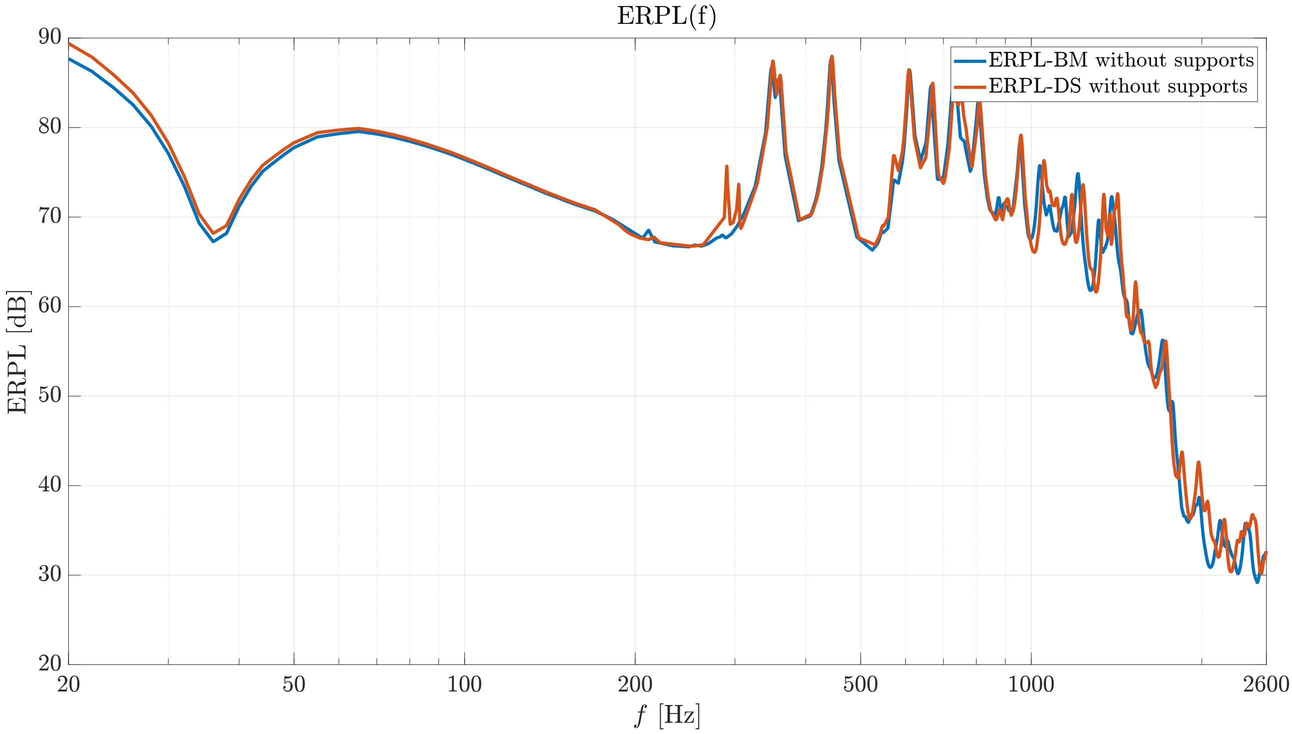

Figure 5.4: ERPL-frequency plot of the benchmark and the design model where the internal supports are removed from both models.

5.3 Conclusion of sub task 2

The benchmark model developed in the previous Chapter 4 has been simplified to the design model in order to reduce the solution time while still giving comparable results of ERPL to those of the benchmark. Various simplifications were investigated, however, only reducing the element size and changing the analysis settings were found to be applicable. The solution time of 80 min of the benchmark is reduced to 36 s in the design model. The results are very comparable, where the largest deviation in the magnitude and frequency of the peaks between the benchmark and design model is 1.55 % and 0.43 %, respectively. Lastly, the internal supports were removed in both the benchmark and the design model, which resulted in a very similar prediction of the change of the ERPL as a function of the frequency between the benchmark and design model.

Repositioning of internal supports using optimization 6

Sub-task 3: Move internal supports using optimization

Parameterize the position of the internal supports. Optimize the position of the internal supports with respect to minimizing the maximum ERPL.

In this chapter, the placement of the existing internal supports is optimized, with the objective of minimizing the maximum ERPL of the exterior MDF surfaces of the cabinet. First, the position of the internal supports is parameterized, and constraints to the parameters are established. Next, the objective function is defined, and the optimization is performed. Lastly, the resulting design is inserted into the benchmark model and its effect on the ERPL is compared against the original design.

6.1 Parameterization

The existing design of the internal supports consists of a single MDF element, glued onto the sides of the cabinet. The position of these MDF supports is parameterized according to Figure 6.1. Here it is seen that each support has two parameters, one for each direction it is allowed to move in. The feasible locations of the supports are visualised as the endarkened areas in the figure, and the locations are chosen such that the supports cannot collide with the bass reflex ports, the tweeter assembly, the crossover assembly or the woofers. Note that the tweeter assembly and crossover are not shown in the picture as they were removed in the initial defeaturing in Section 4.1.1.

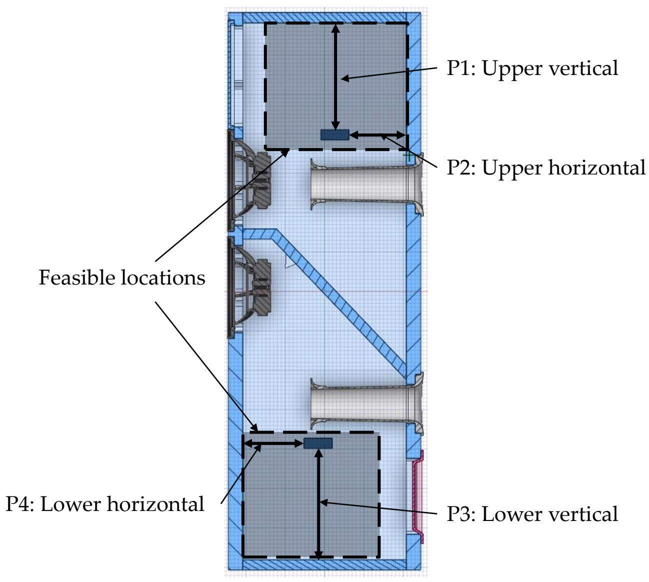

Figure 6.1: Parameterization of the position of the internal supports.

The parameters for the support in the upper cavity are referenced from the top and back surfaces of the cabinet, while the lower support is referenced from the bottom and front surfaces. In Table 6.1, the location of the existing design can be seen along with the lower and upper bounds of the parameters.

Table 6.1: Position of internal supports in the existing design and the lower and upper bounds of the parameters.

Parameter	Existing design	Lower bound	Upper bound
P1: Upper vertical [mm]	190	0	210
P2: Upper horizontal [mm]	126.8	0	200
P3: Lower vertical [mm]	198	0	210
P4: Lower horizontal [mm]	134	0	200

6.2 Objective function

The objective function in this project is the maximum ERPL in the frequency range from 300Hz to 1000Hz, as this was the chosen frequency range to analyze in the design model. This objective function is easily implemented in the DesignExplorer module in ANSYS 2023 R1, as the maximum value of the ERPL can be parameterized in the user interface. Other objective functions can also be used, such as the mean ERPL in this frequency range, or could include the frequency of the ERPL peak in order to include the reverb time. It is however the task of acoustic engineers to define what objective function should be implemented in order to provide "good sound". Additionally, these user-defined objective functions require extensive knowledge of the APDL scripting language and can be time-consuming to implement. As the main objective of this project is to develop a procedure for simulation-driven design of internal supports, this objective function serves as an example of how to perform the optimization. The number of iterations in the optimization scheme is often determined by the nature of the objective function, where highly non-linear objective functions typically require more iterations than linear objective functions. When considering the maximum ERPL there are three reasons why this particular objective function is highly non-linear and therefore requires many optimization iterations.

Firstly, the maximum ERPL reported each time a parameter is changed, could stem from a different peak compared to a previous design point. Recalling Figure 5.3, it is evident that the peaks in the ERPL-plot are of similar magnitude. It is therefore likely that a change in a parameter could lower one peak such that another peak is now the reported maximum peak. This change in the reported maximum peak is only C^0 continuous, as there exists a parameter value where the two peaks are equal in magnitude. However, continuity in the gradient of the objective function cannot be guaranteed. This makes the objective function non-linear.

Secondly, changing the parameters also changes the location of the eigenfrequencies, which when performing the superposition in the harmonic analysis can result in larger deformations from the frequency change alone. This can be seen when looking at the equations for the modal amplitudes (2.59) and the superposition of mode shapes (2.49) from Chapter 2, which are restated below as (6.1) and (6.2) for convenience. Here q_i is the modal amplitude, r_i is the modal load, Ω is the imposed frequency of the load, $\{u\}$ are the nodal displacements and $\{\hat{\Phi}_i\}$ is the mass normalized mode shape vector.

$$q_i = \frac{r_i}{-\Omega^2 + i\Omega 2\zeta_i\omega_i + \omega_i^2} \tag{6.1}$$

$$\{u\} = \sum_{i=1}^{n} \{\hat{\Phi}_i\} q_i \tag{6.2}$$

Looking at (6.1), it is evident that, for $\zeta = 0.01$, as is the case for the MDF the cabinet is made of, the response of the system is largest near the natural frequency ω_i. Now, say there exist two eigenfrequencies ω_1 and ω_2, after computing the two modal amplitudes for these mode shapes, they have to be superpositioned according to (6.2). The response at any frequency is thus a superposition of the response from the two eigenfrequencies. If the two eigenfrequencies are far from each other the effect of the response from ω_1 on the total response at ω_2 is negligible. However, if ω_1 is close to ω_2 the response from ω_1 significantly adds to the total response at ω_2. This is visualised in Figure 6.2, where the responses from ω_1, ω_2 and the summed response are seen with $\zeta_i = 0.01$ and $r_i = 1$ for both $i = 1, 2$. To the left $\omega_2 = 1.2\omega_1$ and to the right $\omega_2 = 1.05\omega_1$.

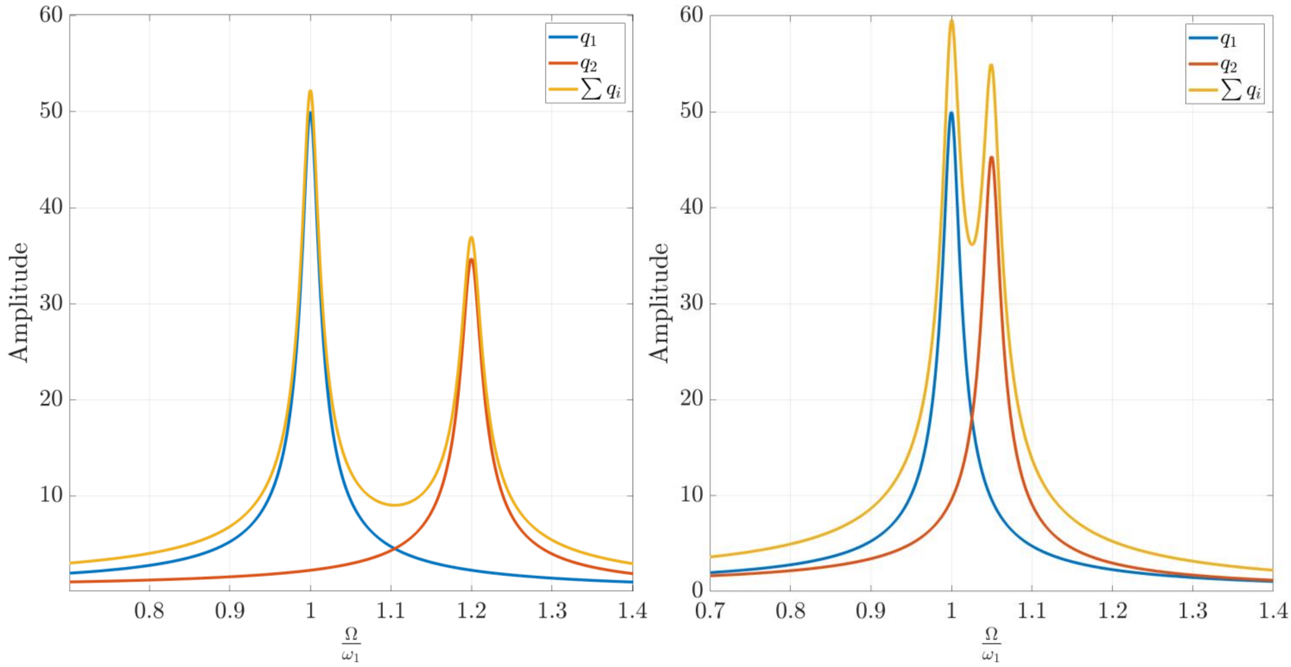

Figure 6.2: Effect of distance between two eigenfrequencies on the mode superposition harmonic response.

It is evident that moving the two eigenfrequencies closer to each other increases the sum of the modal amplitudes, which will increase the total response. It is also interesting to note that in Figure 6.2, the peak modal amplitude decreases as ω_i increases. This is however naturally due to the second term in the denominator in (6.1) as was explained in further detail in Section 2.3. These effects from the mode superposition make the objective function nonlinear, as the ERPL at a certain frequency is dependent not only on the amplitudes of the individual modes but also on the distance between the different modes. Additionally, moving all the eigenfrequencies while keeping the distance between them constant, also changes the ERPL due to the second term in (6.1).

Thirdly, the force applied to the system is highly non-linear with respect to the frequency. Recalling Figures 4.20 and 4.21 on page 38, the external force is a non-linear function of the frequency. This again means that moving the eigenfrequencies could potentially move it to a frequency range where the force is significantly larger or lower. Thus also making the objective function nonlinear.

6.3 Optimization and results

Initially, it was investigated if it would be beneficial to construct a surrogate model, using the sparse grid, as explained in Section 2.5.3. The advantage of using a surrogate model is that if an acceptable model can be created then the subsequent evaluations of the objective function in the optimization will be faster. However, it was observed that constructing the surrogate model with an acceptable accuracy resulted in more evaluations of the design model, compared to using an optimization algorithm directly on the design model.

The optimization scheme used in this project is thus a zero-order genetic algorithm as outlined in Section 2.5.2. This method is chosen as no gradient information is available without performing forward difference or central difference approximations. Additionally, as the objective function is highly non-linear, the number of evaluations needed for gradient-based methods to converge is highly dependent on the initial design. Furthermore, there is the possibility that the gradient-based optimization methods will converge to a local minimum in the feasible domain rather than the global minimum. This is mitigated by using a genetic algorithm, which starts with an initial population that covers the feasible domain. The risk of not converging to the global minimum in the feasible domain is thus mitigated. The initial population size is 32 evaluations, and the population size for each subsequent iteration is also 32. The stability percentage is 2%. The optimization took 7 iterations resulting in 224 evaluations, taking a total of 7 hours, including the solution time, and the time it took for ANSYS 2023

R1 to update the geometry. In Figure 6.3, the maximum ERPL value for each design point as a function of the number of iterations can be seen.

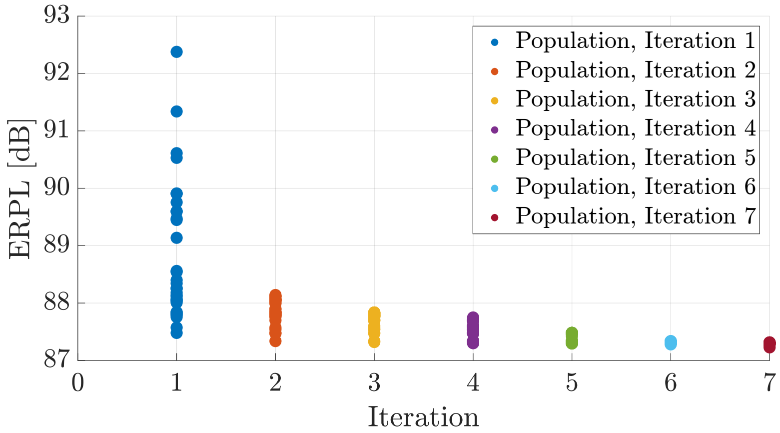

Figure 6.3: Maximum ERPL as a function of iterations in the optimization algorithm.

In Figure 6.4 the position of the optimized internal supports is seen. In Table 6.2, the parameters resulting in the lowest maximum ERPL are seen along with the ERPL value, compared to those of the existing design. Additionally, the maximum ERP of both designs and %-deviation from the existing design is seen.

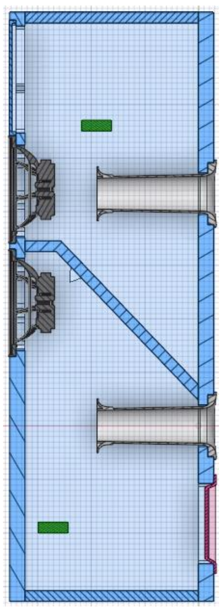

Figure 6.4: Final optimized design.

Table 6.2: Parameters obtained from the optimization and the resulting ERP and ERPL, compared to the existing design from the design model.

Parameter	Optimized result	Existing design
P1: Upper vertical [mm]	163.5	190
P2: Upper horizontal [mm]	195.7	126.8
P3: Lower vertical [mm]	76.9	198
P4: Lower horizontal [mm]	22.2	134
Maximum ERPL [dB]	87.23	90.62
Maximum ERP [W]	5.35×10^{-4}	1.15×10^{-3}
%-deviation (ERP) [%]	-53.14	-

The design model predicts that ERPL will be reduced by ≈3 dB, from 90.62 dB to 87.28 dB. Recalling the definition of ERPL in Section 2.1.3, and converting this back into equivalent radiated power, the ERP is reduced from 1.15×10^{-3} W to 5.35×10^{-4} W. In other words, the optimized position of the existing internal support is predicted to reduce the ERP of the exterior MDF surfaces of the cabinet by more than 50%. However, these predictions are from the design model and need to be validated by inserting the optimized design into the benchmark model.

Before the optimized design is validated against the existing design in the benchmark model, the design model is compared to the benchmark model. This is done as a final check to ensure the design model has not deviated significantly from the benchmark. In Figure 6.5, the ERPL as a function of the frequency of the optimized design from the benchmark model is plotted against the optimized design in the design model.

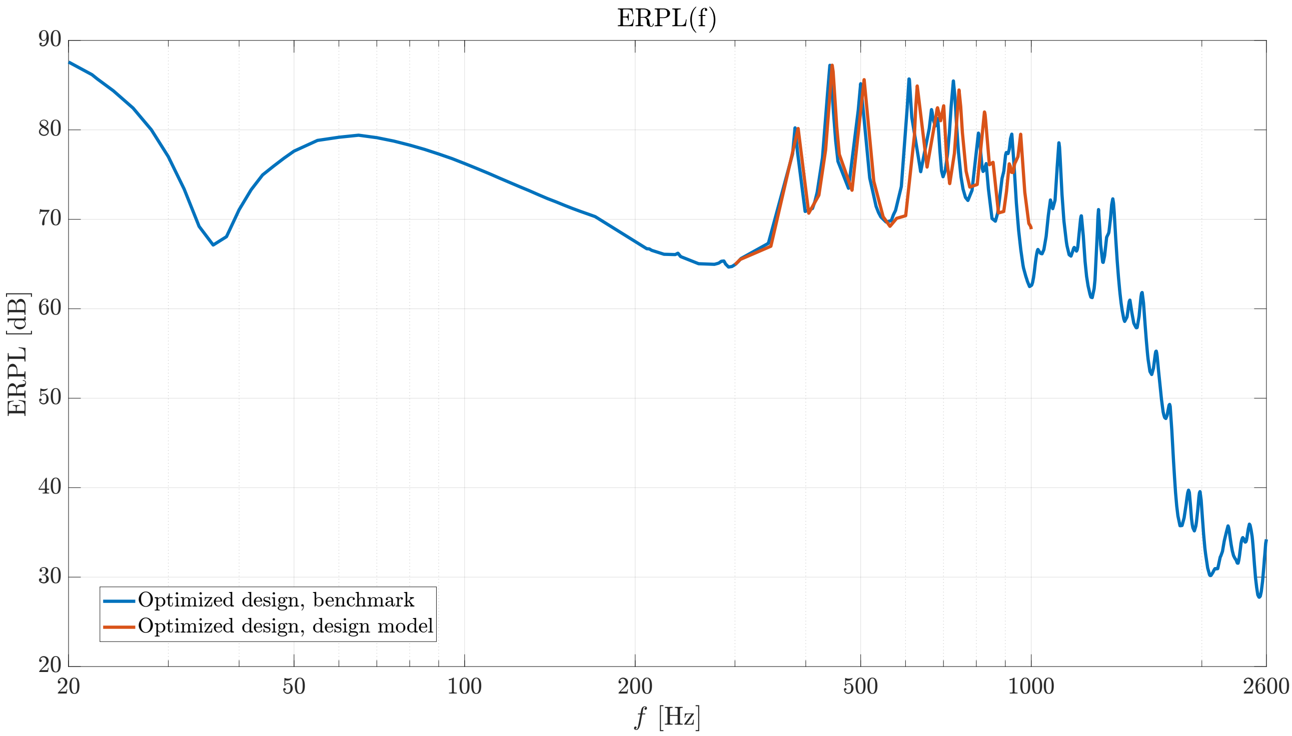

Figure 6.5: ERPL-frequency plot of the optimized design from the benchmark and design model.

In the figure, it is clearly seen that there is still a good correlation between the benchmark and the design model. This validates the assumption that using the design model, as opposed to the benchmark model, for optimization is acceptable. The peaks in the benchmark are predicted to be at lower frequencies for all peaks compared to the design model. However, from 608 Hz and up the location of the peaks in the benchmark are at significantly lower frequencies. Looking at the mode shapes of each model at the peaks at 608 Hz and 629 Hz, confirm that the two mode shapes are the same. This is also true for the remaining peaks. The benchmark is believed to have lower eigenfrequencies than the design model due to the eigenfrequencies converging from above in a modal analysis. In other words, the eigenfrequencies obtain lower frequency values with decreasing mesh size for formulations using a consistent mass matrix formulation, which is used in ANSYS 2023 R1 [11, p. 383]. Figure 6.6 shows the two modes from the benchmark and the design model.

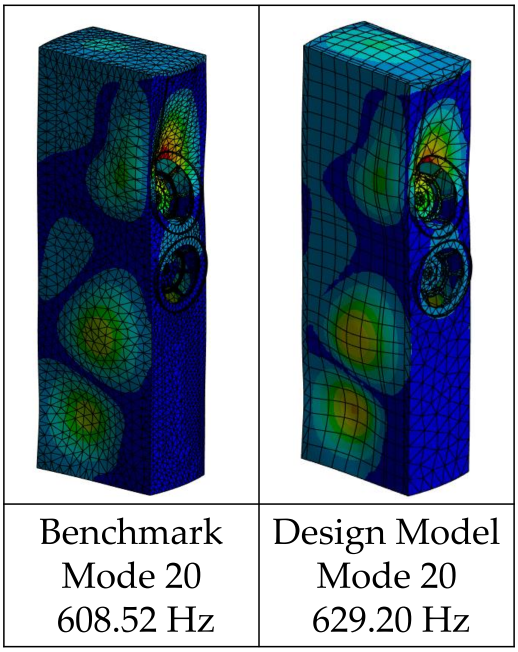

Figure 6.6: Mode shapes from the benchmark and design model of mode 20.

6.4 Comparison of designs

In Figure 6.7, the ERPL as a function of frequency can be seen for the existing design, the optimized design and the design without internal supports, all in the benchmark model.

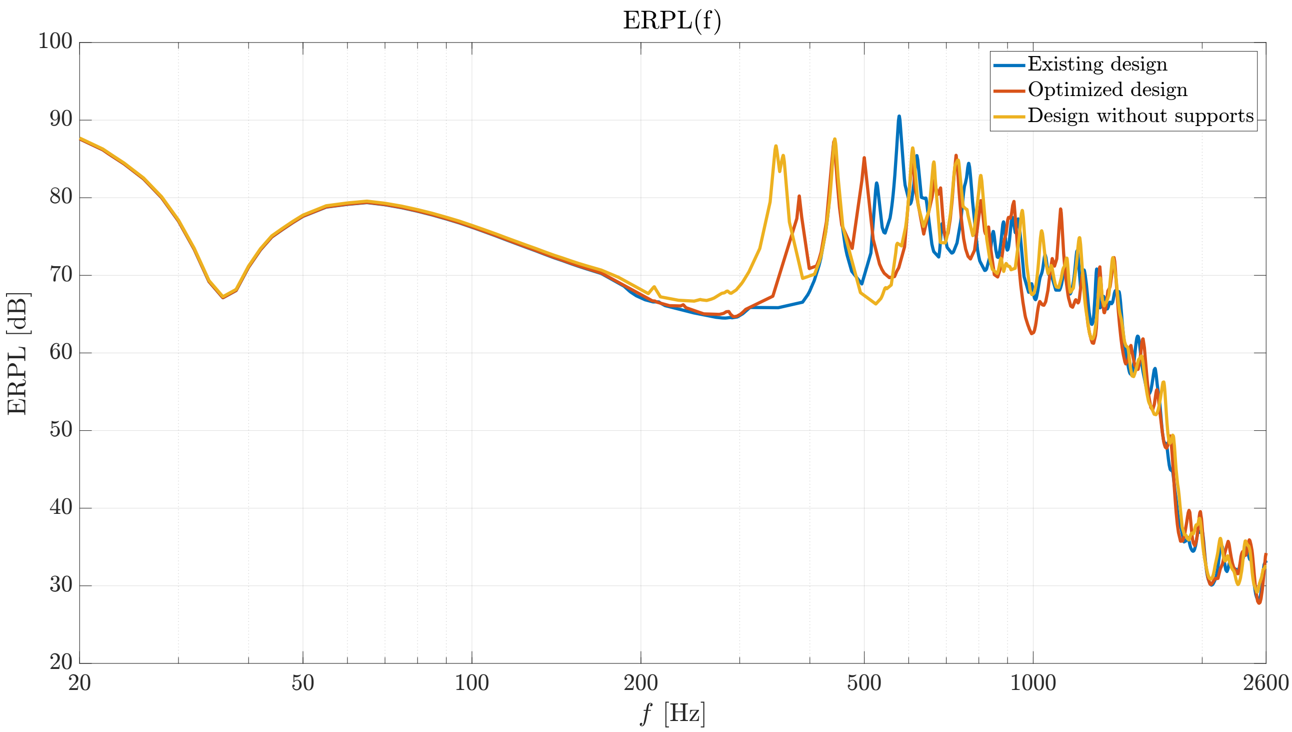

Figure 6.7: ERPL-frequency plot of the optimized design, existing design and design without supports.

In the figure, it is evident that the worst design is the existing design as it shows the largest peak in ERPL of all the designs. The next best is the design without the internal supports, as the peak at 443 Hz is slightly larger than that of the optimized design. This means that the best design is the optimized design. Quantifying the difference between all the designs, Table 6.3 shows the maximum ERPL, ERP, and %-deviation in ERP from the existing design for all designs in the frequency range from 1000 Hz to 2600 Hz.

Table 6.3: Maximum ERPL and ERP of optimized and existing design from benchmark model.

	Optimized design	Design without supports	Existing design
Maximum ERPL [dB]	87.22	87.58	90.52
Maximum ERP [W]	5.27×10^{-4}	5.72×10^{-4}	1.13×10^{-3}
%-deviation (ERP) [%]	-53.23	-49.18	-

From the table, it is evident that the optimized design is the best design. The maximum ERPL is reduced by 3.3 dB in the optimized design compared to the existing design, corresponding to more than a halving of the maximum ERP. The design without supports is almost as good as the optimized design, with a reduction of 2.94 dB compared to 3.3 dB, meaning that the maximum ERP is essentially also halved by just removing the supports.

Another way to compare the designs is to compare the mean ERPL. However, it is not necessarily meaningful to take the mean over the entire frequency range from 20 Hz to 2600 Hz, as little to no changes in ERPL occur in the range from 20 Hz to 300 Hz. Additionally, in the range from 1000 Hz to 2600 Hz, the ERPL is relatively low compared to values in the 300-1000 Hz range and is thus not considered important. Also, the task of finding the mean ERPL value in the 300-1000 Hz range is not as simple as taking the arithmetic mean, as the solutions in frequency are not evenly spaced, as mentioned in Section 5.2.2. Solutions are clustered around eigenfrequencies, which will give a higher weight to some frequency ranges than others when taking the arithmetic mean. Instead, integrating the curve and dividing it by the frequency range gives a mean value that gives equal weight in frequency. When dealing with numerical data of non-equally spaced points, (6.3), also known as the trapezoidal method [22, p. 251-261], can be used for an approximation of the integral.

$$\int_a^b ERPL(f)df \approx \frac{1}{2}\sum_{n=1}^{N}\left((f_{n+1}-f_n)[ERPL(f_n)+ERPL(f_{n+1})]\right), \quad \text{where} \quad a = f_1 < f_2 < \cdots < f_N < f_{N+1} = b \tag{6.3}$$

Where, in this case $a = 300$ Hz and $b = 1000$ Hz. Dividing this with $\Delta f = 700$ Hz gives the mean value. In Table 6.4, the mean value of ERPL and ERP of the existing, the optimized and the design without supports can be seen along with the %-deviation from the existing design of the ERP.

Table 6.4: Comparison of mean ERPL from 300 Hz to 1000 Hz from the existing design, optimized design and the design without supports.

	Optimized design	Design without supports	Existing design
Mean ERPL [dB]	74.52	74.87	74.33
Mean ERP [W]	5.95×10^{-5}	7.03×10^{-5}	7.19×10^{-5}
%-deviation (ERP) [%]	-17.25	-2.2	-

In the table, in addition to the optimized design having the lowest maximum ERPL, it can be seen that the mean ERP is also the lowest for the optimized design. The mean ERPL however, is not lower than that of the existing design. This stems from the fact that ERPL is a logarithmic scale. The ERP for the optimized design in general have a slightly higher ERP than the existing design in frequencies between the peaks, however, the existing design in general has much higher peaks. When converting to dB, a difference in say, 0.001 W to 0.01 W is the same difference in dB as when going from 0.01 W to 0.1 W, even when the absolute value in W is much larger. The same can be seen for the design without supports. The design without supports has a higher mean ERPL and mean ERP, than that of the optimized design, and is an inferior design based on the mean values alone. The optimized design has a higher mean ERPL than that of the existing design, and could by that metric be seen as the inferior design. However, it is very important to note that the optimized design was optimized with an objective function that only accounts for the maximum ERPL. It is very likely that, if the mean ERP or ERPL were chosen and implemented as the objective function, the optimized design would be better than the existing design based on the mean ERP and ERPL.

6.5 Conclusion of sub-task 3

The position of the supports was parameterized and the objective function of minimizing the maximum ERPL in the frequency range of 300-1000 Hz was chosen. The optimization was performed using a zero-order genetic algorithm, which converged after 7 iterations after having performed 224 evaluations of the design model developed in Chapter 5. The optimized design was evaluated in both the design model and benchmark model which yielded similar results in ERPL, confirming once again that the design model is an acceptable approximation of the benchmark model. Lastly, the optimized design, the design without supports and the existing design were compared against each other in the benchmark model. Using the maximum ERPL and ERP as the sole metric for evaluating the performance of the designs results in the optimized design being the best design, with the design without supports being almost as good. The optimized design showed a decrease in maximum ERPL of 3.3 dB, corresponding to a 53% decrease in the ERP, compared to the existing design. Alternatively, using the mean ERPL as the metric showed that the existing design was the best, however, the mean ERP still favoured the optimized design.

Redesign of internal supports using optimization 7

Sub-task 4: Develop an alternative internal support structure

Develop an alternative internal support structure to exemplify the possible reduction in maximum ERPL when the design is less restricted.

In this chapter, an alternative internal support structure is developed to exemplify the possibilities of using simulation-driven design in a less restrictive context than what was demonstrated in the previous chapter. It is believed that a new design can obtain better results than by simply repositioning the existing internal supports, which was done in Chapter 6. The alternative support structure is a general bracing structure that is parameterized. The sensitivities of the parameters are investigated to determine if the number of parameters can be decreased. The optimization is then performed with an objective function of minimizing the maximum ERPL while constraining the allowed volume reduction to 5%.

7.1 Initial design concept

The initial design concept is a general bracing-like structure for all the cabinet faces in order to demonstrate how a better cabinet design can be achieved with little to no creativity and knowledge about the response of the cabinet. The initial design concept can be seen in Figure 7.1.

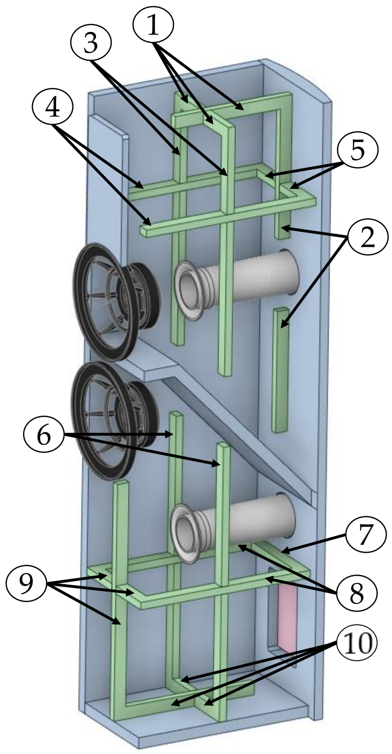

Figure 7.1: Initial design concept. Some faces of the cabinet are hidden in order to see the internal supports. P1-10 indicate the parameterized faces.

All the bracing in Figure 7.1, is made from MDF, with material properties identical to those of the cabinet. It has been requested by DALI A/S, that all internal supports have to be made of the same material as the cabinet. The reason for this is that during transportation of the speaker to the customers, the speaker can undergo both very high and low temperatures. If the supports are made of a material with a different coefficient of thermal expansion to that of the cabinet, the glue assembly might fail, and the supports would no longer be connected to the cabinet. In order to avoid this issue, it is simply a requirement that the cabinet and supports both are made of MDF. The thickness of each brace is a constant 12 mm. All the braces have their depth into the speaker parameterized for a total of 10 parameters. The numbers in the figure represent the parameter number. Due to the mid-plane of the cabinet sidewalls being a symmetry plane, the braces are parameterized such that the symmetry remains.

7.2 Sensitivity analysis

A sensitivity analysis is now conducted to see if the number of parameters can be reduced. The idea is that if any parameters have small sensitivities they can be disregarded, as they have little influence on the resulting ERPL. This sensitivity analysis is a sparse grid initialization [16, p. 88], which works by first evaluating the model with all parameters at their mean value. Next, the model is evaluated an additional two times for each parameter, one time at the minimum value and one time at the maximum value for each parameter, keeping all other parameters at their mean. This does not give sensitivities of the model, but rather a central difference approximation of the sensitivities of each parameter. It is also important to note that no information about any cross-effects of the parameters can be deducted from using this level of a sparse grid.

The sparse grid initialization is performed twice. The parameters are first allowed values from 10 mm to 30 mm which allows them to change from the mean of 20 mm, by 10 mm. Next, the parameters are allowed values from 15 mm to 25 mm, allowing for a 5 mm change from the mean. The two different initializations are made in order to investigate to what degree the objective function, i.e. max(ERPL(Pi)), can be considered linear. If the objective function is linear then the approximation of sensitivities in the two tests should be the same, i.e. constant. However, if the objective function is non-linear then the approximation of sensitivities is not constant. In Figure 7.2 the results from the sensitivity analysis can be seen. On the vertical axis, the change in ERPL from the initial design point can be seen when changing a parameter to its maximum and minimum value, normalized with the change of the parameter. On the horizontal axis, the parameters can be seen with numbers corresponding to Figure 7.1.

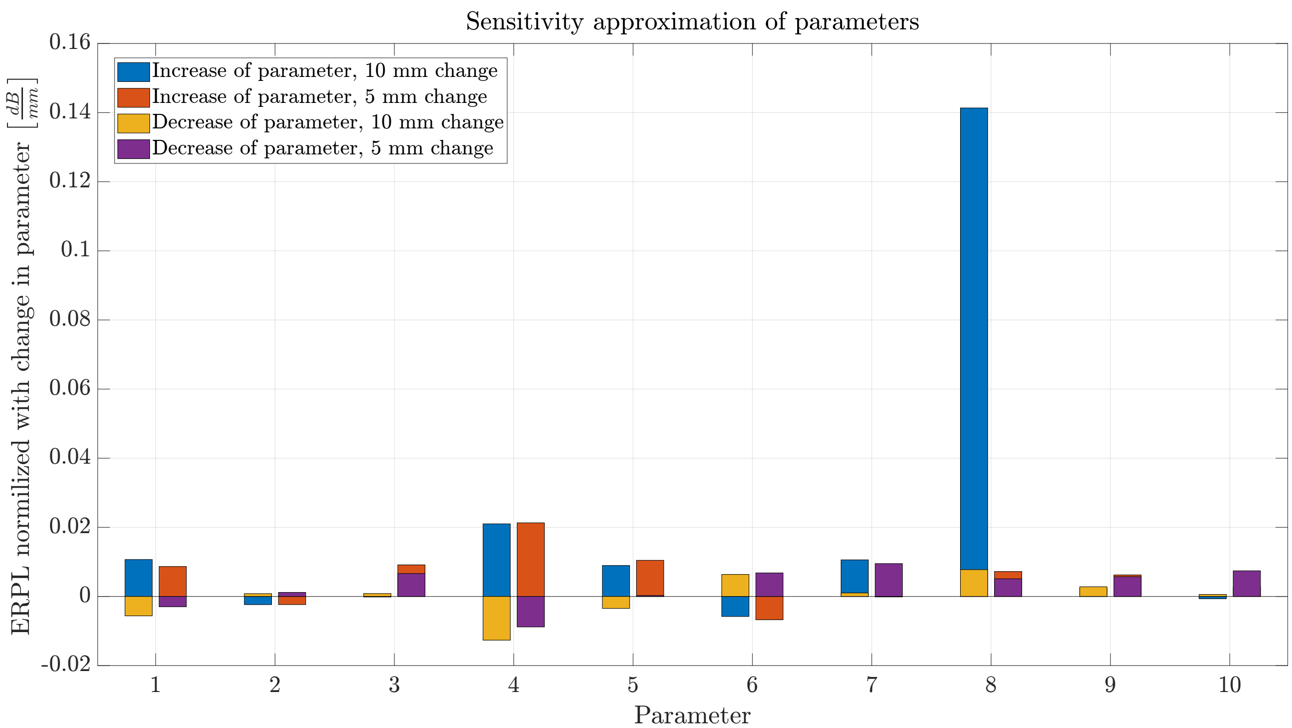

Figure 7.2: Results of the sensitivity analysis using a sparse grid initialization with a change in parameters of 10 mm and 5 mm.

Looking at Figure 7.2, it is seen that the sensitivities differ significantly when performing the central difference approximation with a perturbation of 10 mm compared to a perturbation of 5 mm. In some cases, such as the sensitivities of P2, the sensitivities change signs when changing the perturbation size. It is therefore clear that the objective function is highly non-linear w.r.t. the majority of the parameters at the analysed point. The reasons for this non-linearity are explained in Section 6.2.

A direct result of the objective function being highly non-linear is that the approximations to the sensitivities seen in Figure 7.2, cannot be used to disregard any of the parameters. Even for the parameter P2, which is very small and thus has, based on this sensitivity analysis, little impact on the ERPL. This is because the sensitivities are only calculated around a mean value of 20 mm. As the central difference approximations to sensitivities show that the objective function is nonlinear, it cannot be concluded that P2 has a small sensitivity in the entire design space, as it has been established that the sensitivities are not constant in the design space. The optimization is therefore performed on all 10 parameters shown in Figure 7.1.

7.3 Optimization and results

The optimization is performed with the same zero-order genetic algorithm as was used in the repositioning of the existing supports in Chapter 6. The objective function is likewise to minimize the maximum ERPL in the frequency range from 300 Hz to 1000 Hz. All the parameters are constrained to take values from 1 mm to 45 mm. Additionally, two volume constraints are applied, one for each cavity in the cabinet. In order to prevent too much of the internal volume from being taken up by supports instead of air, DALI A/S has requested that the proposed design cannot decrease the air volume in each cavity by more than 5% from the existing design. Currently, there is 22.23 l of air in each cabinet. Reducing this by 5% gives 21.12 l. As the alternative internal support structure does not include the existing supports in the cabinet, their volume of 0.15 l can also be used for the bracing structure. This results in the constraint that the volume of the supports is not allowed to exceed 1.26 l in each cavity.

The optimization algorithm reached the stability-stopping criterion of 5% after 20 iterations with 80 evaluations in each iteration. This took a total of 50 hours including, solving and updating the model. The parameters obtained from the optimization can be seen in Table 7.1.

Table 7.1: Resulting parameters obtained from the optimization.

Parameter	P1	P2	P3	P4	P5	P6	P7	P8	P9	P10
Value [mm]	1.71	44.01	38.44	9.96	26.80	44.97	17.99	3.07	43.79	23.92

These parameters resulted in the volume of the supports in the upper cavity and lower cavity being 0.53 l and 0.87 l, respectively, meaning that no constraints are violated. The design model, predicts that the maximum ERPL with the parameters seen in Table 7.1 to be dB, which is an approximate decrease of dB and dB from the existing model and optimized model from Chapter 6, respectively. However, this result has to be validated in the benchmark model. In Figure 7.3, the ERPL from the design model with optimized parameters is compared to the ERPL from the benchmark model with the optimized parameters.

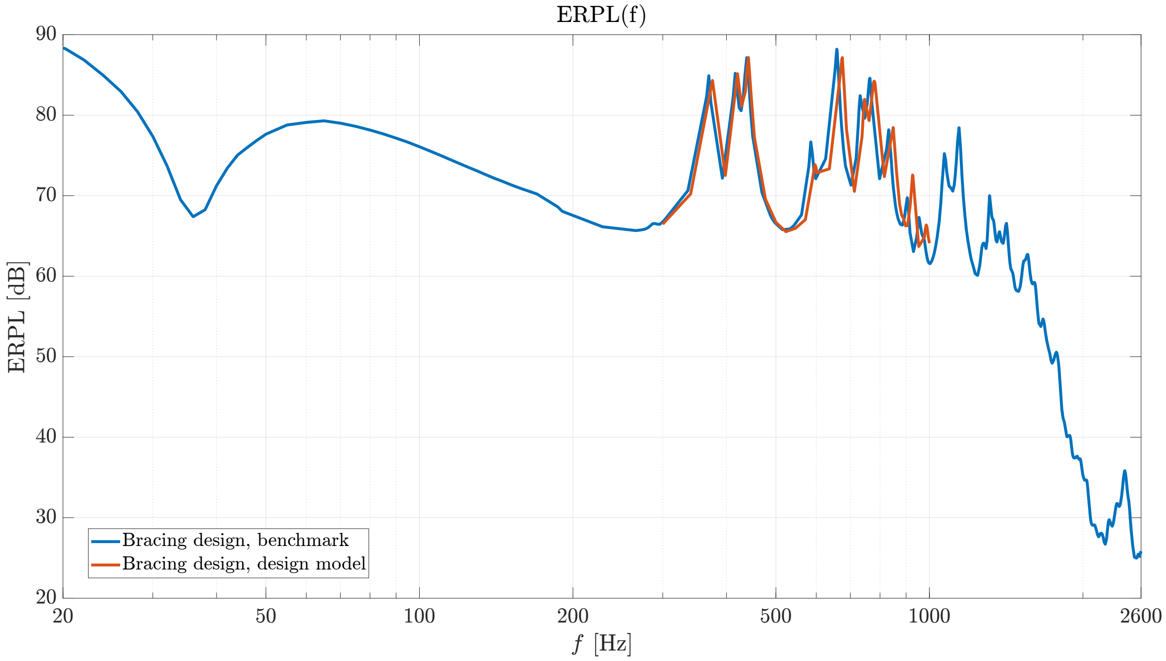

Figure 7.3: ERPL-frequency plot of the bracing design from the benchmark and design model.

In the figure, a tendency similar to that of the same comparison in Chapter 6 is seen. Namely, the correlation between the two graphs is very good, however, the curve from the design model seems to be slightly shifted to the higher frequency range. This is what was also observed in Figure 6.5 in Chapter 6, and can be attributed to the modal analysis converging from above.

7.3.1 Comparison of designs in the benchmark model

In Figure 7.4, the ERPL-frequency plots from the benchmark model of the existing design, design with re-positioned supports and bracing design are seen.

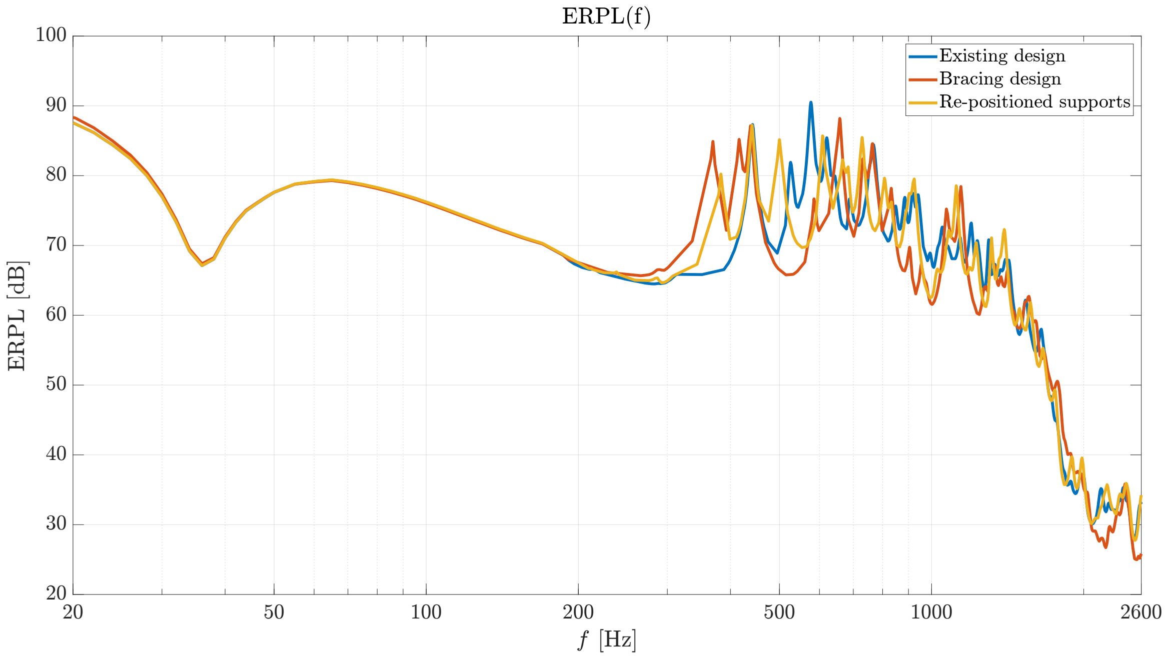

Figure 7.4: ERPL-frequency plot of the existing design, design with re-positioned supports and bracing design.

In the figure, it is evident that the bracing design has a lower maximum ERPL compared to the existing design. Compared to the re-positioned supports design, the peak at 441 Hz, which was the largest peak in the re-positioned supports design, is also lower in the bracing design. However, an additional peak is present in the bracing design at 658 Hz which is the largest peak in the bracing design and is larger than any peak in the re-positioned supports design. This means that the re-positioned supports design is still considered the best design, assuming that the objective function is the sole criterion.

Quantifying the difference between the designs, Table 7.2 lists the maximum ERPL for the designs along with the maximum ERP and %−deviation in ERP from the existing design. In addition to this, the mean values are presented similarly to what was done in Chapter 6.

Table 7.2: Maximum and mean ERPL and ERP of the bracing design, the design with re-positioned supports and the existing design from benchmark model.

	Bracing design	Re-positioned supports	Existing design
Maximum ERPL [dB]	88.19	87.22	90.52
Maximum ERP [W]	6.60×10^{-4}	5.27×10^{-4}	1.13×10^{-3}
%-deviation (ERP) [%]	-41.55	-53.23	-
Mean ERPL [dB]	73.012	74.52	74.33
Mean ERP [W]	6.37×10^{-5}	5.95×10^{-5}	7.19×10^{-5}
%-deviation (ERP) [%]	-11.34	-17.25	-

In the table, it is evident that both the bracing design and the re-positioned support design result in a lower maximum ERPL than that of the existing design. However, it is seen the resulting maximum ERPL from the bracing design is ≈ 1 dB higher than the design with re-positioned supports. This shows that a very general design concept, when optimized, can produce similar, although a bit worse results, than the optimized re-positioning of the existing supports. Looking at this in terms of maximum ERP, the bracing structure resulted in a decrease of 41% compared to the existing design. It is from these results clear that the best design based on the objective function used in this project is the re-positioned supports design. However, the results of the bracing structure still significantly reduce the ERP from the cabinet relative to the existing design, underlining the assumption that a very general initial design can produce better results than the existing design when using a simulation-driven design approach. Looking at the mean ERPL the bracing design is the best compared to the results from the existing design and the re-positioned supports. However, in terms of the mean ERP the re-positioned design is still considered the best. Again the discrepancy in what design is best in terms of mean ERPL and mean ERP stems from the fact that the ERPL is a logarithmic scale. This was also observed and explained in Chapter 6.

7.4 Conclusion of sub-task 4

An alternative internal support structure was proposed in order to exemplify the possibilities of using simulation-driven design for cabinet design. A general bracing structure was proposed to demonstrate that no knowledge about the response of the cabinet is required to propose an acceptable design. The braces were parameterized and their sensitivities were analysed to determine if some of the parameters could be discarded. However, as the objective function of minimizing the maximum ERPL was highly non-linear, none of the parameters could be discarded based on their sensitivities. The optimization was performed using a zero-order genetic algorithm, which converged after 20 iterations after having performed 1600 evaluations of the design model developed in Chapter 5. Validating the optimized bracing design in the benchmark model showed that the maximum ERPL was reduced by 2.3 dB, corresponding to a 41.6% decrease in ERP, compared to the existing design. Comparing the alternative bracing structure developed in this chapter to the repositioning of the supports in the previous chapter, showed that the re-positioned support design is still better than the bracing design. The reduction in ERPL compared to the existing design of the re-positioned and bracing design was 3.3 dB and 2.3 dB, respectively.

8 Discussion

In this chapter, the delimitations stated in Chapter 3, are discussed. The delimitations were set in order to simplify the project. The delimitations and their effect on the project are discussed.

No experiment is performed on the final design: In Chapters 6 and 7 it is concluded that the design with re-positioned supports and the bracing design are both better than the existing design. Those conclusions are of course based on the objective function of minimizing the maximum ERPL, which is the topic of another delimitation, discussed below. However, despite the choice of objective function, a design should naturally always be validated experimentally. This experiment should ideally, unlike the experiment conducted in Chapter 4, measure the sound radiated by the cabinet and not the accelerations. If such an experiment had been conducted the impact on the project would largely depend on the result of the experiment. The design is either accepted and the project concluded, or the design is rejected and an investigation of the cause of the discrepancies between the improvement in radiated sound predicted by the benchmark and measured in the experiment would be launched. The most likely discrepancy is of course due to the choice of objective function.

Only the maximum ERPL is considered as the objective: The objective function used for both optimizations in Chapters 6 and 7 was to minimize the maximum ERPL in the frequency range from 300 Hz to 1000 Hz. This objective function served to exemplify how simulation-driven design using optimization can be used in the design of loudspeaker cabinets, however, it is easy to imagine many other relevant objective functions, such as the reverb time, the location of the eigenfrequencies, etc. Also as mentioned in Section 6.2, the mean ERPL is an equally valid choice of objective function, which in ANSYS, unfortunately, requires extensive knowledge of the APDL scripting language. Additionally, it was also stated in Section 6.2, that the choice of objective function is the task of an acoustic engineer, as they are qualified to define and quantify what constitutes “good sound”. The choice of objective function in the project naturally has a large impact on the optimized designs presented in Chapters 6 and 7. However, the impact of the choice of objective function on the demonstrated simulation-driven design procedure is insignificant, as other objective functions are also expected to work. This is especially true, as the optimization algorithm used in this project, is also applicable to multi-objective optimization problems.

No air is included in any simulations: In this project, the air inside and surrounding the loudspeaker has not been considered. This is done in order to lower the complexities of the simulations and thus reduce the computational time. Including air in the simulation is deemed infeasible in the design model used in the optimization as the computation time would simply be too large. However, the benchmark model which prioritizes accuracy, rather than computational speed, could potentially benefit from the inclusion of air, as results such as the pressure in the air surrounding the cabinet would become available. It is expected that the pressure in the surrounding air could lead to a better prediction of the radiated acoustic power, compared to the ERPL which disregards the phase shift between the pressure and velocity. This is expected to improve the benchmark as a validation tool for both the optimized design and the choice of the objective function. However, it is not expected to improve the result from the optimization as it is important to recognize that the advantages of including air in the benchmark model can only improve the design if the same results could be obtained in the design model without the inclusion of the air, as the optimization ultimately has to be performed on the design model.

Only the woofers are considered: In all analyses performed in this project the dome and ribbon tweeter has been ignored in order to reduce the complexity of the simulation, and in order to reduce the frequency range analysed. Additionally, it would also not be feasible to measure the tweeter with an accelerometer. The soft dome tweeter, is, exactly what the name implies, a soft dome, which means that the accelerometer cannot be applied without damaging the tweeter. Furthermore, even if the accelerometer could be applied to the tweeter, the moving mass of the tweeter itself is less than the mass of the accelerometer of 0.75 g. This would significantly change the behaviour of the tweeter, and the measurements would not give any relevant data. However, the effects of the tweeter are not expected to significantly contribute to the response of the ERPL at any frequency range. Firstly, the moving mass of the tweeter is 0.6 g, which is more than an order of magnitude less than that of the woofer. With comparable accelerations of the tweeter and the woofer, the force applied to the cabinet from the accelerating mass of the tweeter would also be more than an order of magnitude lower. In addition to this, the displacement and the area of the tweeter are also significantly lower than that of the woofer. This leads to a smaller pressure change in the cabinet from the moving tweeter compared to the moving woofer. In other words, no significant forces applied to the cabinet can be attributed to the tweeter, and it can thus be safely ignored from this analysis. All of these points are true for both the soft dome tweeter and the ribbon tweeter.

Only one loudspeaker is analyzed: In this project only the Rubicon 6 loudspeaker is analysed, while DALI A/S has a wish of developing a procedure for using simulation-driven design when designing cabinets for all their loudspeakers. However, DALI A/S has no intentions of implementing any of the proposed designs in this project, despite that the benchmark model has predicted that both the design with re-positioned supports and the bracing design has a lower peak ERPL, than that of the existing design. This is because the Rubicon 6 loudspeaker is already in production and has been since 2014, which is also true for the other loudspeakers in the Rubicon series. However, by demonstrating that using simulation-driven design it is possible to further improve a well-renowned loudspeaker, which is already sufficiently good to be sold, is a good demonstration of the advantages of simulation-driven design. It is believed that the impact of choosing another loudspeaker than the Rubicon 6 is little, as the project illustrates a general procedure for designing a loudspeaker cabinet that is applicable to a wide range of cabinets.

No non-linear vibration analyses are performed
In this project, only the theory of linear vibration analysis is presented and used in simulations to asses the radiated power from the cabinet surfaces. This means that no non-linear effects are investigated at any point during this project. However, looking at the comparison of displacements between the benchmark model and the experiment, it seems that linear vibration theory is sufficient to model the response of the loudspeaker cabinet. Non-linear vibrations were thus not investigated, as the simulation models developed were sufficiently accurate using only linear theory.

Conclusion 9

The main task was defined in the problem statement in Chapter 3 and is restated below:

Reduce the maximum equivalent radiated power level of all exterior MDF surfaces of the cabinet by a re-design of the internal support structure.

The main task is completed when each of the 4 sub-tasks, corresponding to Chapters 4-7, are fulfilled.

In Chapter 4 on page 24 a mode superposition harmonic finite element analysis has been developed in ANSYS Workbench called the benchmark model which prioritizes accuracy over computational efficiency. An experiment was conducted on the speaker, which was used in defining the external loads and boundary conditions applied to the model. The benchmark analysis was validated against the experiment, where a good correlation was observed between the displacements predicted by the benchmark and the displacements measured in the experiment. The benchmark analysis computes the EPRL of all the exterior MDF surfaces of the cabinet as a function of the frequency. It was determined that the frequency range of interest ranges from 300 Hz to 1000 Hz.

In Chapter 5 on page 43 the benchmark model has been simplified to the design model in order to reduce the solution time while still giving comparable results of ERPL to those of the benchmark analysis. By reducing the element size and changing the analysis settings such that the analysis is only performed in the frequency range of interest, the solution time of 80 min of the benchmark is reduced to 36 s in the design model. The results of the design model were very comparable to those of the benchmark, as the largest deviation in the magnitude and frequency of the peaks were 1.55 % and 0.43 %, respectively. The sensitivities of both the benchmark and design model were compared by removing the internal supports, which showed a similar change in the ERPL of both models.

In Chapter 6 on page 49 the position of the supports was parameterized and the objective function of minimizing the maximum ERPL in the frequency range of 300-1000 Hz was defined. The optimization was performed using a zero-order genetic algorithm, which converged after 7 iterations after having performed 224 evaluations. The optimized design was evaluated in the benchmark model, which gave comparable results to that of the design model. The decrease in maximum ERPL of the optimized design compared to the existing design was 3.3 dB, corresponding to a 53% decrease in the ERP.

In Chapter 7 on page 57 an alternative internal support structure was proposed in order to exemplify the possibilities of using simulation-driven design for cabinet design when the design is less restricted. A general bracing structure was proposed to demonstrate that no knowledge about the response of the cabinet is required to propose an acceptable design. The braces were parameterized and constrained to not decrease the air volume in the cabinet by more than 5%. The optimization was performed using a zero-order genetic algorithm, which converged after 20 iterations after having performed 1600 evaluations. The decrease in maximum ERPL of the bracing design compared to the existing design was 2.3 dB, corresponding to a 41.6% decrease in the ERP. Compared to the design with optimized positioning of the existing supports, the bracing design has a 1 dB higher maximum ERPL.

10 Further Work

In this chapter, relevant further work for this project is presented. The topics discussed in the chapter serve as ways to expand or improve the work and results obtained during this project.

10.1 Effects of manufacturing tolerances

As the loudspeaker cabinet is assembled by hand, and the internal supports are attached to the cabinet by glue, the manufacturing tolerances with regard to the placement of the internal supports can be assumed to be significantly large. These tolerances give rise to changes in the ERPL from the cabinet surfaces. The size of these effects is of relevance to the manufacturing and how to set the minimum tolerances. In order to assess this a sensitivity study could have been made at the optimized design point. Here, central difference approximations to sensitivities could be performed, similar to what was done in Section 7.2, with perturbations in the range of expected tolerances. This would show which parameters have a large effect of the ERPL, and thus need tight tolerances, and which parameters could have fairly large tolerances. This would then give an expected span of the ERPL given the tolerances.

10.2 Changing the cavity divider

In the project, two optimizations were performed on two different designs. Here all exterior cabinet surfaces, woofer placements and ports placements were kept the same as the existing design. In addition to this, the cavity divider in the cabinet was also kept the same. As this cavity divider cannot be externally seen, it is fair to assume that this also can be altered, as long as the air volume in the two cavities remains the same. This means that a possible solution to the reduction of the ERPL is not only subject to change from the support structure but also from the cavity divider. Although it is not the intended purpose of the divider to reduce the noise emitted from the cabinet, but rather to separate the cabinet into two equally sized air volumes, a parameterization and optimization of the divider might make this component serve two purposes. It is seen very plausible for this solution to be able to significantly reduce the ERPL as the divider is a very large component relative to the proposed internal supports. This means that there is a possibility to significantly change the stiffness and the mass distribution of the cabinet, both changing the location of eigenfrequencies and mode shapes, which will change the ERPL from the cabinet surfaces.

10.3 Development of a general initial design

In Chapter 7, an initial design based on internal braces on each cabinet surface was parameterized and optimized. This was done to exemplify that a general design concept could yield better results than that of the existing design. However, there is no guarantee that a different, but also general, design could not produce even better results. Here different general designs that are applicable to most floor-standing and bookshelf speakers, could be investigated. These different design concepts could then be parameterized and optimized on an array of different speaker models. The general design that gives the best optimization results for most speaker models could then be used as a standard initial design used for optimization for new speaker models. This investigation has the possibility to significantly improve the internal support structure in future speaker models without much design work required from the engineer.

Bibliography

[1] N.W. McLachlan. *Loud Speakers: Theory, Performance, Testing, and Design.* Oxford engineering science series. Clarendon Press, 1934.

[2] Vivian Capel. *An introduction to loudspeakers and enclosure design.* BP S. Bernard Babani Publishing, London, England, November 1988.

[3] Vance Dickason. *The loudspeaker design cookbook.* Audio Amateur Publications, 2006.

[4] Lothar Cremer, M A Heckl, and Bjorn A T Petersson. *Structure-borne sound.* Springer, Berlin, Germany, 3 edition, January 2005.

[5] Siegfried Linkwitz. The magic in 2-channel sound reproduction - why is it so rarely heard? *International Journal of Architectural Engineering Technology*, 2(2):113–126, December 2015. doi: 10.15377/2409-9821.2015.02.02.2. URL https://doi.org/10.15377/2409-9821.2015.02.02.2.

[6] Engineering ToolBox. *Sound Pressure*, 2004. URL https://www.engineeringtoolbox.com/sound-pressure-d_711.html.

[7] Marinus Luegmair and Hannes Münch. Advanced equivalent radiated power (erp) calculation for early vibro-acoustic product optimization. *International Conference on Sound and Vibration*, 01 2015.

[8] Singiresu S Rao. *Mechanical Vibrations.* Pearson, Upper Saddle River, NJ, 5 edition, August 2010.

[9] ANSYS. *Formulation of Harmonic Analysis Lesson 2*, 2021. URL https://courses.ansys.com/index.php/courses/harmonic-analysis-of-structures/lessons/formulation-of-harmonic-analysis-lesson-2/.

[10] COMSOL. *Mode Superposition*, 2018. URL https://www.comsol.com/multiphysics/mode-superposition.

[11] Robert D Cook, David S Malkus, Michael E Plesha, and Robert J Witt. *Concepts and applications of finite element analysis.* John Wiley & Sons, Nashville, TN, 4 edition, October 2001.

[12] Christopher Morfey. *The dictionary of acoustics.* Academic Press, San Diego, CA, September 2000.

[13] J.S.ARORA. *Introduction to optimum design.* AP (Elsevier), 2017. Fourth Edition.

[14] T. Murata and H. Ishibuchi. Moga: multi-objective genetic algorithms. In *Proceedings of 1995 IEEE International Conference on Evolutionary Computation*, volume 1, pages 289–, 1995. doi: 10.1109/ICEC.1995.489161.

[15] Nestor V. Queipo, Raphael T. Haftka, Wei Shyy, Tushar Goel, Rajkumar Vaidyanathan, and P. Kevin Tucker. Surrogate-based analysis and optimization. *Progress in Aerospace Sciences*, 41(1):1–28, 2005. ISSN 0376-0421. doi: https://doi.org/10.1016/j.paerosci.2005.02.001. URL https://www.sciencedirect.com/science/article/pii/S0376042105000102.

[16] Inc. ANSYS. Designxplorer user's guide. Version 2021R2, 2021.

[17] Luegard Bellman. *Dynamic Programming.* Princeton University Press, Princeton, NJ, USA, 1 edition, 1957.

[18] S. A. Smolyak. Quadrature and interpolation formulas for tensor products of certain classes of functions. *Dokl. Akad. Nauk SSSR*, 148(5):1042–1045, December 1963. URL http://mi.mathnet.ru/dan27586.

[19] Jochen Garcke. Sparse grids in a nutshell. In *Lecture Notes in Computational Science and Engineering*, Lecture notes in computational science and engineering, pages 57–80. Springer Berlin Heidelberg, Berlin, Heidelberg, 2012.

[20] ANSYS. *ANSYS Mechanical APDL Element Reference*, 2011. URL https://www.mm.bme.hu/~gyebro/files/vem/ansys_14_element_reference.pdf.

[21] ANSYS. *ANSYS Mechanical User's Guide*, 2021.

[22] Kendall E. Atkinson. *An Introduction to Numerical Analysis*. John Wiley & Sons, New York, second edition, 1989. ISBN 0471500232. URL http://www.math.science.cmu.ac.th/docs/qNA2556/ref_na/Katkinson.pdf.

Validation of benchmark model A

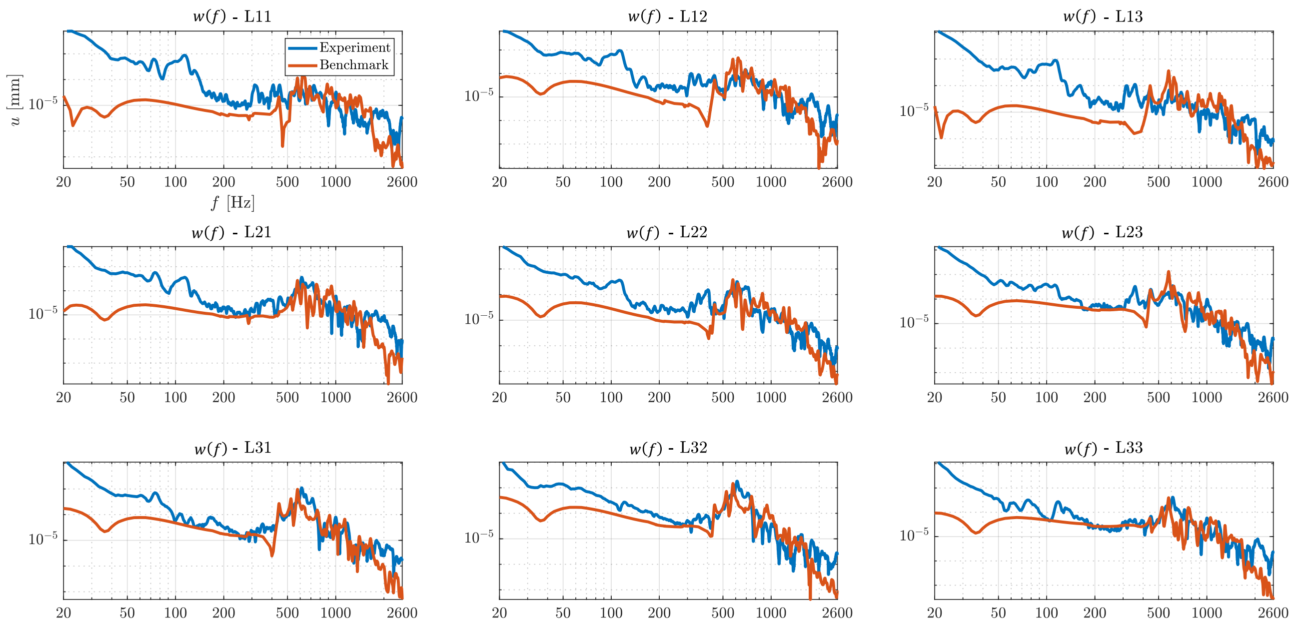

Figure A.1: w-displacements at all points on the left side from benchmark and experiment.

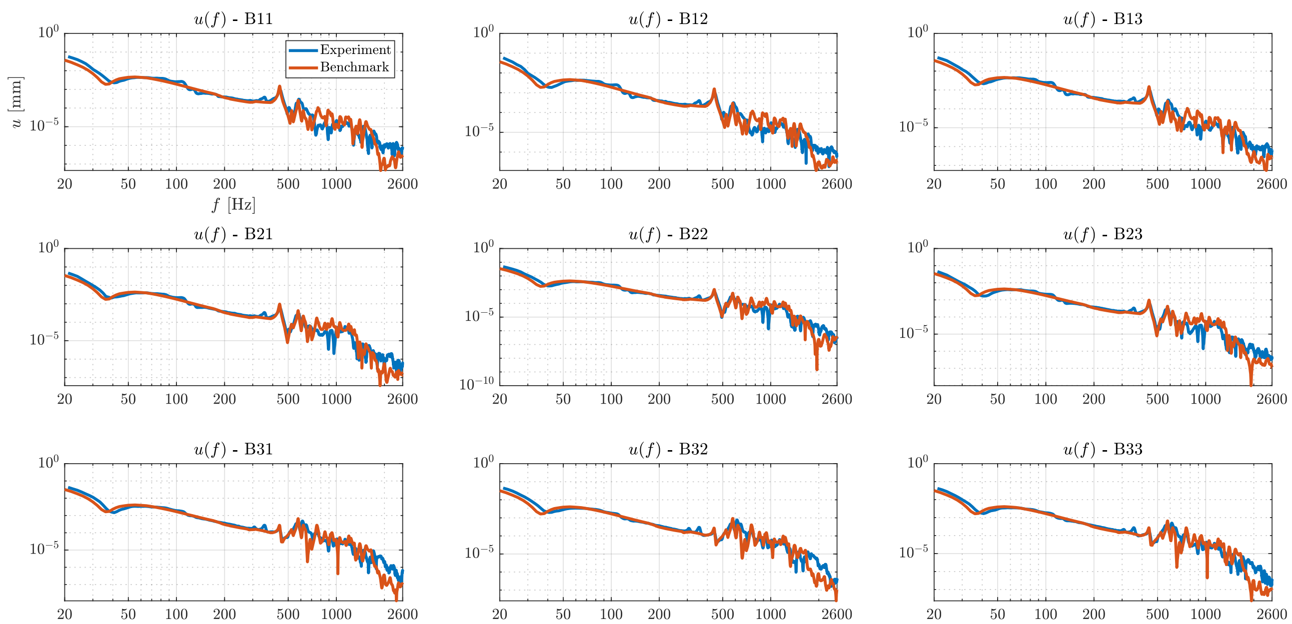

Figure A.2: u-displacements at all points on the left side from benchmark and experiment.

Accelerometer calibration B

Calibration Chart for Accelerometer Type 4374

Brüel & Kjær
Nærum Denmark

Serial No. 1060502

Reference Sensitivity at 50 Hz, 100 ms^{-2} and 24 °C

Charge Sensitivity* 0,117 pC/ms^{-2} or 1,15 pC/g

Voltage Sensitivity* (excl. AO 0038) 0,197 mV/ms^{-2} or 1,94 mV/g

Voltage Sensitivity* (incl: AO 0038) 0,167 mV/ms^{-2} or 1,63 mV/g
(Voltage Preamp. input Capacitance: 3,5 pF)

Capacitance (incl. integral cable) 592 pF

Capacitance of extension cable AO 0038 107 pF

Maximum Transverse Sensitivity (at 30 Hz, 100 ms^{-2}) 3,8 %

Undamped Natural Frequency 118 kHz

Typical Mounted Resonance Frequency 85 kHz
See reverse side of chart for frequency response curve

Typical Transverse Resonance Frequency, using Exciter Table 4290 with accelerometer mounted on a beryllium cube by cyanoacrylate adhesive: 21 kHz

Polarity is positive on the center of the connector for an acceleration directed from the mounting surface into the body of the accelerometer

Resistance minimum 20000 MΩ at room temperature

Date 83.08.09. Signature J.A.

1 g = 9,807 ms^{-2} or 10 ms^{-2} = 1,02 g

* This calibration is traceable to the National Bureau of Standards Washington D.C.

BC 109

Environmental:
Humidity: Sealed
Temperature Range: −74 to +250°C (−100 to +482°F)
Max. Shock Acceleration: 250000 ms^{-2} peak
Typical Magnetic Sensitivity (50 Hz—0,03 T): 30 ms^{-2}/T
Typical Acoustic Sensitivity: 0,1 ms^{-2} at 154 dB SPL (2—100 Hz)
Typical Base Strain Sensitivity (at 250 $\mu\epsilon$ in base plane): 0,005 $ms^{-2}/\mu\epsilon$
Typical Temperature Transient Sensitivity (3 Hz LLF): 4 ms^{-2}/°C
Specifications obtained in accordance with ANSI S2.11-1969

Physical:

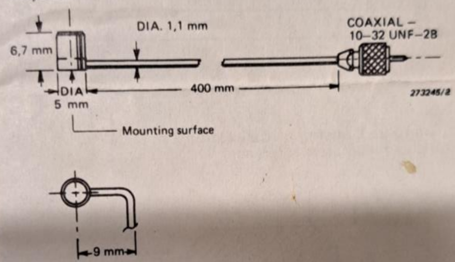

Material: Beryllium and Inconel
Weight: 0,65 gram excl. cable
Mounting: Adhesive
Mounting Surface Flatness: < 5 μm
Seismic Mass: 0,27 gram
Center of Gravity of Seismic Mass: 4,7 mm from mounting surface on central axis
Center of Gravity of Accelerometer: 3,6 mm from mounting surface, on central axis

For further information see B & K "Piezoelectric Accelerometer and Preamplifier" handbook.

Pat. DK 138768 and GB 1522785

Typical Temperature Sensitivity Deviation:
(Piezoelectric Material PZ 27)

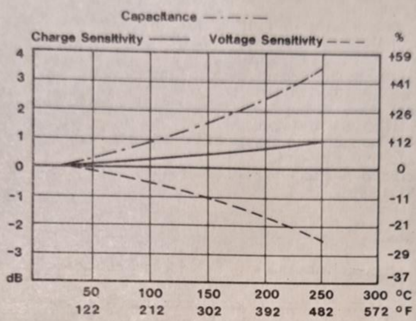

Typical Frequency Response Curve of 4374
(Corrected for response of 4290):

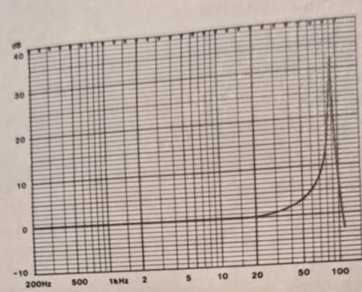

Schematic Drawing of Calibration Exciter 4290:
(Modified laboratory reference)

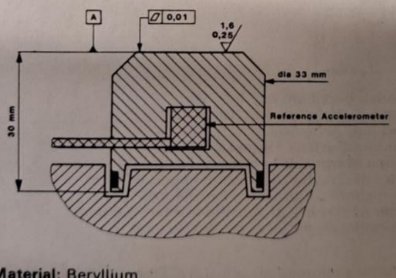

Material: Beryllium
Mass of Exciter Table: 38 gram

Mounting Technique:

Examine the mounting surface for cleanliness and smoothness
If necessary, machine surface to tolerances shown in schematic drawing of calibration table.
Use quick setting Methyl Cyanoacrylate Adhesive for mounting. Apply adhesive sparingly to one surface and apply pressure to set. Sets in 5—15 seconds